

**DEVELOPMENT OF ZINC–ALUMINUM–TITANIUM NANOCOMPOSITES  
SUPPORTED ON BIO-WASTE ACTIVATED CARBON FOR COATING MILD  
STEEL AISI 1015**

**BY**

**ONUOHA, David Chikaorama  
PhD/SEET/2016/890**

**DEPARTMENT OF MECHANICAL ENGINEERING  
FEDERAL UNIVERSITY OF TECHNOLOGY, MINNA**

**AUGUST, 2021**

**A THESIS SUBMITTED TO THE POSTGRADUATE SCHOOL, FEDERAL  
UNIVERSITY OF TECHNOLOGY, MINNA, IN PARTIAL FULFILMENT OF  
THE REQUIREMENTS FOR THE AWARD OF DOCTOR OF PHILOSOPHY  
DEGREE (PhD) IN MECHANICAL ENGINEERING (MATERIALS AND  
METALLURGICAL ENGINEERING)**

## ABSTRACT

Metal nanoparticles have been used in the past to coat mild steel against corrosion due to their outstanding mechanical and corrosion resistance properties. However, metal nanoparticles when used to coat mild steel without solid support or host matrix have shown some deficiencies such as micro cracking and pull-out of coatings from their substrates because of their inherent high surface energy which tend to make them coalesce to one another. Therefore, it is essential to trap these nanoparticles on a solid support when used for coating to help them stay away from each other for improved protection efficiency of nanomaterial coatings. This investigation was carried out on the development of zinc-aluminum-titanium (Zn–Al–Ti) nanocomposite supported on biowaste based activated carbon for coating of mild steel AISI 1015. Preparation of activated carbon from groundnut shell with percentage carbon yield of 50.04% was undertaken by chemical activation process, using  $ZnCl_2$  as activating agent at optimized process conditions of 600 °C, 1.32 hours and 3, representing the activation temperature, activation time and impregnation ratio respectively. A quadratic model was developed to correlate the activation process parameters to the response (percentage yield) and it was observed that the activation temperature with *F*-value of 2413.99 had the most significant effect on the yield among the other process variables. Zn–Al–Ti metal nanocomposites supported groundnut shell activated carbon (GSAC) coatings were developed by hosting the metal nanoparticles on the GSAC, starting with Zn metal nanoparticles at three different mixture ratios of 75:25 %wt, 50:50 %wt. and 25:75 %wt. The GSAC/Zn–Al–Ti sample formulated at mixture ratio of 50:50 %wt. which gave the least average crystallite size of 35.24 nm was then loaded into epoxy resin at four different ratios of 1:1, 2:1, 3:1 and 4:1 and coated on mild steel. Porosity and micro hardness tests were carried out on the coatings. The least percentage volume of porosity of 0.5% was achieved with the 2:1 ratio coating while the maximum micro hardness value of 157 HV was recorded with the 4:1 ratio coating. Optimum resistance to the corrosion of mild steel coupon in 1M HCl was achieved using ratio 2:1, having recorded the least charge transfer resistance ( $R_{ct}$ ) of 42.51  $K\Omega cm^3$  and protection efficiency of 98.73%.

## TABLE OF CONTENTS

	<b>Contents</b>	<b>Pages</b>
Cover Page	i	
Title Page	ii	
Declaration	iii	
Certification		iv
Dedication		v
Acknowledgment		vi
Abstract		vii
Table of Contents		vii
List of Tables		xiv
List of Figures		xvii
List of Plates		xx
<b>CHAPTER ONE</b>		
<b>1.0 INTRODUCTION</b>	<b>1</b>	
1.1 Background to the Study		1
1.2 Statement of the Research Problem	7	
1.3 Justification for the Study		8
1.4 Aim and Objectives of the Study	10	
1.5 Significance of the Study	11	

1.6 Scope and Limitations of the Study	12
--	----

## **CHAPTER TWO**

### **2.0 LITERATURE REVIEW 14**

2.1 Activated Carbon (AC)	14
2.2 Types of Activated Carbons	17
2.2.1 Powdered activated carbon	18
2.2.2 Granular activated carbon	18
2.3 Preparation of Activated Carbon	18
2.3.1 Physical activation	19
2.3.2 Chemical activation	20
2.4 Effects of Process Variables on Preparation of Activated Carbon	21
2.4.1 Effect of Impregnation ratio	22
2.4.2 Effect of activation temperature	23
2.4.3 Effect of activation time	24
2.5 Preparation of Activated Carbon from Agricultural Bio-Waste Resources	25
2.6 Reviews of Various Methods of Preparing Bio-Waste Based Activated Carbon	27
2.7 Applications of Activated Carbon	29
2.8 Calcination	30
2.9 Metal Nanoparticles	32
2.10 Synthesis of Metal Nanoparticles Using the Sol-Gel Method	34

2.11	Titanium Oxide Nanoparticles	37
2.12	Aluminum Oxide Nanoparticles	38
2.13	Zinc Oxide Nanoparticles	39
2.14	Nanoparticles Supported Activated Carbon	41
2.15	Composite Coatings	42
2.16	Epoxy Resin	44
2.17	Corrosion and Corrosion Mechanism	46
2.18	Material Porosity	49
2.19	Hardness of a Material	50
2.20	Review of Previous Works on Coating of Mild Steel	50
2.21	Surface Coating	57
2.21.1	Metallic coating	58
2.21.2	Non-metallic coating	58
2.22	Surface Coating by Metal Spraying	59

### **CHAPTER THREE**

#### **3.0 MATERIALS AND METHODS**

**60**

3.1 Materials 60

3.2 Methods 62

3.2.1 Preparation of groundnut shell particulate 62

3.2.2 Carbonisation of groundnut shell particulates 63

3.3 Microstructure Analysis of Carbonized Groundnut Shell Particulates 64

3.3.1 X-ray fluorescence (XRF) 64

3.3.2 Scanning electron microscope (SEM) analysis 64

3.4	Design of Experiment for Preparation of GS Activated Carbon	65
3.5	Preparation of Activated Carbon	68
3.6	Determination of Percentage Carbon Yield	68
3.7	Proximate Analysis of GSAC	69
3.8	Analysis of Experimental Result	69
3.9	Optimization of Experimental Variables for Groundnut Shell Activated Carbon Preparation	70
3.10	Model Validation	70
3.11	Calcination of GSAC Sample	70
3.12	Characterisation Techniques	71
3.12.1	The X-ray diffraction (XRD) analysis	71
3.12.2	Scanning electron microscopy (SEM) analysis	72
3.12.3	Fourier transform infrared (FTIR) analysis	72
3.12.4	Thermogravimetric analysis (TGA)	72
3.12.5	Brunauer-Emmett-Teller (BET) analysis	73
3.13	Synthesis of Zinc, Aluminum and Titanium Nanoparticles	74
3.13.1	Synthesis of titanium nanoparticles	74
3.13.2	Synthesis of aluminum nanoparticles	74
3.13.3	Synthesis of zinc nanoparticles	74
3.14	Characterisation of Prepared Metal Nanoparticles	75
3.14.1	Scanning electron microscope (SEM)	75
3.15	Development of Zn-Al-Ti nanocomposites Supported GSAC	76
3.15.1	Development of GSAC/ Zn metal nanoparticles composition	76
3.15.2	Development of GSAC-Zn /Al metal nanoparticles composition	77

3.15.3	Development of GSAC-Zn-Al/Ti metal nanoparticles composition	78
3.16	X-Ray photoelectron spectroscopy (XPS) Analysis	78
3.17	Mild Steel Samples Preparation	79
3.17.1	Heat treatment of mild steel samples	79
3.18	Coating of Mild Steel	79
3.19	Coatings Hardness Test	80
3.20	Coatings Porosity Test	80
3.21	Corrosion Test of Uncoated and Coated Steel Samples	81

## **CHAPTER FOUR**

<b>4.0</b>	<b>RESULTS AND DISCUSSION</b>	<b>83</b>
4.1	Characterisation of Groundnut Shell Particles	83
4.1.1	SEM EDS Analysis of Carbonized GS Particulate	83
4.1.2	X-ray fluorescence (XRF) analysis	85
4.2	Chemical Activation of Groundnut Shell Char	86
4.3	Analysis of Variance (ANOVA) for GS Carbon Yield	89
4.4	Model Fits Statistics	90
4.5	Optimization of the Experimental Variables	91
4.6	Model Validation	93
4.7	Proximate Analysis of GSAC	93
4.8	Graphical Presentation of Experimental Results	94
4.8.1	Predicted yield values plot against actual values	94
4.8.2	Plot of Studentized Residual and Predicted Values	95

4.8.3	Outlier t plot for GSAC percentage carbon yield	95
4.8.4	The 3-Dimension (3-D) plot showing effects of activation temperature and time on GS percentage carbon yield	96
4.8.5	Effects of activation temperature and impregnation ratio (IR) on GSAC percentage carbon yield in a three-dimensional (3-D) Plot	98
4.9	Surface Characterisations of Uncalcined and Calcined Samples of GS Activated Carbon	99
4.9.1	Scanning electron microscope (SEM) analysis result	99
4.9.2	X-ray diffractometer (XRD) analysis results	100
4.9.3	The FTIR analysis result	101
4.9.4	Thermogravimetric (TGA) analysis result	102
4.9.5	BET surface area analysis result	105
4.10	Scanning Electron Microscope (SEM) Analysis of Metal Nanoparticles	106
4.10.1	Scanning electron microscope (SEM) analysis with energy dispersive X-ray Spectroscopy (EDS) for zinc metal nanoparticles	106
4.10.2	Scanning electron microscope (SEM) analysis with energy dispersive X-ray spectroscopy (EDS) for aluminum metal nanoparticles	107
4.10.3	Scanning electron microscope (SEM) analysis with energy dispersive X-ray spectroscopy (EDS) for titanium metal nanoparticles	109
4.11	Transmission Electron Microscope (TEM) Analysis of Metal Nanoparticles	110
4.12	Determination of GSAC/ Metal Nanoparticles Composites from Crystallite Size Calculated Using Scherrer Formular	110
4.13	Preparation of Mild Steel Samples	119
4.14	Characterisation of Raw Steel Sample	119
4.15	X-ray Photoelectron Spectroscopy (XPS) Analysis of Prepared GSAC-Zn-Al/Ti Composites	127

4.16	Heat Treatment of Mild Steel Samples	127
4.17	Scanning Electron Microscope (SEM) with Energy Dispersive X-ray Spectroscopy (EDS) Analysis of the Cross Section of Coated Steel Sample	128
4.18	Determination of the Effect of GSAC-Zn-Al/Ti Weight Fraction in Epoxy on the Microhardness Value of Coated Mild Steel Samples	130
4.19	Determination of the Effect of GSAC-Zn-Al/Ti Weight Fraction in Epoxy on Porosity of Coated Mild Steel Sample	131
4.20	Electrochemical Impedance Spectroscopy (EIS) Result	133

## **CHAPTER FIVE**

<b>5.0</b>	<b>CONCLUSION AND RECOMMENDATIONS</b>	<b>142</b>
5.1	Conclusion	142
5.2	Recommendations	143

<b>REFERENCES</b>	<b>144</b>
-------------------	------------

## **LIST OF TABLES**

<b>Table</b>	<b>Page</b>	
2.1	Grouping for Pores Activated Carbon in terms of Pores	15
2.2	The standard specification value by ASTM on the determined parameters	16
2.3	General characteristics of thermosetting materials	44
3.1	List of reagents and their functions	60
3.2	List of materials/equipment and their functions	61
3.3	Design matrix for preparation of groundnut shell activated carbon	67

3.4	Experimental design table for GSAC calcination	71
4.1	Elemental composition of carbonized groundnut shell particulate as determined by SEM-EDS	84
4.2	X-Ray Fluorescence (XRF) analysis of groundnut shell particles	85
4.3	Groundnut shell actual and predicted carbon yield values	86
4.4	Regression coefficient for groundnut shell percentage carbon yield	88
4.5	ANOVA for GS percentage carbon yield	90
4.6	Fit statistics	92
4.7	Optimization of experimental variables for groundnut shell carbon yield	93
4.8	Model validation result	93
4.9	Proximate analysis result for GSAC	105
4.10	BET average surface area values of uncalcined (UC) and calcined (C71, C72, C81 and C82) GSAC samples	105
4.11	SEM-EDS elemental composition of Zn metal nanoparticles	107
4.12	SEM-EDS elemental composition of Al metal nanoparticles	108
4.13	SEM-EDS elemental composition of Ti metal nanoparticles	109
4.14	Structural parameters of AC/Zn mixture at various mixture ratios	112
4.15	Structural parameters of AC-Zn/Al mixture at various mixture ratios	114
4.16	Structural parameters of AC-Zn-Al/Ti mixture at various mixture ratios	117
4.17	Percentage elemental composition of raw mild steel sample	119
4.18	SEM-EDS elemental composition for raw mild steel	122
4.19	Results of XPS possible chemical compounds for GSAC-Zn-Al/Ti	126
4.20	SEM-EDS for Zn-Al-Ti-GSAC/Epoxy coated steel sample	129
4.21	Electrochemical parameters of EIS for samples	138

4.22 Comparison of the percentage corrosion protection (P.E) 139 **LIST OF FIGURES**

<b>Figure</b>	<b>Page</b>
2.1 Steps involved in the sol- gel method	27
4.1 SEM micrograph for carbonized groundnut shell particulate	83
4.2 Predicted values plot against actual values of GS production yield	94
4.3 Studentized residual and predicted response plot for GS yield	95
4.5 3-D response surface plot of GSAC yield (Effect of activation temperature and activation time)	96
4.6 3-Dimension response surface plot of GSAC yield (Effect of impregnation ratio and activation time)	97
4.7 SEM micrographs with EDX of (a) UC (b) C71 (c) C72 (d) C81 samples	100
4.8 XRD pattern for uncalcined (UC) and calcined (C71, C72, C81 and C82) samples	101
4.9 FTIR spectrum for uncalcined (UC) and calcined C71, C72, C81 and C82) samples	102
4.10 Thermogravimetric (thermal stability) plots fo uncalcined (UC) and calcined (C71, C72, C81 and C82) samples of GSAC	105
4.11 Thermogravimetric (thermal decomposition) graph of uncalcined (UC) and calcined (C71, C72, C81 and C82) samples of GSAC	107
4.12 (a) SEM micrograph and (b) EDS spectrum of synthesized Zn metal nanoparticles	and
4.13 (a) SEM micrograph and (b) EDX specrum for prepared Al metal nanoparticles	108

- 4.14 (a) SEM micrograph and (b) EDS result of prepared Ti metal nanoparticles 109
- 4.15 TEM micrographs of (a) Ti, (b) Zn and (c) Al metal nanoparticles 110
- 4.16 XRD pattern for GSAC/Zn composites at different mixture ratios 111
- 4.17 XRD pattern of GSAC-Zn/Al composites at different mixture ratios 113
- 4.18 XRD patterns of GSAC-Zn-Al/Ti composites at different mixture ratios 116
- 4.20 XRD pattern of heated and unheated mild steel samples 120
- 4.21 (a) SEM cross-sectional image and (b) EDS spectrum of raw steel sample 121
- 4.22 XPS spectra for (a) Zn 2p (b) Al 2p (c) Si 2p (d) O 1s and (e) GSAC-Zn-Al/Ti composites 124
- 4.23 Bar chart showing effect of annealing on the hardness values of mild steel sample 127
- 4.24 (a) SEM cross-sectional image and (b) EDS spectrum for Zn-Al-Ti-GSAC/Epoxy coated steel sample 128
- 4.25 Bar chart showing effect of ratio of weight fraction on hardness values of coated mild steel samples 130
- 4.26 Bar chart showing effects of weight fraction on the porosity of coated mild steel sample 131
- 4.27 Nyquist plots for (a) bare metal and neat epoxy coating and (b) coated steel samples 1 M HCl solution at 293k 133
- 4.28 Equivalent circuit diagrams for fitting the EIS data 136

4.29 Cross-sectional view of SEM image for (a) bare metal (b) neat epoxy and (c) 2:1 alloyed epoxy coated samples 140 **LIST OF PLATES**

<b>Plate</b>	<b>Page</b>
<b>I</b>	Photograph of groundnut shell being sun-dried 63
<b>II</b>	Photograph of mild steel samples 119

**CHAPTER ONE**

## **1.0 INTRODUCTION**

### **1.1 Background to the Study**

Nanotechnology has seen widespread use in the formulation of metal nanocomposite coatings that are important for surface protection over the last two decades (Abu-Thabit and Makhlof, 2015). Nanotechnology, through nanocomposite coatings, has enabled the introduction of insoluble nanoparticles of ceramics, metallic and non-metallic alloys into the matrix of the composite for the purpose of improving targeted mechanical and functional properties. Composite coatings offer rare mechanical and corrosion resistance properties (Fuyou *et al.*, 2013). Anti-corrosion property, thermal stability, and wear resistance were all improved by integrating nanostructured materials into traditional coatings (Fustes *et al.*, 2008). As a result of improved toughness and corrosion resistance characteristics, metal matrix reinforced with nanoparticles has been stated to have a wide range of engineering applications. Specifically, nanocomposite coatings with zinc nanoparticles added to them have been confirmed to demonstrate good surface properties (Akande *et al.*, 2018). The anti-corrosion property of epoxy coating can be improved by

modifying epoxy resin with polyaniline or by adding nano silica/aluminum powder together with the polyaniline.

Awaja *et al.* (2009) have observed that most industrially applied polymer resins and composites are characterized by low surface free energy and lack polar functional groups on their surface, resulting in fundamentally poor adhesion qualities. Since the inception of both the aerospace and auto industries, adhesion mechanisms have been known to be dependent on the surface characteristics of the materials in question (Chieh-Tsung *et al.*, 2004). Ceramic-matrix composites and metal of ceramic fibers have been employed to increase polymer composites toughness as metal-matrix. Polymer composites reinforced with SiC fibers and coatings of SiC fibers with a duplex C/TiB<sub>2</sub> reaction layer has proven effective in enhancing the interfacial bond strength, resulting in a moderate interfacial bond strength (Wang and Zhoa, 2019). Incorporation of nanofillers into the organic coatings might enhance their barrier performance, by decreasing the porosity and zigzagging the diffusion path for deleterious species. Tus, the coatings containing nanofillers are expected to have significant barrier properties for corrosion protection and reduce the trend for the coating to blister or delaminate (Nguyen-Tri *et al.*, 2018).

Metal nanoparticles reinforced polymer composites have proffered improvements over the earlier known limitations associated with polymers as corrosion inhibitors (Hefni *et al.*, 2016). The use of Zn metal nanoparticles in this investigation has been informed by their promising unique properties such as thermal and mechanical stability at room temperature, good physical and chemical stability, environmental friendliness, abundant availability, and low cost (Quadri *et al.*, 2017). Lightweight, splendid appearance and boundary

properties have influenced the selection of aluminum metal nanoparticles as essential for this investigation particles. Particularly, Al nanofillers can influence the boundary and mechanical properties of the organic coating (Nasih and Vicki, 2018). Ti nanoparticles have completed the ternary metal nanoparticles composites coatings because of their good thermal and electrical properties as well as their resistance to oxidation, corrosion in high temperature environments. These properties are crucial factors in the applications such as pipelines, castings and automotive industry (Shanaghi *et al.*, 2009).

Lu *et al.* (2019) reported that zinc coating provided good protection for steel but however stated that its long-term protection against high-chlorine or offshore steel structures was not good enough. Aluminum coatings on the other hand demonstrated high hardness, longer durability and higher corrosion resistance but less electrochemically protective than zinc coatings. The excellent performance of titanium alloys coatings has been attributed to their excellent adhesion properties as well as high hardness, low friction coefficient and enhanced corrosion resistance characteristics (Fuentes *et al.*, 2019). Therefore, the Zn- Al- Ti coatings could be the desired ternary alloy for optimal protection of steel. Zinc, aluminum and Titanium based composites have remained good choices for structural component applications and engine components as they offer improved toughness, and micro-hardness properties and exhibit enhanced resistance to corrosion in corrosive environments (Jinhua *et al.*, 2018; Ghorbani, 2014; Fang *et al.*, 2018). This investigation has sought to develop a ternary Zn–Al–Ti metal nanocomposites supported bio-waste activated carbon coating for the protection of mild steel surface.

Previous polymer coatings on mild steel surface with particles such as  $\text{Al}_2\text{O}_3$ ,  $\text{TiO}_2$ ,  $\text{SiC}$  and  $\text{Cr}_3\text{C}_2$  had been done without providing solid support for the random ions of metal nanoparticles has led to serious coating deficiencies such as cracks and pull-out of coatings from metal substrate due to poor adhesion (Sarmed *et al.*, 2013). The bio-waste based activated carbon used in this investigation would serve as a host matrix for stabilization of the participating metal nanoparticles. Metal nanoparticles ions are highly randomized and known to possess large surface energy which makes it easy for them to coalesce to form bulk particles, a situation which can be addressed by the use of solid support (Harish *et al.*, 2018).

Activated carbon is a carbonaceous material with an enormous internal surface area and well-developed porosity. As a result of the characteristic large surface area and microporosity, activated carbon is known to possess powerful adsorption property (Eric, 2010). The possibility of harnessing the surface properties of organic activated carbon in areas different from the highly researched and predominant use in separation of gases, treatment of waste water and industrial effluent is the driving force behind this research work.

Dispersion of metallic nanoparticles on a solid support like activated carbon could be essential in achieving special confinement of the particles in a nano range. Agglomeration of particles will occur in metal nanoparticles in the absence of repulsive forces provided by capping agents such as ligands and solid support. As a result, a good design of metal nanoparticles supported matrix composite could modify the composite system into desirable physical characteristics by taking into account the multifaceted interaction

between matrix interface and nanoparticles (Hanemann and Szabo, 2010). Therefore, this work does not only seek to investigate a new anticorrosion combination technique that could favourably compete with the conventional ceramic and metal matrix-based nanocomposites coatings, but also make case against the huge cost spent on conventional activated carbon by using agricultural wastes in preparing activated carbon.

Metal nanoparticles have attracted various industrial applications owing to their unique physical and chemical characteristics such as improved mechanical strength and high reactivity. Therefore, considering the intriguing track record of improved mechanical and anticorrosion properties offered by these metal nanoparticles relative to their bulk materials, it would be beneficial to incorporate them into a second phase with equally unique properties namely, large surface area, good surface chemistry and adsorptive and catalytic properties (Guo *et al.*, 2014).

Extensive investigation of porous carbon networks that have high specific surface area, good conductivity, and additional ion diffusion channels as catalysts or supports have been undertaken (Wanget *al.*, 2017). Therefore, it will be rational to anticipate that ternary Zn–Al–Ti nanocomposites supported bio-waste activated carbon coatings will exhibit higher strength and show greater resistance to corrosion. Dispersion hardness, selflubricity, high temperature inertness, excellent wear and corrosion resistance, and chemical and biological harmony are all common properties of ceramic or metal matrix nanocomposites with extra dispersed phase of particulates (Shei *et al.*, 2005).

Mild steels are generally low carbon steels with carbon content that ranges from 0.04% to 0.3%, depending on the source. Other chemical compositions of mild steel include manganese (from 0.70 to 0.90%), silicon (with maximum of 0.40%), sulfur (with maximum of 0.40%) and phosphorous (with maximum of 0.40%). Relatively cheap and malleable, mild steel has found applications in numerous engineering fields such as automobile, construction and electromechanical industries. Also, its applications in design and fabrication of gears, fasteners, bearings, shafts, cylinders, bolts and pressure parts of the heat exchanger make the desire for excellent mechanical and anticorrosion properties imperative. Therefore, the need to investigate the new ways of improving the surface protection of mild steel cannot be over emphasized (Rani and Basu, 2012). Mild steels play important roles in people's everyday life because they are used in the production of home appliances such as plates, spoons and parts of electric burners. Most manufacturers prefer to use mild steel as raw material to produce different kinds of engineering components like gear, shafts, keys, hand tools and cams, some of which must possess tough and solid surface and as well, a soft and hard core for their safe operation, durability and reliability, depending on their operating conditions (Abdulrahaman *et al.*, 2017). The above-mentioned properties are deficient in mild steel; thereby, causing surface wear and subsequently breaking upon impact during service. Corrosion instigates systematic weakening and failure of material characteristics which can sometimes lead to human injury, loss of life and collateral damage (Abdulrahaman *et al.*, 2017). Most common farm implements used by Nigerian commercial and peasant farmers like ploughs, harrows, cultivators, peddlers, are manufactured from cheaply and abundantly available low carbon and mild steels to suit poor and rich farmers (Ocheri *et al.*, 2017). During agricultural

operations in dry or wet season, these farm implements come in contact with acidic soils and moistures which result in corrosion and eventually contribute to quick failure and damage of the farm implements. Mild steel is known for its excellent ductility, toughness, high machinability and weldability but show poor resistance to corrosion and wear (Abdulrahaman *et al.*, 2017)

## **1.2 Statement of the Research Problem**

Harish *et al.* (2018) posited that the mechanical properties of metal nanoparticles tend to degrade with time as a result of the unstable behaviour exhibited by metal nanoparticles which could be related to the fact that metal nanoparticles are known to possess high surface energy and noted that the mechanical properties of metallic nanoparticles could be improved by stabilization of the nanoparticles on a solid supports or host matrix. This research is aimed at introducing organic molecules in form of bio-waste activated carbon into metal nanoparticles coating system to serve as a host matrix and prevent the agglomeration of metal nanoparticles which is known to adversely influence the quality and efficiency of metal nanocomposite coatings. Fatoba *et al.* (2015) reported zinc-based layer formation arising from inter-diffusion of zinc and iron atoms which created intermetallic phases and resulted in brittleness of coatings. Cracks in coatings of nickel particles penetrated the substrate and reduced fatigue life of steel (Sarmed *et al.*, 2013). These problems can be solved by hosting of the metal nanoparticles on a solid support to prevent direct interaction between them and the substrate.

Lu *et al.* (2019) have stated that the protection efficiency of zinc coating for steel at longterm service is not good enough and that while aluminum coatings demonstrated high coating hardness, they were less electrochemically protective than zinc coatings. Russo *et al.* (2021) also identified that poor adhesion to steel substrate is a problem associated with aluminum coatings on steel. However, Fuentes *et al.* (2019) have highlighted that the excellent performance of titanium alloys coatings could be attributed to their excellent adhesion properties as well as high hardness, low friction coefficient and enhanced corrosion resistance characteristics; thus, making the choice of zinc, aluminum and titanium metal nanoparticles the desired combination for optimal protection efficiency for steel surface.

Frequent pollution and other environmental hazards arising from indiscriminate dumping of groundnut shells in the farms and sometimes around residential areas is a major problem associated with Nigeria's enviable position as the third highest producer of groundnut in the world after China and India with 3, 028, 571 tons production capacity reported in 2016 (Miguel-Angel *et al.*, 2018).

### **1.3 Justification for the Study**

Development of novel materials from a combination of two or more different ones is being inspired by the desire for highly improved material characteristics that can withstand various rigorous engineering applications (Egbe and Onuoha, 2016). Nigerias's position as a major player in the oil and gas industries requires comprehensive and formdable approach to corrosion issues. There is urgent need to formulate highly corrosion-resistant

systems to bring to barest minimum, the devastating effects of corrosion in the oil and gas sector of our flagging economy since the problem of corrosion cuts across all the engineering fields. Corrosion has been identified as a major threat to global oil and gas industry. Most materials used in oil and gas industry at some point interact with different corrosive environments which tend to impair the usefulness and reduce the service life of such materials. For Nigeria as a predominantly oil-based economy, it is important for the nation's oil and gas assets to have effective and reliable corrosion management technique to mitigate against the consequences of corrosion. The expensive task of replacing crude oil facilities which break down mostly due to corrosion activities is the reason behind high production cost (Akinyemi *et al.*, 2012). Nigeria loses not less than ₦2 billion annually in the oil and gas industry, due to corrosion related problems and vandalization of oil pipelines (Peter-Omale 2005). Corrosion itself aids the activities of pipeline vandals (Akinyemi *et al.*, 2012).

The proposed utilization of Nigeria's over 2 billion metric tons of untapped coal reserve for heat and power generation may subject coal to unhealthy competition if other sources of activated carbon are not explored. Therefore, the use of natural-organic bio-wastes allows achieving several environmental advantages in comparison with their mineralinorganic counterparts.

Nigeria's growing population will continue to place mild steel in high demand because of its use in production of home appliances. Given that Nigeria is an agro based nation, better means of conferring superior surface properties on farm machines and implements, most of which are made of mild steel is highly needed to guarantee safety, service reliability

and to save families from excessive costs incurred in replacing such farm machines and implements.

Nigeria's quest for rapid industrial development coupled with the need to understand the properties, performances, cost and engineering potentials of locally available composite materials is a good reason for carrying out this investigation. Though activated carbon can be made from almost any raw material, waste materials are the most cost-effective and environmentally friendly (Eric, 2010). Environmental issues are associated with the use of coatings made of such metals as cadmium and chromium therefore; there is a crucial need to develop new alloy coatings like that of zinc- nickel system (Shao *et al.*, 2009). There is urgent need to carry out studies that are aimed at replacing costly commercial activated carbon with the unconventional low cost and locally available biowaste adsorbent as the high cost of commercial activated carbon seems to restrict its application (Malik *et al.*, 2006).

#### **1.4 Aim and Objectives of the Study**

The aim of this research work is to develop zinc-aluminum-titanium (Zn–Al–Ti) metal nanocomposites supported on bio-waste activated carbon coating for protection of the surface of mild steel against corrosion in 1 M HCl medium. The aim will be achieved through the following objectives:

- i. Preparation of activated carbon from Groundnut Shell (GS) and using the Central Composite Design (CCD) of response surface optimisation method to study the

effect of activation temperature, activation time and activation agent/char ratio on Groundnut Shell Activated Carbon (GSAC) yield.

- ii. Calcination and characterisation of optimized GSAC sample and using  $2^2$  factorial design to study the influence of temperature and time on the calcination process.
- iii. Prepare Al, Zn and Ti metal nanoparticles using the sol-gel method and characterisation of same.
- iv. Develop and deposit Zn-Al-Ti metal nanocomposites supported on groundnut shell activated carbon coatings on mild steel.
- v. Determine the porosity, hardness and anti-corrosion properties of developed ZnAl-Ti metal nanocomposites supported on groundnut shell activated carbon coatings.

### **1.5 Significance of the Study**

There is a huge market opportunity that can be explored with an anti-corrosion formulation that can favourably compete with already existing ones. Global anticorrosion market was valued at \$14,276 million in 2015, and is expected to plummet at a

Compound Annual Growth Rate (CAGR) of 9.7% to reach \$26,627 million by 2022 (Ashimita, 2017).

With Nigeria's leading role in groundnut production in Africa, preparation of activated carbon from locally sourced bio-waste will put Nigeria in a good position to earn foreign exchange from export of activated carbon. 1.1 million metric tons of activated carbon was

estimated to have been produced in the activated carbon industry in 2014, with 10% projected increase in demand for fresh activated carbon (Tadda *et al.*, 2016).

According to Ocheriet *al.* (2017), steel is used in over 80 percent of the world's industrial products and infrastructure, therefore, with Nigeria abundantly enriched with virtually all the raw materials that are necessary for production of steel, Nigeria could leverage on this natural endowment for production of steel development and improved surface protection system for steel to ensure optimal utilization of steel products and provide the platform for Nigeria's industrial revolution.

The choice of groundnut shell for this investigation will add value to the commodity, thereby, increasing the economic base of farmers and eventually encourage increased groundnut output and reduce the cost incurred in sourcing conventional materials for activated carbon preparation. Increased local content in the manufacture of engineering components can be achieved through the use of locally available materials in developing such engineering components (Mantia and Morreale, 2011).

### **1.6 Scope and Limitations of the Study**

The scope of this investigation is to develop Zn–Al–Ti nanocomposite supported on groundnut shell activated carbon coating for use in protecting mild steel against corrosion in 1 M HCl. The investigation will cover, but not limited to preparation and analysis of various samples.

- i. Optimisation of process conditions for preparation of Groundnut Shell Activated carbon (GSAC) will be carried out.

- ii. Analysis samples and experimental results reported iii. Safety measures, if any, related to the application of developed Zn–Al– Tinanocomposits supported on Groundnut Shell Activated Carbon coating will not be addressed.
- iv. Investigation will not cover comparison of anti-corrosion results obtained using electrochemical impedance spectroscopy (EIS) technique with those of other anticorrosion evaluation techniques.
- v. Behaviours of developed Zn–Al–Ti nanocomposites supported on groundnut shell activated carbon coating in corrosive environments other than 1 M HCL will not be covered.

## CHAPTER TWO

### 2.0

### LITERATURE REVIEW

#### 2.1 Activated Carbon (AC)

Activated carbon has been defined to primarily mean any carbonaceous material that has a enormous internal surface area and prominently developed porous structure, high mechanical strength, improved physico-chemical stability, high adsorptive potential, and high level of surface reactivity which is made possible by processing of the starting materials under elevated temperature reactions (Hayashi *et al.*, 2002; Hayashi *et al.*, 2000; Yacob *et al.*, 2008; Zhu *et al.*, 2008; Guo *et al.*, 2009; Dias *et al.*, 2007 and Hu and Srinivasan, 2001). Activated carbons as carbonaceous materials are different from elemental carbon by the oxidation of the carbon atoms that are present on the outer and inner surfaces (Al-Qodah and Shawabkah, 2016; Pratibha and Jayant, 2017). Activated carbon is characterized by outstanding large specific surface area, prominently developed porosity and tunable surface-containing functional group. Demiral and Aydin Samdan (2016) submitted that activated carbon is mainly a microporous solid. Furthermore, it includes meso and macropores, which are essential pores for adsorbate molecules to gain access to the interior of carbon particles. Activated carbon is tasteless (Sugumaran *et al.*,

2012). Activated carbon is amorphous (Alhamed, 2006; Campbell *et al.*, 2012; and Hassan *et al.*, 2010). Activated Carbon (AC) is a microcrystalline material, presenting a complex heterogeneous surface functionality (Benaddi *et al.*, 2000; Jassim *et al.*, 2012; Onyeji and Aboje, 2011). Activated carbon is non-graphite (Olafadehan *et al.*, 2012).

Activated carbon cannot be converted into crystalline graphite even at a temperature of above 3000 °C (Haris *et al.*, 2008). Abdullah *et al.* (2001); Wan-Nik *et al.* (2006) defined activated carbon as a form of carbon and black solid substance which resembles powder or granular charcoal.

Owing to high surface area and surface functional groups associated with activated carbons, they have been extensively used as an adsorbent to remove pollutants from gases, water and steams (Gupta *et al.*, 2005; Gupta and Rastogi, 2009; Ahmad *et al.*, 2012 and Nath *et al.*, 2013).

The volume of pores present in activated carbons is commonly described as greater than 0.2 ml/g, with an internal surface area of greater than 400 m<sup>2</sup>/g as determined by the nitrogen Brunett-Emmett-Teller (BET) method (McDougall 1991). The width of pores ranges from 3 Å to several thousand angstroms and the pores are generally grouped for convenience in terms of their diameters in the order presented in table 2.1.

Table 2.1: Grouping for Pores Activated Carbon in terms of Pores

	Pore Category	Pore Diameter Range
Macropores		From 500 to 20 000 Å
Transitional pores (or mesopores)		From 100 to 500 Å

Micropores From 8 to 100 Å

---

Source: McDougall (1991)

However, the standard specification value of the determined parameters for activated carbon proposed by the American Society of Testing and Materials (ASTM) are presented in the Table 2.2.

Table 2.2: The standard specification value by ASTM on the determined parameters

Parameters	Unit	Specific Range for Activated Carbon
Apparent Density	G/ml	From 0.36 to 6.74
Total Ash Content	%	Less than or equal to 8 max
Moisture Content	%	From 3 to 10 max
Particle Size Distribution	%	From 5 to 150
Average Particle Size Distribution	%	From 14 to 50

---

Source: (ASTM, 1991)

Despite the fact that the activation process and preparation variables are in control of the prepared carbon's physical properties and performance characteristics, the configuration of the pores and pore-size distribution are largely dictated by the nature of the starting material or precursor. (Bergna *et al.*, 2019). Table 2.3 shows fixed carbon content of raw materials commonly used in the manufacture of activated carbon.

The two major sources of activated carbon have been identified as coal and agricultural by-products or lignocellulosic materials (Ahmadpour and Do, 1997; Lee *et al.*, 2002). Natural carbonaceous materials such as coal, wood, and peat are used to make commercial activated carbons. Since process economics generally dictate the use of readily available, low-cost feedstock, the preparation of activated carbon must strike a balance between economic viability and performance (Mansooreh and Tahereh, 2008). Agricultural byproducts and wastes contain large amounts of lignocellulosic wastes, which could be used as cheap and sustainable sources of activated carbon. As a result, for a country like Nigeria, where the annual harvesting and processing of various agricultural crops results in significant quantities of agricultural by-products such as groundnut shell, palm kernel shell, and coconut shell, this choice is especially appealing. Furthermore, using environmentally friendly starting materials can reduce solid waste pollution while lowering the cost of the raw material used to make activated carbon. According to Harris *et al.* (2008), Rosalind Franklin was credited with the first serious effort towards understanding the structure of carbons prepared by the pyrolysis of organic materials in the 1950s, when it was demonstrated that these carbons fell into two (2) distinct groups, graphitizing and non-graphitizing. The carbon used to produce activated carbon is nongraphitizing, which means it cannot be converted into crystalline graphite even at temperatures of 3000°C or higher. Franklin proposed a simple non-graphitizing carbon model based on small graphitic crystallites connected together by cross-links; however, the existence of these cross-links was not clarified.

## **2.2 Types of Activated Carbons**

Though activated carbon is obtainable in three (3) forms namely, powder, granular and pellets, the most commonly used are granular and powdered activated carbon (Tada *et al.*, 2016). Menendez-Diaz and Martin-Gullon (2006) opined that the wide variety of possible structures of carbon as it moves from nano-scale to micro-scale could be responsible for the different types of carbon and have reiterated that powdered and granular activated carbons are typical carbon types. They noted that they are the nongraphitic and non-graphizable carbons with a high disordered micro-structure. The two main types of activated carbon are discussed in detail below.

### **2.2.1 Powdered activated carbon**

Powdered activated carbons have particle size below  $100 \times 10^{-6}$  nm. Carbon intended for batch treatment of liquid systems is pulverized to a preferred size after activation. Although, most activation processes produce carbon with a pH greater than 7 ( $\text{pH} > 7$ ) that is alkaline in nature. To satisfy the diverse needs of end users, the pH can be adjusted with the addition of acid or alkali. Where a low ash content and low conductivity are required, the carbon is washed with water or acid and then with water.

### **2.2.2 Granular activated carbon**

Granular activated carbon is used in columns or beds for gas and vapour systems, and also to process a number of liquids. The carbon is required to show enough mechanical strength to resist the abrasion incident for continued usage. Since high adsorptive power is associated with a loss of mechanical strength and density, the activation stage cannot be

too short, or the carbon will lack the necessary adsorptive power. It cannot, however, be too long, or the carbon would become too soft and bulky.

### **2.3 Preparation of Activated Carbon**

According to Kannan and Sundaram (2001); Kalders *et al.* (2008); Ozdemir *et al.* (2011); Zhang *et al.* (2011), Dipa *et al.* (2015) and Manoj *et al.* (2013), physical or chemical methods may be used to make activated carbons. Pratibha and Jayant (2016) suggested that the activation of a carbonaceous precursor is generally carried out by physical or chemical activation or a combination of both; chemical activation, on the other hand, is favoured over physical activation because it is a smoother process with a lower activation temperature.

#### **2.3.1 Physical activation**

Ioannidou and Zabaniotou (2007) and Williams and Reed (2004) described physical activation process of preparing activated carbon to be a two-step process of carbonization of carbonaceous material which is accompanied with the activation of resulting char at high temperature condition. The carbonization process is intended to produce charcoal from the starting material. Yahya *et al.* (2015) had reported that the carbonisation temperature usually falls between 400 and 850 °C. Hayashi *et al.* (2002); Attia *et al.* (2008) and Kalderis *et al.* (2008) have explained that the physical method of preparing activated carbon from agricultural wastes which entails carbonisation under inert conditions at high temperature (>800°C) followed by treatment in the presence of steam, carbon dioxide and air at relatively high temperatures (between 800 and 1000°C) is not in agreement with the chemical method that is carried out in one stage in the presence of a

variety of reagents such as acids, bases and salts. Viswanathan *et al.* (2009) suggested that the vital reaction that takes place during carbonisation is the removal of non-carbon elements resulting in the polymerization of carbon atoms into sheets of condensed aromatic systems which are often disordered and irregular and takes the form of a mixture of wood shavings and crumpled paper. Because of this misalignment, voids are formed in the charcoal and the incipient pores will become inaccessible. This will make the second step of activation necessary to create pores. Activation which takes place in the presence of suitable oxidizing gases like carbon dioxide, steam, air or their mixture is basically to develop further porosity and create some ordering of the structure which gives rise to highly porous solid of activated carbon.

### **2.3.2 Chemical activation**

During chemical activation, two activities of carbonization and activation go on at the same time with the starting material being mixed with the chosen chemical activating agent that behaves as dehydrating agent and oxidant. Mansooreh and Tahereh (2007) reported that the common feature of all chemical activation process is that the use of a dehydrating agent responsible for the thermochemical decomposition process, inhibiting the formation of tar and enhancing the yield of activated carbon. Ioannidou and Zabaniotu (2007) reported that chemical activation has been used in most studies to prepare activated carbon from corn cob, olive seed, rice husks, rice straw, cassava peel, peanut hulls, apricot stones, pecan shells, macadamia nutshells, hazelnut shells, and almond shells. Yahya *et al.* (2015) have listed the common chemical activating agents to include  $ZnCl_2$ ,  $H_3PO_4$ ,  $H_2SO_4$ ,  $K_2S$ ,  $KCN$ ,  $HNO_3$ ,  $H_2O_2$ ,  $KMnO_2$ ,  $(NH_4)_2S_2O_8$ ,  $NaOH$ ,  $KOH$  and  $K_2CO_3$ , maintaining that

chemical activation primarily involves a relatively low temperature condition (ranging from 300 to 800°C).

ZnCl<sub>2</sub> and H<sub>3</sub>PO<sub>4</sub> are commonly used as chemical activating agents for chemical activation process involving lignocelluloses materials (Williams and Reed, 2004). However, ZnCl<sub>2</sub> is known to produce higher surface area when compared with H<sub>3</sub>PO<sub>4</sub> (Al-Qoda and Shawabkah, 2009). Yahya *et al.* (2015) had suggested that the mechanisms involved by various activating agents differ, noting for instance, that the use of ZnCl<sub>2</sub> could promote the water molecules extraction from the lignocelluloses structures of the starting materials

Ioannidou and Zabaniotu (2007), hold that chemical activation offers several advantages since it is performed in a single step that marries carbonization and activation. Tsai *et al.* (1998), have said that one of the advantages of chemical activation is the fact that it needs lower temperature for operation and as well produces higher yield. Zhu *et al.* (2008) and Budinova *et al.* (2006) have suggested that chemical activation produces activated carbon with higher surface area while Lillo-Rodens *et al.* (2003) have opined that chemical activation guarantees better reduction of mineral matter content of starting material as compared with physical activation.

#### **2.4 Effects of Process Variables on Preparation of Activated Carbon**

The surface area of resulting sample during activation process, is determined by factors such as the temperature of the reaction, the activation time, the chemical nature and concentration of the activating agent, and the amount and nature of mineral ingredients in

the char. High temperature condition must be provided to guarantee a reasonably rapid rate of activation; however, temperatures above 1000°C should be avoided as such extreme condition could impair adsorption power. Jankoswka *et al.* (1991) have noted that adjusting carbonization conditions could significantly influence the final product, adding that an increased carbonisation temperature condition increases reactivity, but at the same time decreases the pores volume. This decrease in pore volume is as a result of an increase in the condensation of the material at higher carbonization temperatures which yields an increase in mechanical strength. Therefore, it becomes important to choose the correct process temperature based on the desired product of carbonization.

#### **2.4.1 Effect of Impregnation ratio**

Yorgun and Yildiz (2015) opined that the presence of activating agent promotes the dehydration depolymerization and redistribution of constituent bio-polymers and also favours the transition of aliphatic to aromatic compounds, thus increasing the carbon yield. Mansooreh and Tahereh, (2007) submitted that in chemical activation with phosphoric acid, it is a common knowledge that the impregnation ratio is one of the parameters that have a significant effect on the adsorption properties of activated carbon. Results of the investigation which studied effects of addition of different ratios of phosphoric acid to bagasse, hard shells of apricot stones, walnut shell and almond shell indicated that the iodine number of prepared activated carbon was substantially influenced by the phosphoric acid concentration in the impregnating solution, whereas the carbon yield did not change greatly. Malik *et al.* (2006) has submitted that the iodine number relates to the extent of micropore distribution in the carbon, giving an idea of the surface area and porosity of the activated carbon. It was observed that increase in the ratio of activating

agent with respect to char enhanced the surface area value and the pore volume but caused a decrease in carbon yield.

Zhu *et al.* (2008) reported that increased amount of activating agent resulted in increased pore volume and pore sizes. They noted that the BET surface area and the micropore volume changed with impregnation ratio, R when the later was less than 1.5 but with impregnation ratio, R greater than 1.5 ( $R > 1.5$ ), the two quantities decreased. Caturla *et al.* (1994) investigated the effects of  $ZnCl_2$  in the activation of peach stone and submitted that the amount of  $ZnCl_2$  introduced into the precursor during impregnation was a major factor that affected the textural properties, namely, specific surface area and micropore size distribution of the carbon material. Ahmadpour and Do (1997) evaluated the process of  $ZnCl_2$  activation of bituminous coal and identified impregnation ratio of the activating agent to carbon precursor as the most important process variables.

#### **2.4.2 Effect of activation temperature**

Yahya *et al.* (2015) and Tan *et al.* (2008) posited that activation temperature was the most significant parameter to yield, noting that increased temperature condition enhances devolatilization rate resulting in significant effect pore structure formation in activated carbon sample. Mansooreh and Tahereh (2007) reported that in the production of activated carbon from different agricultural wastes, increase in the activation temperature decreases carbon yield. Also, Varila *et al.* (2017); Yorgun and Yildiz (2015) reported that increased carbonization temperature resulted in decrease in carbon yield. This decrease in carbon yield was attributed to losses that may have occurred in form of carbon burn-off and expulsion of volatile matter from the sample.

Zhu *et al.* (2008) studied the effect of activation temperature when preparing activated carbons from sawdust impregnated with  $H_3PO_4$  serving as activation agent at a constant  $H_3PO_4$  /sawdust ratio of 1:1 and activation time of 1 hour at different temperatures. It was noted that the BET specific surface areas and micropore volumes also changed slightly with activation temperature. Conversely, the mesopore and macropore volumes showed only a slight decrease with increase in activation temperature. The microporosity of an activated carbon would be well developed at lower activation temperatures in order that its specific surface area would have a higher value. However, at higher activation temperatures, the micropore volume clearly decreased while the macropore volume increased. This would give rise to a decrease in the specific surface area of the resulting activated carbon because of the burn off of some micropore walls to form mesopores or macropores.

Sanni *et al.* (2017) showed more defined/finer pore with temperature increase from 450 to 575 °C which led to a higher internal surface area and improved adsorption properties. However, further increase in activation temperature to 850°C resulted in extreme carbonization which caused distortion of other pore walls and further expansion of other pore walls between successive neighboring pores. The investigation also recorded reduced yield at temperature above 450 °C with higher temperature of 575 - 850 °C observed to have altered the mesoporous and macroporous structure of the particles.

#### **2.4.3 Effect of activation time**

Mansooreh and Tahereh (2007) had submitted that activation time has significant effect on carbon yield, noting that prolonged activation time led to enlargement or even collapse

of some of the pores. Zhu *et al.* (2008) opined that the specific surface area of activated carbon sample increased rapidly with increased activation time up to 90 minutes and then decreased a little at longer activation time. Yahaya *et al.* (2010) prepared activated carbon from rice husk using chemical activation method where zinc chloride ( $ZnCl_2$ ) was used as chemical activating agent. The effects of activation temperature, activation time and

$ZnCl_2$ /char impregnation ratio (IR) on rice husk activated carbon (RHAC) yield and Cu (II) removal from aqueous solution were investigated. Results revealed that the carbon yield decreased with increase in activation time and temperature. This result agreed with Ahmad *et al.* (2009) which observed that while activation temperature played an important role in the yield of activated carbon prepared from rattan sawdust, activation time did not show reasonable effect on the carbon yield. Ahmad *et al.* (2012) achieved largest specific surface area and highest pore volume at activation time of 3 hours and equally noted slight change in pore volume and surface area between 5- and 7-hours activation times.

## **2.5 Preparation of Activated Carbon from Agricultural Bio–Waste Resources**

A good number of agricultural by-products and wastes has been investigated as starting materials for the preparation of activated carbon besides hard wood and bituminous coal

(Laine *et al.*, 1989; Rodriguez-Reinos *et al.*, 2001; Lafi, 2001; El-Sheikh *et al.*, 2003), Ahmedna *et al.*, (2000), Shawabkeh *et al.*, (1998), Rengarag *et al.*, 2002; Rengarag *et al.*, 1996; and Khalili *et al.*, 2000). These starting materials used in preparing activated carbon include sugarcane bagasse, pecan shells, coconut shell and wood, olive stones, palm seed, apple pulp, rubber seeds and molasses. Rishipal (2002) submitted that activated carbon has been produced from materials with high carbon content such as wood, coal, peat, lignin, nutshells, sawdust, bone, and petroleum coke. Malik *et al.* (2006) identified agricultural by-products as renewable sources of raw materials for activated carbon preparation because development of methods to put waste materials into use is greatly

desired and noted that the huge cost involved in preparing commercial activated carbon has been a major issue that seems to limit its application.

Eric (2010) had stated that despite the fact that activated carbon can be made from virtually any raw material, it is cheaper and environmentally friendly to prepare it from waste materials. Therefore, the use of cheap raw materials with excessive carbon contents and also low inorganic compounds has been a focus of research efforts in the last decades. McDougall (1991) has reiterated that companies in the Western World going into preparation of activated carbon in the past 30 years seemed to concentrate on using coal (which are mostly lignite, bituminous and anthracites) as precursor materials whereas, in the developing world new entrants tend towards using coconut-shell charcoal. The report suggests that since the method of preparation entails the elimination of volatile substance from raw materials, the economic relationship between the price, availability and quality of the raw material on the one hand and its volatile content on the other hand, is important. In a developing country like Nigeria, a major consideration in choice of precursor material for activated carbon preparation should be dependent on the availability of such waste materials as groundnut shell, which despite having high volatile substance and, hence, offering lower yields of activated carbon. Considering this, the economics involved in the use of such inexpensive waste materials as groundnut are more often than not favourable when compared with conventional precursors. According to Rodriguez Reinosa *et al.* (1995), a typical lignocellulosic material comprises approximately 48% carbon. However, Sanni *et al.* (2017) obtained a highest yield of 25% when  $ZnCl_2$  was used as activating agent in preparing activated carbon from coconut shell, a result which was attributed to several factors including the carbonization temperature and concentration of

ZnCl<sub>2</sub>. Ioannidou and Zabaniotou (2007) posited that thermal processes which have been extensively applied in removing moisture and volatile materials of agricultural bio-mass materials leave behind solid char with characteristics that are different from the parent bio-mass substances. The striking dissimilarities are mostly in surface area, pore structure, porosity and physico-chemical characteristics such as elemental analysis, composition, and ash content. This situation resulted in high reactivity, thus making the solid char a desirable by-product for making activated carbon.

## **2.6 Reviews of Various Methods of Preparing Bio-Waste Based Activated Carbon**

Several methods have been utilized to prepare Activated Carbon (AC) from bio-wastes. Mohammed *et al.* (2015), studied the preparation of activated carbon from groundnut shell sourced in Maiduguri, Nigeria by carbonizing in a muffle furnace without air at a temperature of 550 to 1000 °C for 60 minutes. This was followed by mixing the carbonized sample with an aqueous solution of phosphoric acid acting as activating agent. The mixture was then heated at a temperature of 120 °C for 3 hours to vaporize the water and again heated at a temperature of 650 °C in a muffle furnace to enable activation of the pores of the carbon sample. Result obtained indicated low content of volatile substance, implying abundance of pores on prepared sample.

Olowoyo and Orere (2012), produced activated carbon from different locally available shells of groundnut and coconut and obeche wood. The raw materials were oven-dried at 105 °C and carbonized in a muffle furnace for 1 hour at various optimum temperatures between 250 and 750 °C. Materials were then ground into powder, passed through 0.22mm mesh size and activated using Potassium carbonate (iv) (K<sub>2</sub>CO<sub>3</sub>) and Sodium hydrogen

trioxocarbonate (iv) ( $\text{NaHCO}_3$ ) at different temperatures that ranged from 500 to 1000 °C for 15 minutes. Result of density, over-all ash content, moisture content, particle size distribution and average size distribution obtained on characterization of the activated samples were found to be within the standards recommended by the American Society for Testing and Materials (ASTM).

Sumitra *et al.* (2016) used peanut shell to make activated carbon from through chemical activation where potassium hydroxide (KOH) and sodium carbonate ( $\text{NaCO}_3$ ) as

activating agent at activation temperature of 500 °C. The peanut shell was first carbonized and then mixed with chemical activating agent and  $\text{H}_2\text{O}$  at impregnation ratio of 1:1 before thermal activation in a nitrogen atmosphere at various temperatures (300 , 400 , 500 and 600 °C) for 2 hours. Result obtained on characterization showed that the amount of carbon was high in sample prepared using sodium carbonate at 500 °C. It was equally, noted that the peanut shell activated carbon prepared with potassium hydroxide at 600 °C activation temperature had the highest ash content among all the samples.

Aji *et al.* (2017), produced activated carbon from groundnut shell through chemical activation using phosphorus acid ( $\text{H}_3\text{PO}_4$ ). The physio-chemical parameters of the prepared activated carbon were very well compared with those prepared from similar agricultural wastes reported by the researchers, indicating that groundnut shell could be an excellent precursor for preparation of activated carbon for metal ions adsorption. Results obtained from the study indicated that the metal ion adsorption by the prepared

activated carbon improved with increase in both adsorbent dose and contact time with equilibrium being established in about one hour.

Das *et al.* (2015) used green coconut shell to prepare activated carbon through chemical activation method. Green coconut shells were chopped up, washed and sun-dried for 15 to 20 days and then loaded into the furnace operating at a temperature of 150°C for 24 hours to eliminate moisture and other volatile substances. The materials were then crushed with locally made crusher and sieved to 300-700µm particle size range. ZnCl<sub>2</sub> was used to carry out the chemical activation of the powder and the resultant slurry properly mixed and kept in the oven with temperature of 100°C for 24 hours.

## **2.7 Applications of Activated Carbon**

Activated carbon is famed as an encouraging material for adsorbents and catalyst support because of the unique and flexible texture as well as surface properties it possesses (Tsoncheva *et al.*, 2015). Nurettin *et al.* (2015) have opined that considerable attention is recently being given to the incorporation of silver nanoparticles into activated carbon to serve as filtering material in air purification systems and waste water treatment. Gong *et al.* (2015) studied the use of activated carbon in synthesizing uniform palladium (Pd) nanoparticles catalyst with tunable size. Tsoncheva *et al.* (2015) used activated carbon from waste biomass as a matrix for hosting mono- and bi- component copper and cobalt nanoparticles while studying the influence of the characteristics of carbon on the formation of copper/cobalt phase. Yahya, *et al.* (2015) investigated the application of activated carbon in water treatment, energy storage, fuel cells, nuclear power stations, batteries and hydrometallurgy, indicating that the physical properties of activated carbon

are key in determining its most appropriate usage. Sahu *et al.* (2010) reported that activated carbon can be used for the purpose of taste removal, deodorization and decolourization in food industries. Activated carbon is used in medical field to adsorb harmful chemical and drug and in gas cleaning applications for air filter and air conditioning (Yusufu *et al.*, 2012). Activated carbon is one of the most common adsorbents used in a good number of industries to remove and recover organic and inorganic compounds from gaseous and liquid streams. Yusufu *et al.* (2012) reported that the physical properties of activated carbon are key in deciding its application, suggesting that in a situation where the activated carbon is contemplated for an application where frequent back-washing is required, the hardness or abrasion resistance properties are prime for the activated carbon. Khalili *et al.* (2000) had posited that where activated carbon is meant for colour removal in liquid phase systems, a porosity in radii measuring from 20 to 500 Å would be required.

## **2.8 Calcination**

According to Kaur and Bhattacharya (2011), calcination is the process of heating a substance under controlled temperature and in a controlled environment with the intention of improving strength, thermal stability among other mechanical properties. During calcination process, the sample is subjected to heat, but without fusion for the purpose of bringing about some changes in physical and chemical constitution. Ulrich and Husing (2012) explained calcination to mean heating of a solid to a temperature below its melting point, to create a condition of thermal decomposition or phase transition other than melting or fusing. Calcination helps to remove volatile fractions and in decomposition of

carbonates and any other compound to their oxide states. During the calcination step, a solid-state reaction will take place between the constituents of the activated carbon, resulting in the desired phase. Proper calcinations at the right temperature are therefore necessary to obtain the best powder properties. Purer powders are achieved during calcination by elimination of the undesirable compositions. Philip *et al.* (2007) with a 1:1 atomic ratio of copper and chromium, calcinations at 600°C and higher resulted in the transformation of crystalline CuCrO<sub>4</sub> into tetragonal copper chromite (CuCr<sub>2</sub>O<sub>4</sub>). Both inorganic and organic materials can be calcined to improve their performance. Slimani Alaoui *et al.* (2014) calcined bone based activated carbon at 400 and 600°C for 4 hours while preparing bone chars by calcinations in traditional furnace. The objectives for calcinations are mostly to expunge water that may be present in the sample as moisture in the form of water of crystallization or as constituent water and to eliminate carbon dioxide and for further oxidation.

Komeili *et al.* (2016) in their study of the effects of calcinations parameters on the properties of alumina as a catalyst support noted that calcinations conditions impacted on the structural, acidic and textural characteristics of alumina. They, for instance, observed a rapid reduction in surface area when temperature rose from 800 to 1050°C. Nordin *et al.* (2015) suggested that one of the main factors that could influence calcinations process is temperature. Khalfasoui *et al.* (2014) calcined orange peels particles at 300, 400 and 550°C for  $\frac{1}{2}$  hour, 1 hour and 2 hours at each temperature and reported increased in specific surface area from 300 to 400°C while calcinations at 550°C with a relatively longer calcination time recorded reduced specific surface area as the particles became

thinner with reduced porosity of surface area. Mohamed *et al.* (2012) found that calcium oxide preparation was highly a function of factors such as temperature and time. Gao *et al.* (2017) studied the effects of calcinations temperature on the structure and adsorption performance of Ce-Mn/ Activated carbon materials and submitted that sample calcined at 800C exhibited the best phenol adsorption capacity. Zazo *et al.* (2009) noted that within the temperature range of 150 – 300C studied, calcinations temperature did not affect the porosity of the sample.

Calcination reactions usually occur at or above the thermal decomposition temperature defined as the temperature at which the standard Gibbs free energy is equal to zero.

## **2.9 Metal Nanoparticles**

Nanomaterials are materials that have the sizes of their individual building blocks less than 100 nm, at least in one dimension. Nanoparticles (especially transition metal nanoparticles) have intrigued researchers in the past few decades and have been used in magnetic, optical, energy storage devices as super capacitors and most importantly, they act as highly effective catalysts (Harish *et al.*, 2018; Ankur and Manivannan, 2015). It must be emphasized that the essence of nano science and technology is simply to control matter at the molecular level. Behzad and Hamid, (2006) submitted that when matter is as small as 1- 100 nanometers, several of its characteristics will change easily and will present various distinct features that are different from both macro-matter and single atoms as a result of the quanta effect, regional confinement of matter and large surface or interface effects.

Akbari *et al.* (2011) stated that the existence of unique properties of nanoparticles that are size-dependent is not in doubt and this could be attributed to their comparably large surface area. Verradate *et al.* (2012) have reported that metal oxide nanoparticles have in the past decades been developed extensively and have been widely deployed in many applications such as semiconductors, capacitors, catalyst, sensors, and batteries. Siavash (2011) noted that tremendous advances recorded in nanotechnology has opened up new opportunities for it in material sciences and engineering such as nanobiotechnology, bionanotechnology, quantum dots, surface-enhanced Raman scattering (SERS) and applied microbiology.

Nalwa (2000) stated that nanostructured materials are popular for their outstanding mechanical and physical properties which stem from the fact that they have extremely fine grain sizes and also high grain boundary volume fraction.

Popoola *et al.* (2014) have also hinted that the efforts now are being channeled to understanding the synergy of numerous nanoparticles, their mechanisms, dynamics and coating kinetics for corrosion management. Suba *et al.* (2016) have proposed that metal nanoparticles are interesting for a good number of applications because of their behaviour and stated that metal oxide nanoparticles have been successfully employed as corrosion inhibitor. Atta *et al.* (2015) modified magnetite nanoparticles with rose amidoxin (oxime) and studied the corrosion inhibition efficiency for mild steel and came up with encouraging result. Zubillaga *et al.* (2009) have successfully applied TiO<sub>2</sub> nanoparticles as corrosion inhibitor to steel, carbon steel and stainless steel. Again Sharmila *et al.* (2012)

reported nanosized CeO<sub>2</sub> as anticorrosive inhibitor for mild steel in different acid media of HCl and H<sub>2</sub>SO<sub>4</sub>.

Allahkaram *et al.* (2011) have submitted that as a result of their excellent mechanical and physical properties, nano materials have been the focus of many researchers who are attempting to create advanced corrosion resistant coatings. Malatji and Popoola, (2015) submitted that nanotechnology for some years now is being used to formulate metal coatings for surface protection.

### **2.10 Synthesis of Metal Nanoparticles Using the Sol-Gel Method**

There is a wide variety of physical and chemical techniques that has been deployed in the synthesis of nanoparticles of varying sizes as a result of the rising demand for various metallic and non-metallic nanoparticles in the past two decades (Monaliben *et al.*, 2015). The physical techniques include methods such as laser ablation, lithography and high-energy irradiation while the chemical techniques include sol gel method, flow injection, chemical reduction, nucleation, electrochemistry, solvo-thermal, microwave-assisted, and photochemical reduction.

Azlina *et al.* (2016) have suggested that the sol-gel method is the simplest method and offers the ability to control the particle size and morphology by systematic monitoring of reaction parameters, emphasizing that the main benefits of sol-gel method are the high purity and uniform nanostructure that is achievable at low temperatures.

The sol gel method is the transformation of a solution from a liquid (referred to as the sol) which is mostly colloidal into a solid (referred to as the gel) phase (Sajjadi, 2005). Bolla *et al.* (2017) submitted that the formation of metal oxide from sol- gel method involves different consecutive steps, first of which is the quick hydrolysis of the relevant metal precursor that gives the metal hydroxide solution. This is followed by instant condensation, resulting in the formation of three-dimensional gels after, which the resulting product is finally dried. Sajjadi, (2005) noted that the precursor for synthesizing these colloids consist of metal salts that are inorganic or metal organic substances such as metal alkoxides and posited that applications for sol-gel is based not only on the low process temperature, but also on the various special shapes obtained from the gel state combined with compositional and micro structural control.

Kamil *et al.* (2016) synthesized aluminum and titanium nanoparticles using the sol- gel method. In synthesizing titanium oxide nanoparticles using sol gel method, 100 mL of isopropyl alcohol was added to 15 mL of titanium isopropoxide and the mixture stirred for 10 minutes. 10 mL of de-ionized water was added drop wise to the mixed solution. Then the mixture solution was stirred continuously for 2 hours. The gel was left for 24 h in dark to dry after which the dried TiO<sub>2</sub> was calcinated at 550 °C.

Benhebal *et al.* (2013) prepared ZnO powder by sol-gel method from zinc acetate dihydrate, oxalic acid, using ethanol as solvent. The resulting product on characterization using techniques such as nitrogen adsorption isotherms, X-ray difraction (XRD), scanning electron microscopy (SEM), was seen to have a hexagonal wurtzite structure with the particles that are spherically shaped.

Premash *et al.* (2004) and Serena (2019) stated the major steps involved in sol-gel method to include:

- i. Preparing a homogeneous solution of pure precursor in an organic solvent that is miscible with water or the hydrolysis reagent.
- ii. Preparing the sol from solution by treating the homogeneous solution with H<sub>2</sub>O, or H<sub>2</sub>O with HCl/NaOH/NH<sub>4</sub>OH.
- iii. Allow the sol to change to gel through polymerization (aging) or poly condensation of hydrolyzed precursors.
- iv. The gel is formed into the desired form or shape to be followed by drying. The gel forms a dense 'xerogel' through collapse of the wet-gel structure (porous network) caused by the evaporation of the solvent (or an aerogel for example through supercritical drying).
- v. Calcination which is intended to give materials that is mechanically stable

The various steps involved in the sol-gel method are represented in Figure 2.1.

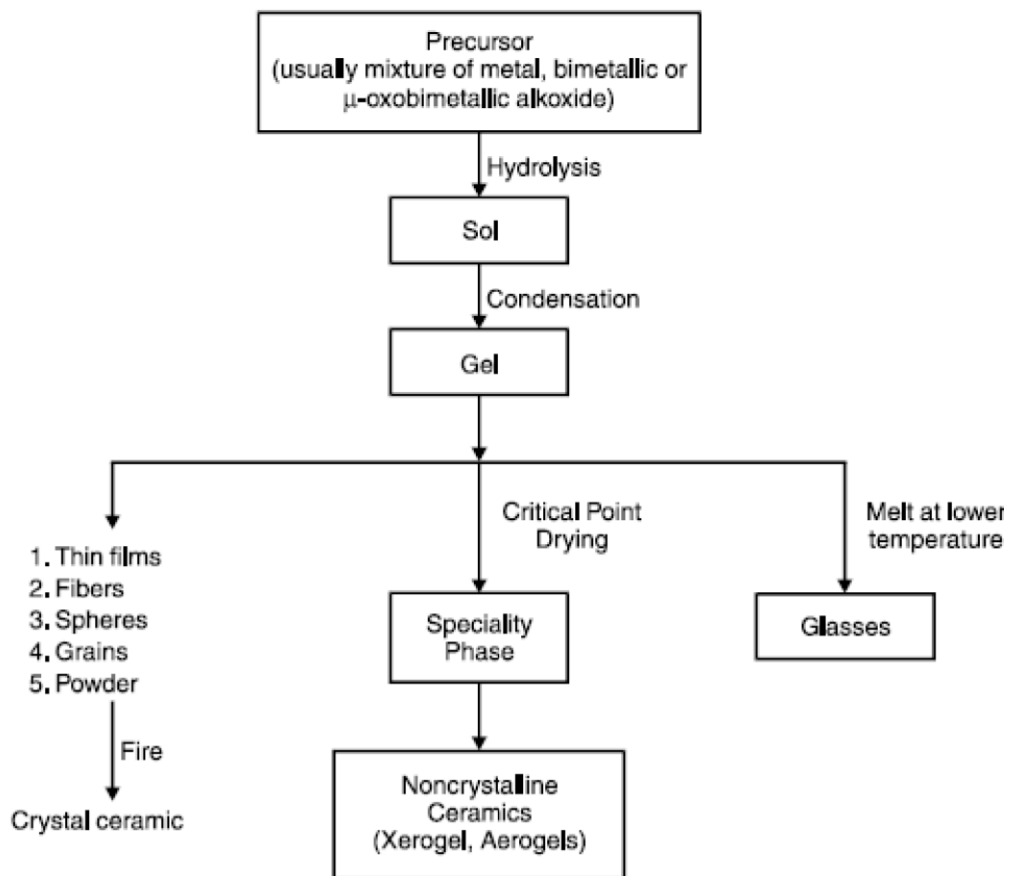


**Figure 2.1: Steps involved in the sol- gel method (Source: Pramesh *et al.*, 2004)**

### **2.11 Titanium Nanoparticles**

Titanium (Ti) is a metallic transition element and is the fourth most abundant structural metal that falls in the category of light elements. Titanium can easily be alloyed with other widely used elements such as iron and zinc (Goso and Kale, 2011). High specific strength (the same magnitude of strength as that of steel) and biocompatibility are some of the interesting properties of titanium, making it a common choice for biomedical implant

(Fang *et al.*, 2018; Agapovichev *et al.*, 2016). Ti nanoparticles are made as products of extractive processes that yield primary metal by reducing titanium tetrachloride (TiCl<sub>4</sub>) or titanium dioxide (TiO<sub>2</sub>) (Fang *et al.*, 2018). Avolio *et al.* (2016) opined that at a function of relative amount and surface treatment, Ti nanoparticles may enhance mechanical strength of the composite, ranging from  $31.1 \pm 2.5$  to  $43.7 \pm 0.7$  MPa—also contributing to biological response in terms of adhesion and proliferation mechanisms. The major applications for titanium are in aerospace, defence, medical, domestic and other emerging markets (Goso and Kale, 2011).

### **2.12 Aluminum Nanoparticles**

Aluminum (Al) nanoparticles, nano-dots or nano-powder are black spherical high surface area metal particles. Nanostructured aluminum particles typically measure between 10 and 30 nanometers (nm) and having specific surface area (SSA) the range of 30 to 70 m<sup>2</sup>/g. They may also be available at an average particle size of 70 -100 nm range with a specific surface area of approximately 5 - 10 m<sup>2</sup>/g (Ghorbani, 2014). Aluminum nanoparticles are considered promising as alternatives to conventional ink materials, replacing silver and copper nanoparticles, due to their extremely low cost and low melting temperature (Lee *et al.*, 2018). Aluminum (Al) and its nanoparticles have physical and chemical qualities that make them suitable for a wide range of applications, including alloy powder metallurgy parts for automobiles and aircraft and for conductive, heat reflecting and anti-

corrosion purposes (Baladi and Mamoor, 2010). Nanoscale Al particles are also used as high-capacity hydrogen storage materials (Li *et al.*, 2009). Vijaya *et al.* (2018) have reported that aluminum nanoparticles which is known to exist in several phases is one of the most important and extensively used structural composite materials for spacecraft, abrasive, electrical insulators and for thermal wear coatings.

Vladimir *et al.* (2018) posited that aluminum and its alloys are extensively used in modern engineering industries such as aerospace, electrical and chemical engineering mainly because of their striking properties which include high corrosion resistance, small linear shrinkage, crack resistance and good fluidity. Hassanpour *et al.* (2018) have stated that the diverse biomedical applications of aluminum nanoparticles is traceable to their exceptional physicochemical and structural features such as resistance towards wear, chemicals, mechanical stress as well as their favourable optical properties and a porous vast surface area; other reasons being low cost of production and ease of handling, noting that metal matrix nanocomposites based on aluminum and with nanoparticles incorporated into them exhibit higher performance characteristics, particularly in terms of ultimate strength, yield strength, heat resistance, plasticity and hardness.

Nano-sized aluminum particles are known to be a novel energetic material with extremely high reactivity due to its enormous specific surface area, and they are predicted to be used as a next-generation propellant in aerospace applications. The reactivity of aluminum nanoparticles is proportional to their size. Aluminum nanoparticles with a diameter of 3050 nm have been shown to be the most reactive, noting that because of their potential to oxidize, generating Al<sub>2</sub>O<sub>3</sub> nanoparticles instead, the manufacture of high purity Al nanoparticles is a big difficulty Ganeey (2010).

### 2.13 Zinc Metal Nanoparticles

Zinc metal nanoparticles are semiconductors with large exciton binding energy (60meV) and a broad band gap (3.37 eV) (Dutta *et al.*, 2009). Zinc nanoparticles are biocompatible semiconductor that is also a low-cost luminous material. For its unusual features and many applications in antireflection coatings, transparent electrodes in solar cells, ultraviolet (UV) light emitters, and diodes, lasers, varistors, piezoelectric devices, spinelectronics, surface acoustic wave propagator, it has garnered intense research efforts (Gorla *et al.*, 1999).

Phindile *et al.* (2012) reported that zinc nanoparticles are an environmentally friendly oxide, because of its nontoxicity and the ability to absorb in the UV range. With melting and boiling points of 1975 and 2360°C respectively are they are known to exhibit anticorrosive and anti- bacterial properties. Jinhua *et al.* (2018) have described Zinc nanoparticles as one of the most important metal oxide nanoparticles that is commonly utilized in various fields because of their unique physical and chemical properties. Zinc oxide nanoparticles are used in the rubber industry to, improve performance of high polymer in their toughness, provide wear proof of the rubber composite and intensity and anti-aging among several other applications. The methods for stable zinc oxide nanoparticles preparation have been widely developed in recent years which range from the chemical precipitation method, sol-gel method, solid-state pyrolytic method, solutionfree mechanochemical method to biosynthesis method.

The morphology of zinc nanoparticles depends on the process of synthesis (Khwaja *et al.*, 2018). They may be nano-rods, nano-plates, nano-sphers, hexagonal, tetrapods,

nanowire, nano-rings or nano-flowers (Wang and Lou, 2008; Jang *et al.*, 2008; Mahmud *et al.*,

2006; Kakiuchi *et al.*, 2006; Mahmud and Abdullah, 2006; Shen *et al.*, 2009; Ding and Wang, 2009; and Moezzi *et al.*, 2011).

#### **2.14 Nanoparticles Supported Activated Carbon**

Given that activated carbon which possesses powerful adsorption property has over the years been predominantly used in treatment of wastewater, separation of gases, removal of heavy metals from industrial effluent and as catalyst, researchers are beginning to explore other areas of possible application for it. One of the new areas activated carbon is being deployed is in its use as a host matrix for metal nanoparticles with the aim of improving material properties. The philosophy behind this is that when adsorbate ions are adsorbed on surface of an adsorbent, there is restriction of movement of those ions, resulting in decrease in degree of randomness of the system and eventual decrease in entropy. Grain boundaries are initiated and the inability of the ions to cross the grain boundaries imparts positively on the hardness of the system.

Hamid and Seyyed (2014) studied the effect in terms of mechanical properties of titanium dioxide nanoparticles with 21 nm particle size in a vinyl ester resin and suggested that incorporation of particles into the polymer can result in a reasonable improvement of mechanical properties, but however stated that a homogeneous distribution of fillers within the matrix is essential in achieving the desired result.

Hanemann and Szabo (2010) reported that it is possible to modify the physical characteristics of polymer matrix by the introduction of organic or inorganic nanostructured materials, in order to create new polymers with some new characteristics. This dispersion of nanoparticles in a matrix is very essential in recording enhanced ductility, strength and other mechanical characteristics of nanocomposite coating system.

However, Shi *et al.* (2009) had opined that when the amount of nanoparticles in nanocomposite coatings system surpasses a critical value, particles tend to agglomerate, resulting in decline of the mechanical characteristics in form of induced microcracks on the surface of the coating, higher wear rate and reduction in Young's modulus. Appropriate production and processing methods are required to achieve good particle dispersion.

Sun *et al.* (2008); Ramezanzadeha *et al.* (2011) have submitted that exchanges between nanoparticles and the matrix could be enhanced through chemical bonds.

Nanoparticles have the ability to grow the cross-linking densities present in the coatings or enhance the physical exchanges among macro-molecular chains of the matrix system. Shi *et al.* (2009) have said that matrix support for nanoparticles could be effective means for nanoparticles to supplement the poor mechanical and tribological behaviours of some polymer matrices such as their woeful opposition to surface abrasion and wear.

Burris (2007) had stated that some basic mechanisms are made the interface reinforcement possible. These mechanisms include the exchange between nanostructured materials and the polymer matrix system which may give rise to the formation of special microstructures (like a finer scale lamellar structure). As expected, the improved mechanical characteristics tend to prevent rapid crack extension in the coating system.

## 2.15 Epoxy Resin

Epoxy resin is a type of thermoset polymeric material, representing the highest performance resin among other resins that are currently available. Thermosetting resins are associated with a network structure formed exclusively by covalent bonds (Aigbodion *et al.*, 2011). However, epoxy is formed as a result of extended molecular chain structure like vinyl ester having reactive sites at both ends (Cripps and Gurit 2015). Epoxy resins are utilized in a wide spectrum of applications, and proper choice of resin, modifiers and cross-linking agents allows the properties to be engineered towards achieving desired performance characteristics (Massingil and Bauer, 2000). The mixture of the resin and curing agent gives the cured thermoset epoxy resin. Curing mechanism transforms the previously low molecular weight resin into a thermoset system, that is a space interlock or three-dimensional (3-D) chemical structure. Epoxy is used to explain both the uncured and cured forms of the resin.

Epoxy resin is available in various grades, from low viscosity liquid to high melting solids and is used in many industrial applications owing to its unique combination of properties compared to other resins. The molecules of epoxy consist of additional two ring groups at the center which serve to absorb thermal and mechanical stresses while offering good toughness and stiffness properties.

The curing process of epoxies is known to be different when compared with polyester resin. The most common curing agent is polyamine; the ensuing chemistry ensures that the epoxy binds to each amine site in order to form molecular three-

dimensional structures. Epoxy matrix materials are utilized in printed circuit boards and other similar areas. The unique properties of epoxy resin such as specific strength, chemical resistance and thermal stability make it most compatible adhesion to embedded fibre (Zhou *et al.*, 2008). Enhancement of mechanical properties such as adhesion of polymer are efficiently achieved by introduction of fillers (Naser and Fahad, 2018). Comparative advantages of epoxides in relation to other various thermosetting resins have presented in Table 2.5.

Table 2.3: General characteristics of thermosetting materials

Properties	Polyester	Phenolic	Epoxide
Density (kg/cm <sup>3</sup> )	1,200	1,200	1,100-1,500
Tensile Strength (MPa)	50-80	40	60-80
Tensile Elongation (%)	2-5	2.5	2-5
Flexural Strength (MPa)	90-130	90	100-150
Heat Deflection Temperature (°C)	60-100	120	290

Source: Lai *et al.* (2003)

## 2.16 Epoxy Composites Coatings

Verma *et al.* (2020) posited that epoxy resins represent a special class of organic macromolecules that are widely used for various industrial applications, noting that epoxy resins because of their macromolecular nature, provide better surface coverage and anticorrosive activities than simple organic corrosion inhibitors. Epoxy based coatings have gained prominence among numerous corrosion protection methods, due to higher

corrosion resistance and outstanding adhesion to metallic substrates (Ibrahim *et al.*, 2020; Xavier, 2020 and Zhou *et al.*, 2020). Several studies have been recently conducted on the performance of epoxy composite coatings incorporated with different nanofillers in various industrial fields (Kumar *et al.*, 2018). Verma *et al.* (2020) reported that several epoxy resins in pure and cured forms had been used as anti-corrosive coating materials, particularly for carbon steel in acidic and sodium chloride environments of percentage range between 3% and 3.5%. Chhetri *et al.* (2019) reported that despite the beneficial characteristics of epoxy resins high brittleness, poor impact resistance and flexibility which allow the formation of numerous tiny pores and microcracks due to mechanical damage; thereby necessitating the incorporation of nanofiller in order to improve the anticorrosion performance of the coating. This is achieved by increasing the diffusion path length of corrosive ions, thus restraining the formation of micropores and cavities. Epoxy coatings have consistently faced durability issues such as surface blistering and delamination which is mainly caused by the micro-pores formed during the curing stage of neat epoxy; thereby, leading to a substantial deterioration in its barrier performance (Abakah *et al.*, 2020). Chhetri *et al.*, (2019) emphasized that the introduction of a filler within the epoxy resin addressed observed challenges associated with epoxy and further augmented its anticorrosion properties, stating that in composites, the constituent components retain their intrinsic properties at the microscale level, but at macroscopic level, the composites exhibit properties superior to the participating components.

Satarkova *et al.* (2013) investigated the water uptake performance of epoxy composites coatings and concluded that free volume and restriction of polymer chains surrounding the graphene nanoplatelets influenced water absorption. Um *et al.* (2018) evaluated the

properties of graphene loaded water-based epoxy coating and discussed that, the presence of graphene did not affect the coating's adhesion to the metallic substrate but however improved the hydrophobic characteristics of the coatings

It has been confirmed that zinc incorporated nano composite coatings show good surface properties which is not unconnected with the strengthening influence of the embedded particles (Akande *et al.*, 2018). By virtue of toughness, thermal resistance, hardness and corrosion resistance, titanium and aluminum based composites have become good choices for structural component applications such as rockets, farm tools and engine components.

### **2.17 Corrosion and Corrosion Mechanism**

Scully (1987) defined corrosion as the dilapidation of metals as a result of interaction with the environments. Corrosion occurs when a material begins to deteriorate as result of a chemical attack or reaction under the influence of the surrounding environment; it is the result of chemical interaction between a metal and its environment which can be in different forms (Eugene *et al.*, 2016). Corrosion is the main cause of decay of metals when they unite with their surroundings as metals commonly degrade when they come in contact with moisture/ water (H<sub>2</sub>O), bases (NaOH, CaCO<sub>3</sub>, NaHCO<sub>3</sub>), acids (HCl<sub>2</sub>, H<sub>2</sub>SO<sub>4</sub>, HNO<sub>3</sub>), salts (NaCl), liquid chemicals, aggressive metal polishes, gases and sulfur containing gases (Pandian *et al.*, 2016). Commonly, corrosion tends to result in a relatively uniform removal of a surface with certain features in the surface of the metal such as grain boundaries, precipitates and metal/inclusion interfaces likely to be favorably or selectively attacked. Corrosion is a continuous mechnism which could be difficult to control and terminate (Rani and Basu, 2011). Corrosion, no doubts, poses an extreme concern in

engineering design. One of the first questions a designer must answer is whether or not the materials being used will be subjected to a corrosive attack during service. Fontana (1987) opined that careful choice of materials therefore, is a potent tool for dealing with severe corrosion. Failures that occur as a result of corrosion attack can be very costly therefore, preventing or reducing these attacks has become extremely important for industries and households. Donald *et al.* (2011) have suggested that corrosion process is aimed at lowering the free energy of a system and takes place over a period of time either at a higher or lower temperature. They submitted that the composition and physical integrity of a solid material is altered in a corrosive environment. Herle *et al.* (2011) have highlighted that the deterioration of metals is mostly seen in steel and iron materials for gas and transport industries where billions of dollars are spent either to inhibit or replace corroded materials. Chemical corrosion is seen when a corrosive liquid dissolves the material but in electrochemical corrosion, metal atoms are removed from the solid material as a result of an electric circuit that is produced. Chemical corrosion is an important consideration in many sectors such as transportation, utilities and production and manufacturing. Corrosion destroys more than (3%) of the world's gross domestic product (Shi *et al.*, 2017).

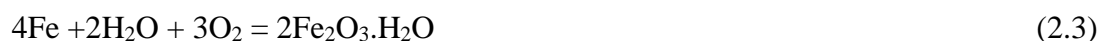
Popoola *et al.* (2014), had suggested that for convenience, it is desirable to ignore the detailed structure of the metal and consider corrosion as a non-homogeneous chemical reaction that takes place at a metal - nonmetal interface and involves the metal itself as one of the reactants, noting that corrosion can affect the metal in a variety of ways that depends on its nature and relevant environmental condition. Corrosion can be expressed, therefore, by the simple chemical reaction:



where A stands for the metal and B represents the non-metal reactant (or reactants), while C and D are the results of the interaction between A and B. The non-metallic reactants are most times referred to as the environment, though it should be noted that in an intricate environment, the main constituents can play only a minor role in the reaction. One of the products of the reaction, say, C, will be an oxidized variety of the metal while D will be a reduced variety of the nonmetal. C is normally termed the corrosion product, although the term could apply equally to D. In its simplest form, reaction (2.1) becomes



where the reaction product can be taken either as an oxidized variety of the metal or as the reduced variety of the non-metal. This form of corrosion reaction is referred to as a "dry" corrosion reaction because it does not require water or aqueous solutions. The resulting reaction in aqueous solution is called a 'wet' corrosion reaction, and the overall reaction (which is actually a sequence of intermediate steps) is written as



As a result, one (or more) of the reaction products in all corrosion reactions will be an oxidized form of the metal, aquo cations (example,  $\text{Fe}^{2+}(\text{aq.})$ ,  $\text{Fe}^{3+}(\text{aq.})$ ), aquo anions (example,  $\text{HFeO}_2^- (\text{aq.})$ ,  $\text{FeO}_4^{2-} (\text{aq.})$ , or solid compounds (example,  $\text{Fe}(\text{OH})_2$ ,  $\text{Fe}_3\text{O}_4$ ,  $\text{Fe}_3\text{O}_4 \cdot \text{H}_2\text{O}$ ,  $\text{Fe}_2\text{O} \cdot \text{H}_2\text{O}$ ), while the reduced form of the non-metal would be the other reaction product (or products). As a result, corrosion can be thought of as a heterogeneous redox

reaction at a metal–nonmetal interface, in which the metal is oxidized and the nonmetal is reduced.

According to Umoru (2001) and Natarajan (2013), the indirect cost of actual or potential corrosion is more difficult to quantify, but it is likely to be much higher, having been estimated in the United States of America (USA) to be about 300 billion dollars, while in developing countries like Nigeria, it is estimated to be around 10 billion dollars and around Rs. 2.0 lakh crores per annum in India.

### **2.18 Material Porosity**

Leisner and Benzoni (2017) stated that a porosity test reveals either the number of pores in a coating or the area of the substrate exposed through pores in the coatings and suggested that to guarantee a high quality product during time of use, it is important that the substrate is perfectly sealed by the coatings deposited on it.

Ramanjeet *et al.* (2014) opined that the causes of porosity may vary; however, they may be associated with the absorption of oxygen nitrogen and hydrogen gases. Leisner and Benzoni (2017) elucidated that porosity can occur as a result of the nature of the deposited coating as many materials which have deposition processes accompanied by reasonable hydrogen gas evolution, contain tensile stress, which often introduce formative cracks. Porosity can as well originate where the material being coated contains sources of porosity like the existence of non-metallic inclusions such as slag or carbides. The coating will not deposit on the inclusion, but rather grow over it. Depending on the deposition method, the inclusion might be sealed, but often a tiny pore will be left.

Ramanjeet *et al.* (2014) suggested that removal of sources of contamination from the workpiece surface and proper surface preparation of materials can significantly lower the level of porosity

### **2.19 Hardness of a Material**

Hardness is a measure of the resistance to permanent deformation or damage. Absolute hardness is measured in GPa, the same units used to measure pressure and elastic moduli (bulk modulus, shear modulus). This suggests that hardness and elastic properties can be related. There is, in fact, a connection, particularly with the shear modulus. Hardness, on the other hand, is a much more complicated property than elasticity, as it includes plastic deformation and brittle failure. For these reasons, a complete picture of hardness must include defects (mainly dislocations) and grain size in addition to the ideal crystal structure and its characteristics. The latter is linked to hardness by a phenomenon known as the HallPetch effect, which states that hardness increases as particle size reduces (in reality, there is a maximum in the nanometer range). By making nanoparticle aggregates and nanocomposites, it is possible to greatly increase the hardness of a material.

### **2.20 Review of Previous Works on Coating of Mild Steel**

Lu *et al.* (2019) investigated the anticorrosion properties of Zn–Al composite coating using the cold spraying method where poor protection efficiency of zinc coating for steel at long-term service and the fact that aluminum coatings were electrochemically less protective when compared with that of zinc were highlighted. Srivastava *et al.* (2010) studied the electrochemical effect of nano Cr<sub>2</sub>O<sub>3</sub> incorporation into Ni matrix and reported no significant improvement in corrosion resistance at a particle loading of 50g/L.

Malatji and Popoola (2015), investigated the coating of mild steel surface with ternary Zn-Cr<sub>2</sub>O<sub>3</sub>-SiO<sub>2</sub> nanocomposite using the electrodeposition method. The Zn-Cr<sub>2</sub>O<sub>3</sub>-SiO<sub>2</sub> composite coatings on mild steel surface which were produced from electrolytic chloride bath solution were examined for surface morphology, structural analysis and composition of the coatings using scanning electron microscope fitted with Energy Dispersive

Spectrometry (SEM-EDS) and X-ray diffractometer (XRD) to a modification in crystallographic orientation and as well a refinement of crystals. While testing the coatings for hardness and subjecting them to annealing temperatures of 250 C for 16 hours, improvements in microhardness and thermal stability were observed. The coefficient of friction decreased significantly, suggesting that the coatings were selflubricating and thus increased wear resistance. This investigation revealed that the incorporation of the Cr<sub>2</sub>O<sub>3</sub> and SiO<sub>2</sub> into Zn matrix has positive synergetic effect on the microhardness, thermal stability and tribology but not on the anticorrosion property. However, the corrosion resistance of pure zinc is insufficient at high temperatures and severe oxidising conditions; hence, it is alloyed with metals to provide higher corrosion resistance. Zn-Ni alloy coatings have been shown to have higher hardness than both zinc and cadmium separately (Youssef *et al.*, 2004).

Deen *et al.* (2009), evaluated the anti-corrosion characteristics of painted mild steel surface using the Electrochemical Impedance Spectroscopy (EIS) technique. The EIS method was used to assess the corrosion resistance of zinc-based epoxy paint on chemically treated mild steel surfaces in artificial sea water. The electrochemical impedance spectroscopy and Open Circuit Potential (OSP) measurement of the rusted surface before being treated chemically were also investigated in order to compare result with that obtained from the corrosion behaviour of the applied paint film. The electrochemical characteristics of painted surface were estimated based on the obtained EIS parameters which included paint film resistance, painted film capacitance and double layer capacitance. Based on calculation using EIS spectrums, it was noticed that pore resistance ( $R_{pore}$ ) decreased with the appearance of double layer capacitance ( $C_{dl}$ ) which

was as a result of the electrolyte passing through the film, a result which was further confirmed by the decrease of polarization resistance ( $R_p$ ).

Dhawan *et al.* (2015) used Tafel extrapolation, salt spray testing, and weight loss methods to create a strongly hydrophobic and anticorrosive hydrophobic polyaniline-SiO<sub>2</sub> composite (HPSC) coating for safety in the marine environment by chemical oxidation polymerization and tested it for protection of mild steel from corrosion in a 3.5 percent NaCl aqueous solution. The hydrophobic properties of HPSC were investigated using contact angle measurement after a suitable coating of HPSC was deposited on mild steel using epoxy resin by powder coating process. Their findings revealed a significant reduction in corrosion present, indicating improved mild steel safety in the marine climate. After 60 days of immersion in a 3.5 percent NaCl solution, the coating containing

HPSC had a safety efficiency of 93.3 percent and 85 percent in a 35-day salt spray test. The passivation of steel by polyaniline was credited with the high efficiency of HPSC containing coatings. It was also recorded that using HPSC coated with mild steel at 6.0 wt. percent HPSC loading in epoxy resulted in a higher safety efficiency of up to 96 percent.

Wang *et al.* (2010), examined the effect of SiO<sub>2</sub> nanoparticles on the microstructures and properties of Ni-W-P/CeO<sub>2</sub>-SiO<sub>2</sub> composites prepared by pulse electrodeposition when prompted by the rising demand for composites with enhanced resistance to enormously aggressive environments because of rising demand for extended safe service life of industrial objects. Ni-W-P based composites containing CeO<sub>2</sub> and SiO<sub>2</sub> nanoparticles on

the surface of common carbon steel was prepared by pulse co-deposition of Ni, W, P, CeO<sub>2</sub> and SiO<sub>2</sub> nanoparticles. The microstructures and properties of Ni-W-P/CeO<sub>2</sub>-SiO<sub>2</sub> composites were investigated in relation to the amount of SiO<sub>2</sub> in the bath. The composites had the fastest deposition rate, the highest microhardness, compact microstructures, smaller crystallite sizes, and uniform distribution of W, P, Ce, and Si within the Ni-W-P matrix metal when the SiO<sub>2</sub> concentration in the bath was held at 20 g/L. Inhomogeneity of microstructures and refinement in grain size were observed when the concentration of SiO<sub>2</sub> in the bath was increased from 10 to 20 g/L. As the SiO concentration was increased to 30 g/L, the crystallite sizes increased even further, resulting in the presence of certain bosses with nodulation forms on the composites' surface.

Olfa *et al.* (2012), explored the use of nano-SiO<sub>2</sub> particle-modified Zn-Ni alloy coatings to enhance certain surface properties. The effects of loading Zn-Ni alloy with nanoparticles on deposit morphology, phase structure, composition, and subsequent influence on the corrosion process in corrosive solution containing 3% NaCl, as well as the thermal stability of deposits at 200°C, were investigated. The X-ray diffraction measurements showed that the alloys comprised two phases which were pure zinc and  $\gamma$  phase. Results also showed that Zn-Ni alloy composites exhibited higher values of microhardness and were thermally stable up to 24 hours at 200°C and on the other hand, a better corrosion resistance in corrosive media of 3% NaCl. This behaviour indicated that the content of Ni nanoparticles in the composite was responsible for the observed corrosion behaviour.

Yathish and Chitharanjan (2013), studied the anti corrosion property of electrodeposited multilayer Zn-Ni-SiO<sub>2</sub> nanocomposites coatings on mild steel. The corrosion behaviours

and properties of the multilayered Zn-Ni-SiO<sub>2</sub>nanocomposites coatings were studied using electrochemical polarization and impedance methods. For optimum corrosion resistance, deposition conditions such as cyclic cathode current densities (CCCDs), bath composition, and layer number were optimized. When a coating was changed from a monolayer to a multilayer type, the anti-corrosion corrosion performance of multilayer nanocomposites coatings improved significantly. The corrosion density of multilayer nanocomposites coating reduced progressively with number of layers up to an optimal level, and then started to increase. Under optimal conditions, the multilayer nanocomposites Zn-Ni- SiO<sub>2</sub> coatings were found to be about 107 times higher corrosion resistant than the monolayer Zn-Ni-SiO<sub>2</sub> coatings, which are about 1.5 times higher corrosion resistant than the monolayer Zn-Ni alloy coatings.

Fatoba *et al.* (2015), studied the hardness values and corrosion characteristics of laser alloyed Zn-Sn-Ti coatings of UNS G10150 mild steel. Two different alloy compositions of 25%Zn-25%Sn-50%Ti and 20%Zn-20%Sn-60%Ti were used in the study. The laser alloy of Zn-Sn-Ti on the UNS G10150 steel showed better hardness values and corrosion resistance when compare with the substrate with all characteristics improving with increasedTi content in the alloy. At a laser power of 900W and a speed of 0.8m/min, the best properties were obtained with 20 percent Zn-20 percent Sn-60 percent Ti.

Popoola *et al.* (2016), investigated the anti-corrosion behaviour of Zn- ZnO-Y<sub>2</sub>O<sub>3</sub> coating on mild steel surface using the electro-deposition technique. The coated samples were analyzed for composition and microstructure using standard methods, and it was found that the microstructure of the deposit obtained at 10% Ytria showed fine-grains Ytria

deposit on the mild steel surface. In sodium chloride solution, the obtained results exhibited improved wear behaviour and anti-corrosion properties. Coated mild steel samples also demonstrated increased hardness values both before and after heat treatment.

Punith and Venkatesha (2013) studied coating of mild steel surface with Zn-TiO<sub>2</sub>. Electromagnetic experiments using polarization and impedance methods were used to assess the anti-corrosion properties of binary Zn-TiO<sub>2</sub> composite coatings made from bath solution with varying amounts of TiO<sub>2</sub>. When compared with pure zinc coatings, the results showed that TiO<sub>2</sub> incorporated zinc coatings had better corrosion resistance to aggressive media. In addition, the embedded TiO<sub>2</sub> nanoparticles improved the deposit's compactness, microstructure, and desired orientation.

Ghaziof and Gao (2015) investigated the anti-corrosion behaviour of Zn-Ni-Al<sub>2</sub>O<sub>3</sub> nanocomposite coatings on the surface of mild steel using a novel sol enhanced electroplating method. Cyclic voltammetry, XRD, ESEM, and Tafel tests were used to investigate the effect of alumina sol on the electrodeposition process and coating properties and it was discovered that Zn-Ni-Al<sub>2</sub>O<sub>3</sub> nanocomposites coatings presented more uniform and compact deposits with fine grained microstructure when compared with that of Zn-Ni coatings. As alumina nanoparticles were introduced into Zn-Ni coatings, the corrosion resistance of the coatings improved dramatically.

Popoola *et al.* (2016) investigated the corrosion and wear characteristics of ternary NiSn-P composites coatings on mild steel surface using the electroless method. The linear polarization analysis of the binary Ni-P and ternary Ni-Sn-P electroless depositions of

mild steel surfaces showed that the ternary Ni-Sn-P electroless deposit had a stronger corrosion resistance property with corrosion rate values of 0.000246 mm/yr as compared to the binary Ni-P deposit with 0.016672 mm/yr. It was also revealed that the coefficient of friction for the unplated samples ranged from 0 to 0.08, while the coefficient of friction for the plated samples was significantly lower, ranging from 0 to 0.02.

Fayomi *et al.* (2015) investigated the corrosion resistance and mechanical characteristics of doped Zn-Al-SnO metal matrix composites coating on mild steel substrates, in which the Zn-Al coating containing SnO<sub>2</sub> nanoparticles was prepared by electrodeposition from sulphates electrolyte. Using linear polarization techniques, the anticorrosion activity of a coating prepared with various concentrations of SnO<sub>2</sub> and potential was investigated in a 3.65 percent NaCl solution. Coatings were tested for wear and hardness using an accelerated reciprocating dry sliding wear test and a diamond micro-hardness tester. Their results showed that introduction of SnO<sub>2</sub> in the plating enhanced anti-corrosion and mechanical characteristics of Zn-Al-SnO<sub>2</sub> composites coatings.

## **2.21 Surface Coating**

A surface coating is a thin layer of material that serves as a barrier between a metal and its surroundings. Coatings have been applied to material surfaces to alter and enhance their properties (Mohd *et al.*, 2018). New designs and improvements of surfaces are the results of rising requirements of surfaces and interface properties of mechanical systems. Before now, material selection was predominantly used to protect engineering materials from degradation occasioned by corrosion and wear and also ensure optimal performance of these materials in various operating conditions, but this is no longer technologically or

economically feasible (Guo *et al.*, 2014). Protective systems are being developed to enhance the corrosion resistance property of materials. There equally exist multi-layered systems in coating operation. The use of chromating and phosphating phases for coatings is being substituted with molybdate, rare earth, silicate, titanium oxides, or zirconium oxides owing to grave environmental and health concerns (Oki 2007; Phani *et al.*, 2005; Lunder, 2004; Song and Mansfeld, 2006; Montemora *et al.*, 2009 and Wen *et al.*, 2008).

Metal coatings are applied using any of electrodeposition or electroplating, hot dipping, flame spraying, cladding and vapour deposition while inorganic coatings are applied using spraying, diffusion, or chemical conversion. Surface coating involves two types namely, metallic and non-metallic coating. Metallic and non-metallic coatings are deployed to assuage the fretting wear damage incurred in engineering components (Harris *et al.*, 1985).

### **2.21.1 Metallic coating**

In metallic coating, the material is coated with a layer or layers (in the case of multilayer coating) of other metals which are either more noble than the material or less noble than it. For instance, steel material can be coated with either copper which is more noble than steel or zinc which is less noble than it. When coating a material with a metal that is more noble than it, care should be taken to guarantee that the coating does not have pores or cracks to prevent the formation of dissimilar metal corrosion cells, which would in turn lead to the material's corrosion. However, Popoola *et al.* (2016b) argued that metallic coatings should be self-passivation with a potential lower than the substrate to allow for a long-life cycle and high protecting efficiency, and at the same time, that the potential

difference between coating materials should not be too negative; otherwise, hydrogen embrittlement on the substrate would occur.

### **2.21.2 Non-metallic coating**

In this case, non- metals are used as coating materials to protect surfaces of base materials. Common examples of non-metallic coating include plastic and rubber coating. Nonmetallic coating can be form of inorganic or organic coating. Inorganic coating involves oxidation (passivation), phosphating (which is a pre-painting resin, organic solvent and a pigment), lacquers (a thermoplastics dissolved in an organic solvent), coal tar and temporary coating.

### **2.22 Surface Coating by Metal Spraying**

Metal spraying which is also referred to as metallizing entails impregnation of a substrate (a base material) with a metal or metal compound by spraying the coating metal or compound on the surface of the substrate (base material). The metal to be used in depositing on the surface of the base material can be either in form of wire or powder. The metallic wire or powder is heated to a molten state in the thermal spraying gun, then sprayed onto the surface with compressed air or another gas to form a coating. Zinc and aluminum are the two metals that are most easily applied by thermal spray. The two metals, as well as their alloys, provide excellent corrosion resistance in a variety of marine and industrial environments. Prior to the coating process, the surface of the base material is first cleaned to guarantee adhesion of the sprayed metal on an even and uniform layer.

A thermal spraying gun is used to apply the coating (Lu *et al.*,2019).

Whether the metal to be deposited is in form of wire or powder, the coating metal is usually atomized before spraying it under pressure onto the substrate.

## CHAPTER THREE

### 3.0 MATERIALS AND METHODS

#### 3.1 Materials

The chemicals and reagents used in this investigation were purchased from Joe Chem Ventures, Nsukka, Enugu State, Nigeria. The chemicals and reagents were used in the synthesis of Zn metal nanoparticles and formulation of GSAC-Zn-Al-Ti composites. All chemicals and reagents used are of analytical grade with percentage purity in the range of 95, - 99.6% and no further purifications were done. The chemicals, reagents and other materials/equipment used during the investigation have been presented in Tables 3.1 and 3.2 respectively.

Table 3.1: List of reagents and their functions

S/N	Reagent	Function of reagent
1	Zinc chloride	Activating agent
2	De-ionized water	Mixture medium
3	Isopropyl alcohol	Preparation of titanium nanoparticles
4	Titanium isopropoxide	Precursor for preparation of titanium nanoparticles
5	Aluminum trichloride	Precursor for preparation of aluminum nanoparticles
6	Zinc acetate	Precursor for preparation of zinc nanoparticles
7	Ethanol	Mixture medium
8	Sodium hydroxide	For preparing zinc metal nanoparticles
9	Acetone	Groundnut shell activated carbon/metal nanoparticles mixture medium
10	Epoxy	Coating matrix
11	dimethylaminopropylamine	hardner
12	Hydrochloric acid	Corrosive medium

Table 3.2: List of materials/equipment and their functions

S/N	Name of Material	Function of Material
1	Groundnut shell	Metal nanoparticles support
2	Design Expert software (version 11.0)	For statistical analysis
3	OriginPro software 9.0	For plotting of graphs
4	Muffle furnace	For carbonization and activation
5	Electric weighing balance	For determining weight of samples
6	Oven	Drying of samples
7	Scanning electron microscope (ZEISS)	Sample surface analysis
8	PANalyticalX'Pert Pro diffractometer	Sample crystal phase analysis
9	MicroActive ASAP 2460 surface area analyser,	Surface area analysis
10	Perkin Elmer spectrum 100FT-IR spectrometer	Analysis of functional group of samples
11	DSC-TGA Q500 Universal V4.5A	Thermal decomposition analysis
12	Transmission electron microscope (TEM) (Jeol, JSM2010)	Particle size and distribution analysis
13	Magnetic stirrer	For stirring of mixtures.
14	Spray gun	For coating
15	100 mesh sieve	For groundnut shell particle size analysis

### **3.2 Methods**

Methods used include preparation of groundnut shell (GS) particulates, carbonization and characterization of the groundnut shell particulate and preparation of activated carbon from the GS precursor, taking into consideration the designed parameters for each activation process. Also undertaken was the characterization of the activated and calcined samples to evaluate the microstructural composition and behaviours (thermal behaviour, crystallinity, functional group and specific surface area) at different temperature and time. Zn, Al and Ti metal nanoparticles were also prepared and characterized before the coating procedures were carried out.

#### **3.2.1 Preparation of groundnut shell particulate**

Groundnut shell (see Plate 1) was obtained from groundnut sellers in Piako market in Minna, Niger State. The groundnut shell was washed three (3) times in tap water to remove dusts and other unwanted materials like dry leaves, stones and pieces of wood. The groundnut was then dried under sunlight for two weeks to remove moisture. At the end of the two weeks, 5.3kg of groundnut shell was available for further experiment. The groundnut was ground with a local grinding machine and oven-dried at 100°C for 24 hours. After drying in the oven, the size of the particles of the char that was produced as a result of the oven-drying was examined in line with ASTM-60. Weighed 600g of groundnut char was placed into a set of sieves arranged in descending direction of fineness and shaken for 15 minutes which is the recommended time to attain complete classification of the char. The particles used were and those that passed through the 48µm

sieve, therefore the particle size of the char used was  $< 48\mu\text{m}$ . This particle size was selected because  $48\mu\text{m}$  sieve was the least sieve size that was available where the sieving process was performed.



Plate I: Photograph of groundnut shell being sun-dried

### **3.2.2 Carbonisation of groundnut shell particulates**

A crucible was filled with a known weight (400g) of sieved particles of groundnut shell (precursor) and placed in a furnace and the temperature raised gradually from room temperature to  $200^{\circ}\text{C}$  in nitrogen (99.99%) flow having a flow rate of 150 ml/min. This temperature was made to remain constant for 3 hours so that char would be produced. The resulting char was allowed to cool down to room temperature before being stored in air-tight containers for further treatment.

**3.3 Microstructure Analysis of Carbonized Groundnut Shell Particulates** The X-ray fluorescence (XRF) and Scanning electron microscope (SEM) analysis of the carbonized groundnut shell particulate were conducted. The XRF analysis was carried out so to ascertain and quantify the chemical elemental in the carbonized groundnut shell sample while the SEM analysis was performed to examine the surface morphology of the carbonized sample.

#### **3.3.1 X-ray fluorescence (XRF)**

The X-Ray Fluorescence (XRF) analytical method was utilized in determining the elemental composition of the prepared groundnut shell char. The analysis was performed using a Spectro XLab Pro 2000. A known weight (6 g) of the sample was placed onto the special holder in the spectrometer to start the experiment. The analyser has the capacity to produce high X-ray intensity for quantitative analysis of the elements in the. The sample atoms are excited with this high x-ray radiation and the resulting characteristics x-rays are measured. The process lasted for about 25 minutes to obtain a spectrum for the energy and intensity of the emitted x-rays. Based on the data obtained the elemental composition of the sample was calculated. XRF analyzer determined the chemistry of the sample through measurement of the fluorescent X-ray emitted from the sample after it was excited by a primary X-ray sample.

#### **3.3.2 Scanning electron microscope (SEM) analysis**

The surface morphology of the sample was examined using ZEISS SUPRA 35VP scanning electron microscope (Shamsuddin *et al.*, 2016). The sample (10g), was placed onto aluminum stubs by means of carbon tappe placed on the stub. The samples were then

coated with 20nm thick layer of gold to prevent charging and the stubs were then put into the vacuum chamber of the equipment where the analysis was done at magnifications in the range of 1500x to 5000x using a Polaron Equipment limited model E500, which was set at an electric voltage of 1.2kV (10 mA) and vacuum 20 Pa for 10 minutes of the analysis. The digitized image was obtained.

### **3.4 Design of Experiment for Preparation of GS Activated Carbon**

For the purpose of this work, a Central Composite Design (CCD) which is designed for response surface methodology (RSM) was used to ascertain the effects of individual experimental variables and their interactive influences on the response (percentage carbon yield) in preparing activated carbon from groundnut shell. The highest yield that is achievable can be increased through the optimization of the production variables namely activation temperature, activation time and impregnation ratio (Azargohar and Dalai (2005); Wu and Tseng (2006)).

Three experimental variables which are activation temperature (A), activation time (B) and impregnation ratio (C) were investigated in this work. The Central Composite Design (CCD), apart from the 3 level factors has axial or star point which is usually denoted by  $\alpha$  which increases the number of levels to be studied to 5, thereby giving the experimental design flexibility. The number,  $N$  of experiments based on the Central Composite Design (CCD) is given by Equation (3.2).

$$N=2^n + 2n + n_c \tag{3.1}$$

where  $N$  denotes the total number of experiments  $n$  is the number of independent variables and  $n_c$  is the number of center runs used in the experiment.

20 experiments are required in order to analyze the influence of the three experimental variables. The experimental runs comprise 8 factorial points, 6 axial points and 6 replicates at the center points. In this investigation, 6 center runs were used as the case with Yahaya *et al.* (2010); Chowdhury *et al.* (2012). Therefore, 20 experimental runs were obtained by substituting the values of  $n$  (3) and  $n_c$  (6) in Equation (3.1).

In order to reduce to the barest minimum the influence of uncontrolled factors in the experiment, the sequence of the experiment was randomized as suggested by Sumathi *et al.* (2009). Replicates at the center points were used to estimate residual error and the reproducibility of the data.

Response of interest which is percentage carbon yield was calculated using Equation (3.2).

$$\text{Yield (\%)} = \frac{W_f}{W_i} \quad (3.2)$$

where  $Y$  (%) is the percentage yield,  $W_f$  is the final weight of activated carbonized groundnut shell char and  $W_i$  is the initial weight of carbonized groundnut shell char before activation.

The design matrix which contains the actual and coded levels of the experimental variables being studied was generated using the central composite design and presented in Table 3.3. Table 3.3 was generated after inputting all required information such as number

and names of numerical factors, number and name of response, number of center points and the range of levels to be considered. The software automatically generated the lower and upper levels. The 20 experimental runs were strictly performed in line with the experimental conditions presented in Table 3.3. Response of percentage groundnut shell carbon yield for each experimental run was calculated using Equation 3.2 and inputted into the empty response column of the software for further analysis.

Table 3.3: Design matrix for preparation of groundnut shell activated carbon

Run	Type of Point	Levels			Activated Carbon Preparatory		
Variables		(Coded Factors)			(Actual		
Factors)					Temperature	Time	
Ratio							
A (°C)	B (Hr)	C					
1	Fact	-1	-1	-1	600	1	1
2	Fact	+1	-1	-1	800	1	1
3	Fact	-1	+1	-1	600	3	1
4	Fact	+1	+1	-1	800	3	1
5	Fact	-1	-1	+1	600	1	3
6	Fact	+1	-1	+1	800	1	3
7	Fact	-1	+1	+1	600	3	3
8	Fact	+1	+1	+1	800	3	3
9	Axial	-1.682	0	0	531.82	2	2
10	Axial	+1.682	0	0	868.18	2	2
11	Axial	0	-1.682	0	700	0.32	2
12	Axial	0	+1.682	0	700	3.68	2
13	Axial	0	0	-1.682	700	2	0.32
14	Axial	0	0	+1.682	700	2	3.68
15	Center	0	0	0	700	2	2
16	Center	0	0	0	700	2	2
17	Center	0	0	0	700	2	2
18	Center	0	0	0	700	2	2
19	Center	0	0	0	700	2	2
20	Center	0	0	0	700	2	2

---

The mathematical model and graphical analysis for the response (percentage groundnut shell carbon yield) with consequent statistical significance of the model were implemented using Design-Expert software (version 11.0 Stat-Ease, Inc., Minneapolis,

USA).

The response (percentage groundnut shell carbon yield) was, therefore, used to produce an empirical model that correlated the response to the three independent preparation variables by using a second degree polynomial equation 3.3

$$Y=b_0 + \sum_{i=1}^n b_{ixi} + (\sum_i^n b_{iixi})^2 + \sum_{i=1}^{n-1} \sum_{j=i+1}^n b_{ijxixj} \quad (3.3)$$

where  $Y$  stands for the predicted response,  $b_0$  is the constant coefficient,  $b_i$  denotes the linear coefficient,  $b_{ij}$  is the interaction coefficient,  $b_{ii}$  is the quadratic coefficient and  $x_i, x_j$  are the coded values of the activated carbon preparation variables (Myers and Montgomery (2002), and Zainudin *et al.*, (2005).

### 3.5 Preparation of Activated Carbon

The method used by Yahaya *et al.* (2010); Tan *et al.* (2008) Chowdhury *et al.* (2012) was adopted in preparing the activated carbon from groundnut shell char. Prior to mixing with groundnut shell char,  $ZnCl_2$  pellets was dissolved in 250ml of de-ionized water. The activation steps were similar to those of carbonization process. The char produced from carbonization was mixed with  $ZnCl_2$  pellets at different impregnation ratios (IR), as calculated using Equation (3.1). At the end of each procedure, the activated sample was

cooled to room temperature under nitrogen flow. After cooling, the excess  $ZnCl_2$  in the sample were leached out by immersing it in 1M HCl solution for 24 hours. It was then washed again several times with de-ionized water till the ph of the solution that was washed got to 6.5.

### **3.6 Determination of Percentage Carbon Yield**

Dried weight of activated carbon sample was recorded as  $W_i$  before it was impregnated and loaded into the furnace. At the end of each activation process the final weight of the retrieved sample was measured as  $W_f$ . Response of percentage groundnut shell carbon yield for each experimental run was calculated using Equation 3.2 as earlier stated.

### **3.7 Proximate Analysis of GSAC**

The proximate analysis of prepared GSAC to ascertain the moisture content, volatile matter and ash content of the sample was undertaken using thermogravimetric analyser (Perking Elmer TGA7, US). 25 mg of GSAC were placed in a platinum crucible on the pan of a microbalance and heated between 22 and 990°C at a heating rate of 10°/min and weighed constantly for proximate analysis results.

### **3.8 Analysis of Experimental Result**

After inputting the results of the calculated groundnut shell percentage yield into the software, the results were analyzed to know which parameters were significant or not and also to determine if the model of the experiment is significant or not. This was done on the *design (Actual)* component of the software which contains the actual experimental design of 20 columns. The experimental design was first changed to standard order

arrangement from the initial run order arrangement by making use of the *view* menu and clicking *standard order*. Further analyses of the results were performed using the *summary*, *graph columns* and *evaluation* menus of the software. The *summary* menu gave the summary of the experimental design which includes the type of design. The *graph column* menu showed in graphical terms, the relationships of the various experimental variables against the response of groundnut shell percentage carbon yield. The *evaluation* menu showed the summary of the analysis of the experimental design which includes the model, results and graphs.

### **3.9 Optimization of Experimental Variables for Groundnut Shell Activated Carbon Preparation**

Part of the first objective of this investigation is to optimise the experimental parameters for optimum GSAC yield. Outstanding adsorption efficiency coupled with adequate product yield is desired in the production of commercial activated carbon (Chowdhury *et al.*, 2012). Therefore, in this investigation, experimental variables were optimized order to obtain the maximum response possible. To achieve this, the *numerical* menu in the optimisation section of the Design-Expert software version 11.0 (STAT-EASE Inc Minneapolis, LTS) was selected. Yield being the response was set at maximum whereas the values of the three variables (activation temperature, activation time and impregnation ratio) were fixed in the ranges being studied. After model simulation, 41 sets of experimental variables were suggested by the software. Therefore, the conditions of experiment that offered the maximum yield/desirability were selected for validation.

### 3.10 Model Validation

The conditions of experiment that offered the maximum yield/desirability from the optimization process were used to carry out activation procedure. The GSAC percentage yield obtained from the experiment was calculated to validate the predicted result and the percentage was error determined.

### 3.11 Calcination of GSAC Sample

A known amount (80g) (Chowdhury *et al.*, 2012) of groundnut shell activated carbon prepared under the optimal activation temperature, activation time and impregnation ratio of 600°C, 1.32 hour and 3 respectively was collected a graphite crucible and put in the furnace for calcination at different temperature of 700 and 800°C and time of 1 and 2 hours. Based on 2<sup>2</sup> factorial design, 4 calcination procedures were carried out as shown in Table 3.4.

Table 3.4: Experimental design table for GSAC calcination

Stand. Run	Run	Temperature (°C)	Time (hr)
4	1	800	2
1	2	700	1
3	3	700	2
2	4	800	1

### 3.12 Characterisation Techniques

The X-ray diffraction (XRD), Brunett-Emmett-Teller (BET), scanning electron microscopy (SEM), fourier transform infrared (FTIR) and thermogravimetric (TGA)

analyses were carried out on the calcined (UC) and uncalcined (C71, C72, C81 and C82) samples to determine their crystallinity, surface area, agglomerated particle size/pores distribution, functional groups and thermal stability. Results obtained were discussed and compared.

### **3.12.1 The X-ray diffraction (XRD) analysis**

The crystal phases and the crystallite size of the calcined samples were ascertained using X'Pert HighScore PANalytical X-ray diffractometer with Cu K $\alpha$  radiation. The calcined sample was rotated at exactly one-half of the angular speed of the receiving slit, so that the constant angle between the incident and reflected beams is maintained. The receiving slit is fixed in front of the counter on the counter tube arm, and behind it is usually fixed a scatter slit to guarantee that the counter collects radiation only from the portion of the specimen illuminated by the primary beam. The intensity diffracted at the numerous angles was automatically recorded on a chart and the appropriate ( $\Theta$ ) and (d) values were taken.

### **3.12.2 Scanning electron microscopy (SEM) analysis**

The surface morphologies of the calcined samples were examined using a VEGA3 TESCAN SEM. About 0.05 mg was spread on carbon adhesives tape and sputter that was coated with Au-Pd using a Quorum T150T for 5 min and the microscope was operated with electron high tension at 20.0 kV for imaging to identify the morphology of the sample's surfaces.

### 3.12.3 Fourier transform infrared (FTIR) analysis

The FT-IR spectra of the samples were obtained using the SHIMADZU spectrophotometer instrument. In preparing the sample, potassium bromide (KBr) pellet method which involved mixing 10 mg of GSAC with 100 mg of dried spectroscopic grade was used. The already ground KBr was pressed into a pellet by applying a pressure of 10 tonnes 2 minutes (Anyika *et al.* 2017). The transparent pellet was dried in an oven at 30°C overnight and then inserted into the instrument to record the spectra over the range of 4000 – 250  $\text{cm}^{-1}$ . The spectra were recorded at room temperature with the wave number range of 4000 –250 ( $\text{cm}^{-1}$ ).

### 3.12.4 Thermogravimetric analysis (TGA)

TGA technique was used to measure the mass variation of GSAC sample due to temperature change (Anyika *et al.*, 2017). It was performed using PerkinElmer STA8000

Simultaneous Thermal Analyser fitted with Pyris software for analysis of obtained data under well-ordered atmosphere of nitrogen to eliminate combustion of GSAC sample. A known weight of 15 mg of GSAC was subjected to heat in a furnace operating at temperature range of 25 to 1600°C. With measured weight of GSAC placed in the sample crucible and an empty crucible placed on the reference arm of the scale of the analyser, the weight sensor detected and recorded in microgram, the level of weight change due to GSAC loss or the oxidative gain. Nitrogen was used in the experiment as purge gas at flow rate of 100 mL/min with the analysis performed at a low decomposition rate of 20

°C/min

### 3.12.5 Brunauer-Emmett-Teller (BET) analysis

The specific surface area of calcined GSAC sample was determined using multipoint BET surface areas. Analysis was performed by nitrogen adsorption at 77 K using Quantachrome Autosorb Automated Gas Sorption system which is a surface area analyzer.

Prior to the analysis, out-gassing procedure was done at 350 °C for 4 hours to eliminate any volatile material or vapour that may still be in the sample and which could interfere with the measurement. The out-gassing procedure is vital in a bid to obtain the desired precision and accurate specific surface area analysis (Anyika *et al.*, 2017). After the out-gassing procedure, the sample tube was removed, the stopper was inserted and the weight of the GSAC sample recorded. The sample tube was fixed onto the volumetric apparatus, and the sample ejected; down to the specific pressure within the range of 2 Pa and 10 Pa.

### **3.13 Synthesis of Zinc, Aluminum and Titanium Nanoparticles**

The Sol- gel method as used by Kamilet *al.* (2016) was employed to synthesize zinc, aluminum and titanium nanoparticles.

#### **3.13.1 Synthesis of titanium nanoparticles**

To synthesize titanium oxide nanoparticles using the sol gel method, 100 mL of isopropyl alcohol was put into 15 mL of titanium isopropoxide and the mixture stirred for 10 minutes. To this mixed solution, 10 mL of de-ionized water was added drop wise. The mixture solution was then stirred continuously for 2 hours. The gel formed was left for 24 hours in dark and then dried. The dried titanium nanoparticles were calcinated at 550 °C to achieve the needed result. The formation and morphology of titanium nanoparticles and particle sizes was confirmed by TEM analysis and SEM analysis respectively.

### **3.13.2 Synthesis of aluminum nanoparticles**

To Synthesize aluminum nanoparticles using sol-gel method, aluminum trichloride was used as the precursor. 28% of ammonia was introduced drop wise to stirred ethanolic solution of aluminum chloride (0.1M). The formed gel was left to mature for 30 hours at room temperature after filtering in vacuum chamber, drying at 100 °C for 24 h in an oven, and annealing at 1000°C. The formation and morphology of alluminum nanoparticles was confirmed by TEM analysis and SEM analusis respectively.

### **3.13.3 Synthesis of zinc nanoparticles**

The sol-gel method was again used to synthesize zinc nanoparticles. Zinc acetate dehydrate ( $\text{Zn}(\text{CH}_3\text{COO})_2 \cdot 2\text{H}_2\text{O}$ ) servedas precursor material and ethanol ( $\text{CH}_2\text{COOH}$ ) as solvent, 2M sodium hydroxide (NaOH) and distilled water was used as medium.

Similar steps as described in preparation of Ti and Al nanoparticles were repeated. TEM and SEM analysis of resulting sample were performed to confirm the presence of zinc nanoparticles.

## **3.14 Characterisation of Prepared Metal Nanoparticles**

The surface morphological and the average particle size evaluation of the prepared metal nanoparticles were evaluatedusing the scanning electron microscopy (SEM) andtransmission electron microscopy (TEM) techniques.

### **3.14.1 Scanning Electron Microscope (SEM)**

To perform the surface morphological analysis of the sample using ZEISS SUPRA 35VP Field Emission scanning electron microscope, the samples were placed onto aluminum

stubs by means of carbon tape placed on the stub. The stubs were then put into the vacuum chamber of the equipment for 10 minutes of analysis at magnifications in the range of 1500x to 5000x using a Polaron equipment limited model E500 set at a electric voltage of 1.2kV (10 mA) and vacuum pressure of 20 Pa.

### **3.14.2 Transmission Electron Microscope (TEM) analysis**

TEM analysis was performed out using Philips GM-30 electron microscope. A known weight (10 g) of sample was spread in deionized water. A drop of thin dispersion was set on a staining pad. Facing up, the coated side of a carbon coated copper grid is inserted into the drop. After 10 minutes, the grid is removed and sun-dried. The UTHSCA Image version 300 software was used to test the particle size distributions

### **3.15 Development of Zn-Al-Ti Nanocomposites Supported GSAC**

Mixture ratios of 3:1, 1:1 and 1:3, representing 75:25 %wt, 50:50 %wt and 25:75%wt respectively was used in the formulation of GSAC/metal nanoparticles system (Vineetha *et al.*, 2018). However, introduction of the metal nanoparticles was iterative, starting with Zn metal nanoparticles and converging with Ti metal nanoparticles. The mixtures were stirred vigorously to achieve even dispersion of the participating particles. Stoichiometry and homogeneity are based on the ability of mixed precursors to form a single molecular species, particularly when water is added, so that ions are distributed evenly (Pramesh *et al.*, 2004).

### 3.15.1 Development of GSAC/ Zn metal nanoparticles composition

In the first instance, Zn metal nanoparticles were introduced onto GSAC at the working ratios of 3:1, 1:1 and 1:3. Each of the different ratios of the mixtures was dissolved in 50ml of acetone and stirred vigorously using a magnetic stirrer that operated at 30rev/min for 25 minutes to achieve homogeneity and even distribution of mixed particles. The slurry formed was heated in the oven at 60°C for 4 hours to eliminate acetone (Lusi *et al.*, 2017). X-ray diffraction (XRD) technique was used to determine the sample with the smallest average crystallite/grain size among the three (3) samples. Irfan *et al.* (2018) posited that the average crystallite/grain sizes ( $D$ ) of the different mixtures were calculated from XRD results using Scherrer formula given in Equation (3.6).

$$D = \frac{K\lambda}{\cos\theta} \quad (3.6)$$

where  $D$  stands for the average crystallite size (nm),  $K$  denotes the shape factor ( $K =$

0.94),  $\lambda$  is the x-ray wavelength in nanometer (nm) represents the full width at half maximum (FWHM) in radians and  $K$  is a constant related to crystallite shape, normally taken as 0.9.  $\theta$  which is the expanded diffraction peak measured at full width at half maximum (FWHM) is in radians. The properties of nano-structured deposits are strongly grain size dependent (Muralidhara *et al.*, 2011). Therefore, from the results obtained, the ratio with the smallest average crystallite/grain size was used as the base sample for introduction of Al nanoparticles.

### 3.15.2 Development of GSAC-Zn /Al metal nanoparticles composition

Al metal nanoparticles were introduced onto GSAC/Zn metal nanoparticles sample of mixture ratio of 3:1 which gave the smallest average crystallite/ grain size. Al metal nanoparticles were equally introduced onto the GSAC/Zn formulation at mixture ratios of 3:1, 1:1 and 1:3. Each set of the newly formulated GSAC-Zn/Al mixture was again dissolved in 50 ml of acetone and mixed using a magnetic stirrer at 30rev/min for 25

minutes to achieve homogeneity and even distribution of mixed particles. The slurry formed was heated in the oven at 60 °C for 4 hours to eliminate acetone. X-ray diffraction (XRD) analysis was performed on the three mixtures. From the XRD results obtained, the crystallite/grain sizes ( $D$ ) of the different mixtures were calculated using Scherrer formular in Equation (3.6) to determine the mixture sample with the smallest average crystallite/grain size for further investigation.

### **3.15.3 Development of GSAC-Zn-Al/Ti metal nanoparticles composition**

Ti metal nanoparticles were introduced onto GSAC-Zn/Al metal nanoparticles sample of mixture ratio of 3:1 which gave the smallest average crystallite/ grain size. Ti metal nanoparticles were equally introduced onto the GSAC-Zn-Al formulation at mixture ratios of 3:1, 1:1 and 1:3. Each set of the newly formulated GSAC-Zn-Al/Ti mixture was again dissolved in 50 ml of acetone and mixed using a magnetic stirrer at 30rev/min for 25 minutes to achieve homogeneity and even distribution of mixed particles. The slurry formed was oven-heated at 60 °C for 4 hrs to eliminate acetone. X-ray diffraction (XRD) analysis was performed on the three samples. From the XRD results obtained, the crystallite/grain sizes ( $D$ ) of the different mixtures were calculated using Scherrer formular in Equation (3.6) to determine the mixture sample with the smallest average crystallite/grain size. At this point all 3 metal nanoparticles of Zn, Al and Ti have been

successfully mixed together; therefore, the GSAC-Zn-Al/Ti formulation of 1:1 mixture ratio which gave the smallest crystallite/grain size was used for coating procedure.

### **3.16 X-Ray Photoelectron Spectroscopy (XPS) Analysis**

The X-Ray Photoelectron Spectroscopy (XPS) investigation was performed using ultrahigh Vacuum chamber (Fisons Instruments) MT-500 with a non-monochromatic Al X-ray radiation ( $\text{K}\alpha$  1486.6 keV) a CLAM-2 hemispheric analyzer for electron detection at a base pressure of  $7 \times 10^{-9}$  mbar. The samples were supported on a carbon adhesive tape and were irradiated with the high intensity source. A fraction of the electrons produced near the surface escape into vacuum and reach the spectrometer's analyzer slit, which measures electron current (the number of electrons per unit time) as a function of their energy. The plot of intensity against energy relates to the XPS. For the determination of the binding energy, a background correction was applied.

### **3.17 Mild Steel Samples Preparation**

AISI 1015 steel was used for the investigation. The AISI 1015 Steel was mechanically cut into small coupons measuring 20 mm x 20 mm x 20 mm and then polished using 50 grit size emery papers to remove unwanted materials such as rusts and dusts from the metal surface. The polished samples were characterized for elemental composition and then heat treated (annealing) to remove residual stresses which the metal may have acquired during cutting.

### **3.17.1 Heat treatment of mild steel samples**

For the purpose of releasing the mild steel samples of any residual stresses gained during cutting, four (4) sets (with each set having four samples) of the mild steel samples were heated at four different temperatures of 500, 550, 600 and 650°C for 1 hour (Nurudeen and Oluleke, 2013). After annealing, the hardness values of the mild steel samples were evaluated using the Indentec Hardness Testing Machine. The set of annealed mild steel sample with the highest hardness value was used for further experiments.

### **3.18 Coating of Mild Steel**

Annealed mild steel samples were dipped into acetone to remove any grease or oil on the mild steel surface. Epoxy resin was modified novolac and the curing agent was dimethylaminopropylamine. Habeeb *et al.* (2018) reported that epoxy and curing agent mixed at a ratio of 2:1. GSAC-Zn-Al/Ti were incorporated into the epoxy/curing agent mixture at five (5) different concentrations of 1, 2, 3 and 4 wt.% which was similar to the composition by weight presented by Khodaei *et al.* (2019) when investigating the anti-corrosion property of epoxy-based nanocomposite coating reinforced by a zeolite complex on mild steel in 1M HCl.

The coating was applied using spraying gun and after drying (at ambient temperature for 24 hours). At the center of the cold spray equipment is gun mechanism, which was equipped with a high-pressure gas pipeline, a heater, a powder feeding pipe and a nozzle 2 mm in diameter. The coating thickness was determined using Minitest 600 Erichsen digital meter. The coatings were heated in an oven at temperature of 100°C for 1 hour to re-arrange the microstructure of the coatings.

### 3.19 Coatings Hardness Test

The Indentec hardness testing machine was used to determine the hardness values of steel samples coated with different amounts (1, 2, 3 and 4wt.%) of GSAC-Zn-Al-Ti in epoxy. For each sample, 5 hardness tests were carried out and the average was recorded. Data from the tests were collected and compared with result obtained from hardness test carried out on uncoated mild steel sample. A bar chart of hardness against weight composition was produced.

### 3.20 Coatings Porosity Test

The ISO 10545 procedure (water absorption method) for determining porosity which was used by Andreola *et al.* (2000) was adopted in carrying out the porosity test. The method involved weighing 5 mild steel (4 coated with different concentrations of GSAC-Zn-AlTi/epoxy and the neat epoxy coated sample) dry samples and immersing them in boiling water for 2 hours. Sample dry weight,  $W_d$  was recorded. The heating system was shut off, and the samples were left in water for 4 hours (water immersion time) to cool naturally and achieve saturation. The samples were taken out of the water, and any excess moisture on their surfaces was wiped away with a damp cloth. Their wet masses were then measured and reported as  $W_w$ . Data from the tests were collected and the porosity values of samples were determined using the formula presented in Equation 3.6 (Andreola *et al.*, 2000).

$$W. A. (\%) = \frac{W_w - W_d}{W_d} \times 100 \quad (3.7)$$

where  $W. A.$  is the water absorption/porosity (%),  $W_w$  is the sample weight after boiling in water and  $W_d$  is the dry sample weight.

### **3.21 Corrosion Test of Ucoated and Coated Steel Samples**

For the purpose of this investigation, the corrosion test was carried out on 6 mild steel samples (1 uncoated mild steel sample, 1 mild steel sample coated with only epoxy and 4 samples of mild steel coated with different ratios of GSAC-Zn-Al-Ti/Epoxy. Six samples in all were used to carry out the investigation using the electrochemical impedance spectroscopy method of corrosion testing (Habeed *et al.*, 2018). Under static conditions, the electrochemical measurement was performed using a Voltlab (Tacussel-Radiometer PGZ 100) potentiostat managed by Tacussel corrosion analysis software model (Voltmaster 4). The corrosion test set-up was made up of three electrodes. A white saturated calomel electrode (SCE) served as the reference electrode. The auxiliary electrode was platinum, and the working electrode (to which the sample was connected) was carbon steel. The reference electrode was used to refer to all potentials in this analysis. To create a steady state open circuit potential ( $E_{opc}$ ), the working electrode was dipped in 1M HCl for 30 minutes. The electrochemical measurements were carried out after the  $E_{opc}$  measurements. Every electrochemical experiments were carried out at room temperature in an aerated solution. The EIS experiments were performed in a frequency range with a high limit of 100 kHz and a separate low limit of 0.1 Hz at open circuit potential, with 10 points per decade, at the rest potential after 30 minutes of acid immersion by applying 10 mV ac voltage peak-to-peak after 30 minutes of acid immersion. Corrosion tests on uncoated steel, epoxy coated steel, 1:1, 1:2, 1:3, and 1:4

epoxy enhanced Zn-Al-Ti/GSAC coated steel were used to build Nyquist plots. The characteristics of the Nyquist plots obtained was used to interpret the findings.

## **CHAPTER FOUR**

### **4.0 RESULTS AND DISCUSSION**

#### **4.1 Characterisation of Groundnut Shell Particles**

##### **4.1.1 SEM-EDS analysis of carbonized groundnut shell particulate**

SEM micrograph and elemental composition of carbonized groundnut shell particulate was obtained using the ZEISS scanning electron microscope (SEM) fitted with Energy

Dispersive X-ray Spectroscopy (EDS) and the results presented in Figure 4.1 and Table 4.1 as shown in Figure 4.1 and Table 4.2

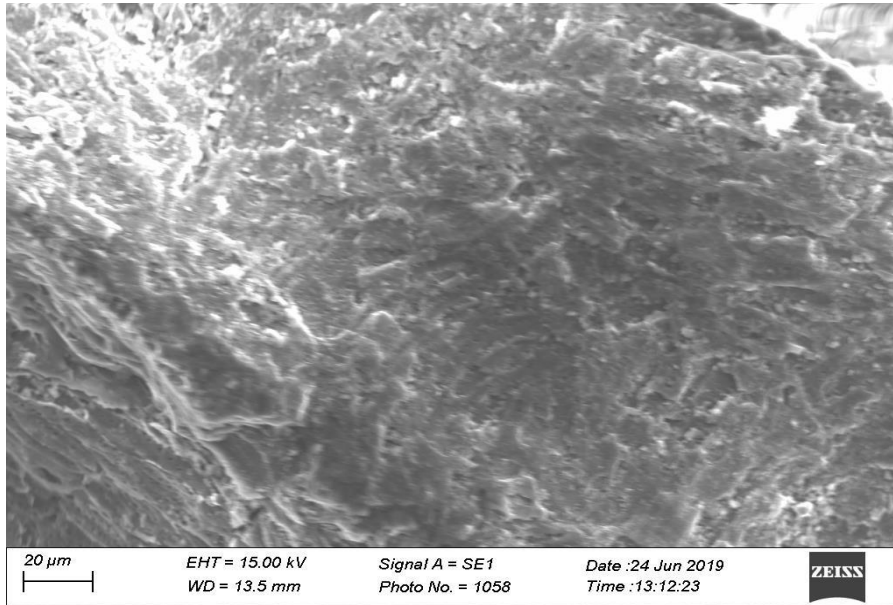


Figure 4.1: SEM micrograph for carbonized groundnut shell particulate

As observed from the SEM micrograph in Figure 4.1, there is absence of porous surface. However, a few flake structures and some rudimentary pores were noticed on the sample surface. The absence of micro pores on the carbonized sample surface could be related to the absence of activating agent to penetrate into the structure of the carbonized sample, thereby necessitating the development of tiny pores (Mohammed *et al.*, 2015).

Table 4.1: Elemental Composition of Carbonized Groundnut Shell Particulate as Determined by SEM-EDS

Element	Weight (%)	Atomic (%)
C	43.89	55.91

N	27.99	30.58
O	2.73	2.61
Mg	1.69	1.07
Al	0.79	0.45
Si	1.03	0.81
P	1.45	0.72
S	1.8	0.86
K	7.01	2.74
Ca	11.6	4.26

---

The SEM-EDS result revealed the predominant presence of carbon (43.89wt. %) as expected. The presence of nitrogen as one of the major constituents at 27.99wt. % composition confirms the source of the precursor as hemicellulosic.

#### 4.1.2 X-ray fluorescence (XRF) analysis

The XRF analysis of groundnut shell particulates was carried out and the result represented in the Table 4.2

Table 4.2: X-Ray Fluorescence (XRF) analysis of groundnut shell particles

Element	Composition (wt%)
1	Al <sub>2</sub> O <sub>3</sub> 6.46
2	SiO <sub>3</sub> 69.16
3	Fe <sub>2</sub> O <sub>3</sub> 6.20
4	MnO 0.08
5	ZnO 4.34
6	K <sub>2</sub> O 0.50

7	MgO	0.21		
8	P <sub>2</sub> O <sub>5</sub>	0.31		
9	Na <sub>2</sub> O	0.04		
10	SO <sub>3</sub>	0.23		
11	CaO	0.78		
12	V <sub>2</sub> O <sub>5</sub>	0.10		
13	Cr <sub>2</sub> O <sub>3</sub>	0.045	14 NiO	0.01
15	ZnO	0.07		
16	Ga <sub>2</sub> O <sub>3</sub>	0.01		
17	SrO	0.01		
18	Y <sub>2</sub> O <sub>3</sub>	0.01		
19	ZrO <sub>2</sub>	0.32		
20	Nb <sub>2</sub> O <sub>5</sub>	0.02		
21	Cl	10.02	22 Cu	0.01

---

The X-Ray Fluorescence (XRF) analysis result presented in Table 4.2 confirmed that SiO<sub>2</sub>, Fe<sub>2</sub>O<sub>3</sub>, ZnO and Al<sub>2</sub>O<sub>3</sub> with 69.16, 6.20, 4.34 and 6.46% respectively were seen to be major constituents of the ash/particulate. Silicon dioxides are known to be among the hardest substances with a melting point of 1600°C. Some other oxides like MnO, K<sub>2</sub>O, CaO, Mg and P<sub>2</sub>O<sub>5</sub> were also discovered to be present in small amounts. The presence of such hard element as SiO<sub>2</sub> in high weight percentage suggested that the groundnut shell particles can be used for manufacturing of engineering material where hardness is desired property.

#### 4.2 Chemical Activation of Groundnut Shell Char

The experimental design matrix showing groundnut shell actual and predicted percentage carbon yield is presented in Table 4.3. The actual percentage yield values are the laboratory results obtained using equation 3.5 while the predicted yield values were software generated.

Table 4.3: Groundnut shell actual and predicted carbon yield values

Run	Temperature A (°C)	Time B (hr)	Ratio C	Actual Yield (%)	Predicted Yield (%)
1	700.00	2.00	0.32	29.38	28.09
2	600.00	3.00	1.00	37.72	38.37
3	800.00	1.00	1.00	20.53	21.28
4	800.00	1.00	3.00	28.12	28.13
5	868.18	2.00	2.00	18.64	18.05
6	531.82	2.00	2.00	51.60	51.27
7	600.00	1.00	3.00	49.94	49.88
8	700.00	2.00	2.00	34.09	34.63
9	700.00	2.00	2.00	34.45	34.63
10	600.00	3.00	3.00	47.56	47.47
11	600.00	1.00	1.00	37.94	38.54
12	800.00	3.00	3.00	25.16	25.22
13	700.00	2.00	3.68	41.14	41.50
14	700.00	2.00	2.00	34.68	34.63
15	700.00	2.00	2.00	35.29	34.63
16	700.00	2.00	2.00	34.25	34.63
17	700.00	2.00	2.00	34.87	34.63
18	800.00	3.00	1.00	19.91	20.62
19	700.00	3.68	2.00	30.95	30.48
20	700.00	0.32	2.00	33.52	33.07

The run order for determination of percentage carbon yield of groundnut shell which has been presented in Tables 4.3 revealed the values of the response (actual and predicted).

To create a connection between the activated carbon preparation variables and carbon yield, Design Expert software's Central Composit Design (CCD) was used.

The experimental errors were calculated using six (6) center points. The experiment's series was randomized to reduce the influence of uncontrollable variables (Tan *et al.*, 2008). The highest percentage carbon yield of 51.27 percent was obtained using the

experimental variables of activation temperature, activation time, and impregnation ratio of 531.82°C, 2 hours, and 3 respectively, as shown in Table 4.3.

A model was chosen based on the highest order polynomial with major additional terms that was not aliased by the sequential model sum of square (Arami-Niya *et al.*, 2012;

Chowdhury *et al.*, 2011). As indicated by the software, a quadratic model was chosen. The regression coefficient for fitting the quadratic equation of the GS percentage carbon yield as generated by the software is shown in Table 4.4.

Table 4.4: Regression coefficient for groundnut shellpercentage carbon yield

---

Source	Sum of Squares	Degree of freedom	Mean Square	F Value	p-value Prob > F	
Model	1585.08	9	176.12	319.19	<	Significant
					0.0001	
A-Temperature	1331.98	1	1331.98	2413.99	<	
					0.0001	
B-Time	8.06	1	8.06	14.60	0.0034	
C-Ratio	217.08	1	217.08	393.43	<	
					0.0001	
AB	0.1203	1	0.1203	0.2181	0.6505	
AC	10.11	1	10.11	18.33	0.0016	
BC	2.52	1	2.52	4.57	0.0583	
A <sup>2</sup>	0.0014	1	0.0014	0.0025	0.9612	
B <sup>2</sup>	14.71	1	14.71	26.65	0.0004	
C <sup>2</sup>	0.0477	1	0.0477	0.0864	0.7748	
Residual	5.52	10	0.5518			

Based on the regression coefficient of groundnut shell percentage carbon yield in Table 4.4, the final empirical model in terms of the coded factors for the response of percentage carbon yield is represented by the following equation:

$$Y (\%) = 34.63 - 9.88A - 0.77B + 3.99C + 0.01A^2 - 1.01B^2 + 0.06C^2 - 0.12AB - 1.12AC - 0.56BC \quad (4.1)$$

The effect of one variable on yield response (Y) is represented by the coefficients for temperature (A), time (B), and impregnation ratio (C). The coefficients with second order terms and those with multiples of two variables show the interaction of the multiples of

two variables and the quadratic effect, respectively. A synergistic effect is indicated by a positive sign in front of the words, while an antagonistic effect is indicated by a negative sign.

### 4.3 Analysis of Variance (ANOVA) for GS Carbon Yield

Analysis of variance (ANOVA) of groundnut shell (GS) carbon yield was used to further justify the models' adequacy. Table 4.5 shows the results of the ANOVA for the quadratic model for GS carbon yield performed with the Design-Expert program (version 11.0, Stat-Ease, Inc, Minneapolis, USA).

Table 4.5: ANOVA for GS percentage carbon yield

Source	Sum of Squares	Degree of F	Mean F Square	F	p-value Value Prob	> freedom
Model	1585.08	9	176.12	319.19	< 0.0001	Significant
A-Temperature	1331.98	1	1331.98	2413.99	< 0.0001	
B-Time	8.06	1	8.06	14.60	0.0034	
C-Ratio	217.08	1	217.08	393.43	< 0.0001	
AB	0.1203	1	0.1203	0.2181	0.6505	
AC	10.11	1	10.11	18.33	0.0016	
BC	2.52	1	2.52	4.57	0.0583	
A <sup>2</sup>	0.0014	1	0.0014	0.0025	0.9612	
B <sup>2</sup>	14.71	1	14.71	26.65	0.0004	
C <sup>2</sup>	0.0477	1	0.0477	0.0864	0.7748	
<u>Residual</u>	<u>5.52</u>	<u>10</u>	<u>0.5518</u>			

The regression model's analysis of variance (ANOVA) reveals that the model is highly significant as proven from the calculated F-value and a very low probability value in Table

4.5. Where the value of Prob. > F less than 0.05, the model terms are viewed to be significant (Sahu *et al.*, 2010). The model *F*-value of 319.19 and Prob. > *F* less than 0.0001 implies that this model was significant. However, A, B, C, AC and B<sup>2</sup> were significant model terms while AB, BC, A<sup>2</sup> and C<sup>2</sup> were insignificant to the groundnut shell response of yield. Also from Table 4.5, it was observed that activation temperature (A), the activation time (B) and impregnation ratio (C), were significant on the response of yield. However, the activation temperature imposed the greatest influence on the response of yield with the highest *F*-value of 2413.99 and therefore, was the most significant factor during the activation process.

#### 4.4 Model Fits Statistics

The fit statistics of the developed model with respect to correlation coefficient R<sup>2</sup>, Adequate precision, standard deviation and other related parameters is presented in Table 4.6.

Table 4.6: Fit statistics

Std. Dev.	0.7428	R <sup>2</sup>	0.9965	Mean	33.99	Adjusted R <sup>2</sup>
						0.9934
C.V. %	2.19	Predicted R <sup>2</sup>	0.9774			
		Adeq Precision	63.2426			

The correlation coefficient, R<sup>2</sup>, and standard deviation values can all be used to determine the model's consistency. R<sup>2</sup> stands for the ratio of sum of the squares (SSR) to total sum of the squares (SST) and shows how well the model approximates experimental data

points (Myers and Montgomery, 2002). Developed model seems to be the best at low standard deviation and high  $R^2$  (Ahmad *et al.*, 2009). With  $R^2$  closer to 1, it implies that modal values are closer to response experimental values (Hushmand *et al.*, 2011).

Here, the model  $R^2$  value is given as 0.9965, signaling that 99.65% of the total variation in groundnut shell carbon yield could be due to the factors studied.

The value of 'Adequate Precision' which measures the signal to noise ratio was obtained as 63.2426. Adequate precision value more than 4 is desired (Hushmand *et al.*, 2011). The adequate precision value from Table 4.6 was given as 63.2426. In other words, the model can be used to traverse the design space (Chowdhury *et al.*, 2012). The predicted and experimental yield responses both had variance errors of less than 10%, which is well within the acceptable range.

#### **4.5 Optimization of the Experimental Variables**

The optimization procedure carried out using Design Expert software to show the selected experimental parameters and yield presented in Table 4.7. Here, the result of the experiment was analysed with the experimental variables modified to obtain the maximum targeted response of carbon yield.

Table 4.7: Optimization of experimental variables for groundnut shell carbon yield

Number	Temp	Time	Ratio	Yield	Desirability
1	600.000	1.000	3.000	49.882	0.987
2	600.001	1.010	2.999	49.886	0.985
3	600.001	1.000	2.991	49.830	0.985
4	600.758	1.000	3.000	49.799	0.985
5	600.001	1.029	3.000	49.905	0.983
6	600.000	1.000	2.976	49.744	0.983
7	601.914	1.004	3.000	49.677	0.982
8	600.002	1.039	3.000	49.913	0.982
9	600.003	1.000	2.967	49.694	0.981
10	600.000	1.053	3.000	49.923	0.980
11	603.355	1.007	3.000	49.523	0.979
12	603.810	1.000	3.000	49.467	0.979
13	600.000	1.055	2.991	49.870	0.979
14	600.000	1.069	3.000	49.934	0.978
15	600.001	1.006	2.952	49.611	0.978
16	600.000	1.078	3.000	49.940	0.977
17	604.888	1.000	3.000	49.350	0.976
18	600.000	1.096	3.000	49.951	0.975
19	600.000	1.102	3.000	49.953	0.974
20	606.430	1.000	3.000	49.181	0.973
21	600.000	1.116	3.000	49.963	0.973
22	600.024	1.129	3.000	49.968	0.971
23	607.859	1.001	3.000	49.027	0.970
24	610.101	1.000	3.000	48.782	0.965
25	600.000	1.000	2.874	49.156	0.965
26	612.303	1.000	3.000	48.542	0.961
27	600.001	1.000	2.826	48.876	0.957
28	600.003	1.000	2.806	48.760	0.953
29	600.000	1.277	3.000	50.030	0.952
30	616.376	1.000	3.000	48.098	0.952

31	600.000	1.284	3.000	50.032	0.951	
32	617.561	1.000	3.000	47.969	0.949	
33	618.408	1.009	3.000	47.884	0.946	
34	600.000	1.320	3.000	50.039	0.946	Selected
35	600.002	1.000	2.753	48.459	0.944	
36	610.511	1.000	2.866	47.978	0.942	
37	600.000	1.544	3.000	50.026	0.912	
38	600.000	1.000	2.413	46.507	0.879	
39	652.231	1.000	3.000	44.193	0.870	
40	600.001	1.000	2.160	45.059	0.826	
41	691.579	1.000	3.000	39.911	0.769	

The optimum GSAC yield was obtained using activation temperatures, activation times, and impregnation ratios of 600°C, 1.32hr, and 3 respectively, as shown in Table 4.7. The GSAC yield of the best activated carbon was about 50.04 percent.

#### 4.6 Model Validation

Table 4.8 shows the model validation result which was obtained after the optimized experimental variables were used to carry out activation procedures in the laboratory.

Table 4.8: Model validation result

Activation Impregnation	Activation Predicted	GSAC Yield (%) Experimental Error (%)			
Temp A (°C) Ratio C	Time B (Hr)				
600	1.32	3	50.04	49.75	0.58

The experimental value for percentage yield was near to the value expected by the model, with a relatively small error of 0.58 percent between the predicted and actual values, as shown in Table 4.8.

## 4.7 Proximate Analysis of GSAC

Table 4.9 summarizes the findings of GSAC's proximate study.

Table 4.9: Proximate analysis result for GSAC

S/N	Property	Value
1	pH	6.5
2	Moisture content (%)	2.5
3	Ash content (%)	7.5
4	Carbon yield (%)	49.75
5	BET average surface area (m <sup>2</sup> /g)	498.52

The moisture and ash contents were calculated as 2.5% and 7.5% respectively as can be seen in Table 4.9. Both values are within acceptable limits based on American Society of Materials and Testing (ASTM) D2867-11(2018).

## 4.8 Graphical Presentation of Experimental Results

### 4.8.1 Predicted yield values plot against actual values

Figure 4.2 displays a diagnostic plot of predicted yield values versus the actual or real yield values.

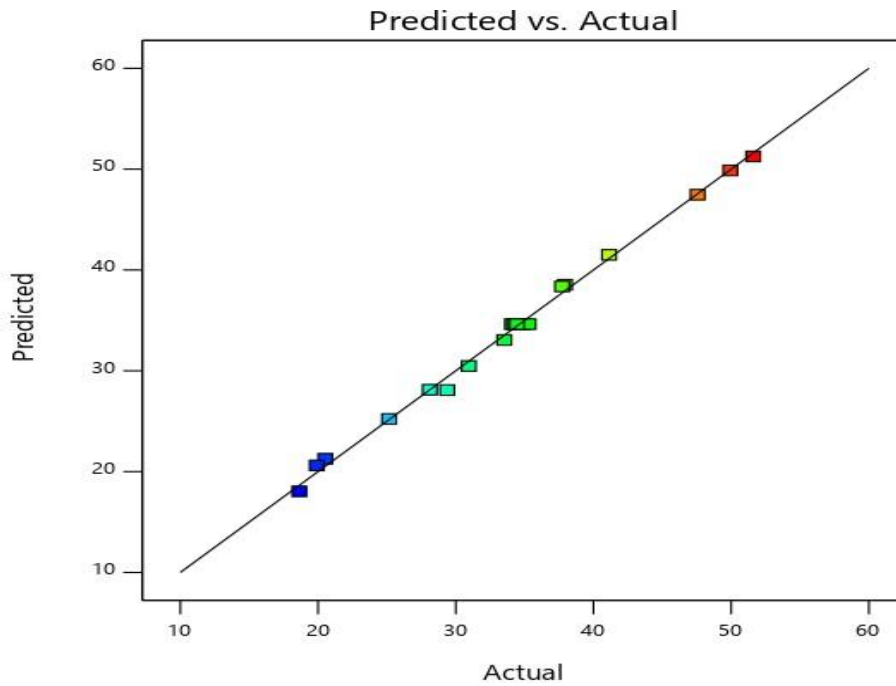


Figure 4.2: Predicted values plot against actual values of GS production yield

It was observed in Figure 4.2, that the predicted values for the percentage carbon yield were near their experimental values, reflecting good performance and suitability of the model represented in Equation 4.1. This might not be unconnected with the high  $R^2$  value obtained, which implied that the predicted value for GSAC yield would be more exact and nearer to its actual value (Nasehir *et al.*, 2010).

#### 4.8.2 Plot of studentized residual and predicted values

The studentized residuals and predicted plot showing the data points within the range of study is presented in Figure 4.3.

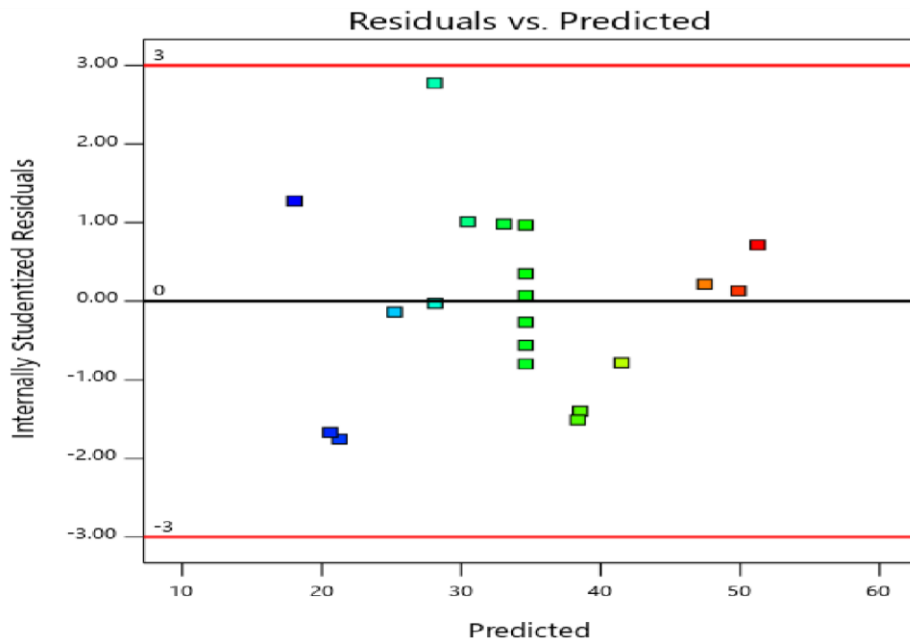


Figure 4.3: Studentized residual and predicted response plot for GS yield

Figure 4.3 shows that the data points in the plot are randomly distributed, suggesting that the variance of experimental observations was between  $\pm 3.00$ , meaning that no response transformation was needed for this study's experimental design (Myers and Montgomery, 2002).

#### 4.8.3 Outlier *t* plot for GSAC percentage carbon yield

The outlier *t* plot has been presented in Figure 4.4. The outlier *t* plots reflect a simple data recording error which sometimes show the region of independent variables where the fitted model has shown poor approximation to the true response surface (Myers and Montgomery, 2012).

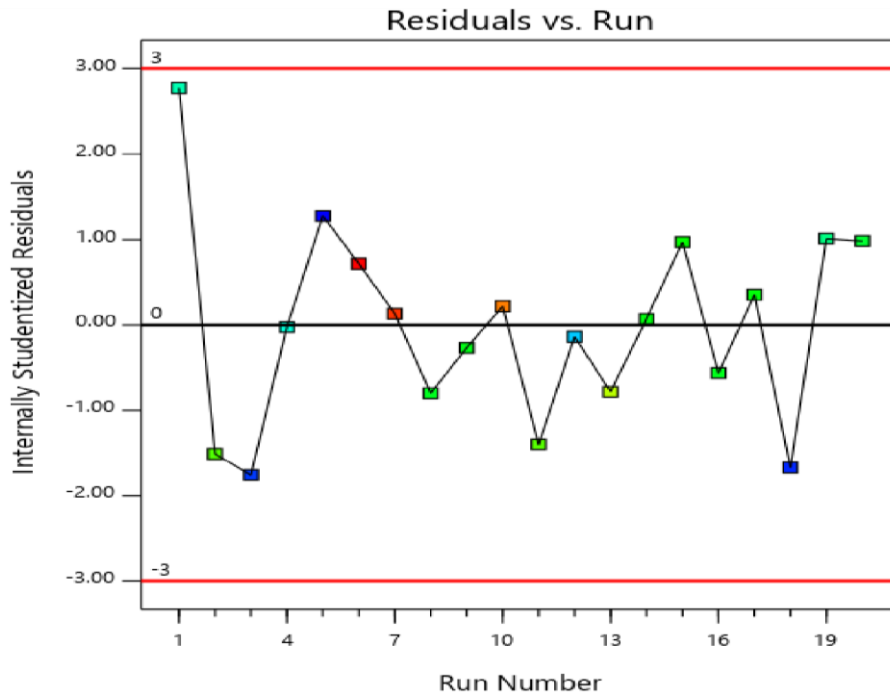


Figure 4.4: Outlier  $t$  plot for production of GS carbon yield (%)

All of the normal residuals in Figure 4.4 fall within the range of  $\pm 3.0$ . This means that the fitted model's (Equation 4.1) data approximation to the response surface was good and did not represent any data recording error.

#### 4.8.4 The 3-Dimension (3-D) plot showing effects of activation temperature and time on gs percentage carbon yield

Figure 4.5 shows a three-dimensional (3-D) plot of the effects of activation temperature and time on GSAC percentage yield. The plot shows that activation temperature has the most significant effect, with an  $F$ - value of 2413.99, and that activation time has a negligible effect, with an  $F$ - value of 16.60..

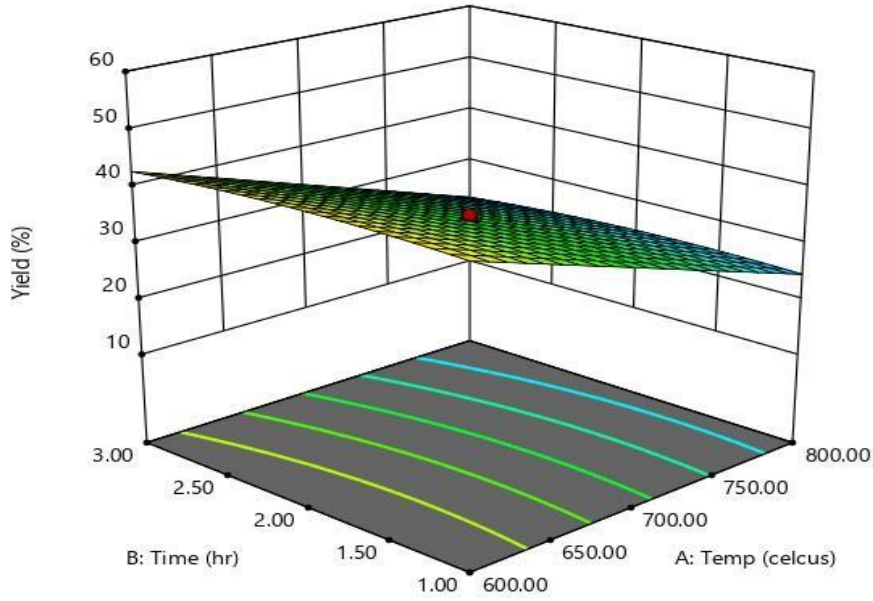


Figure 4.5:3-D response surface plot of GSAC yield (Effect of activation temperature and activation time)

The carbon yield of Groundnut Shell (GS) was found to decrease as activation temperature and time increased, with the Impregnation Ratio (IR) set at the midpoint (IR =2.0). When the two variables of activation temperature and activation time were at their lowest point within the range tested, the highest yield was obtained. This finding was consistent with Ahmad *et al.* (2009) and Nasehir *et al.* (2010), who found that activation temperature had a significant impact/effect on the yield of activated carbon prepared from rattan sawdust and rice husk, respectively, although activation time had little impact/effect. With a rise in activation temperature, overall weight loss was observed, resulting in a decrease in yield at elevated activation temperatures. The carbon weight loss may be attributed to carbon burn-off and devolatilization of the precursor, which is due to increased pore production and formation as a result of the intensifying dehydration reaction (Yorgun and Yildiz,

2015; Varila *et al.*, 2017). The C-ZnCl<sub>2</sub> and C-CO<sub>2</sub> reaction rates increase as the temperature rises, resulting in a reduction in carbon yield (Lua and Yang, 2004).

#### 4.8.5 Effects of Activation Temperature and Impregnation Ratio (IR) on GSAC Percentage Carbon Yield in a Three-Dimensional (3-D) Plot

Figure 4.6 displays a 3-D plot of the effects of activation time and impregnation ratio (IR) on GS percentage carbon yield. The activation temperature has the highest F- value of 2413.99, while the impregnation ratio has the lowest F- value of 393.43.

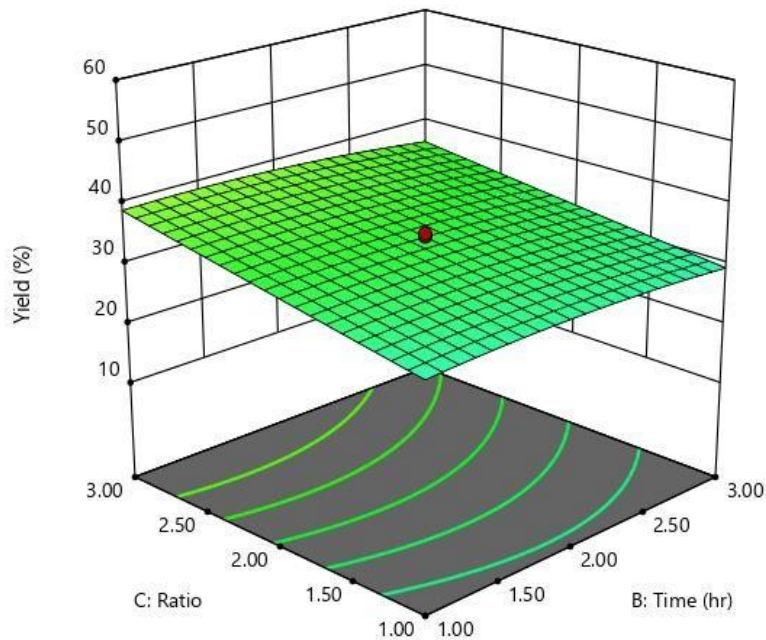


Figure 4.6: 3-Dimension response surface plot of GSAC yield (Effect of impregnation ratio and activation time)

Carbon yield increased as the impregnation ratio was increased. Within the range under examination, the highest yield was obtained at the maximum point of impregnation ratio. The existence of an activating agent encourages depolymerization, dehydration, and

redistribution of constituent biopolymers, as well as the conversion of aliphatic to aromatic compounds, resulting in increased yield (Yorgun and Yaldiz, 2015).

## **4.9 Surface Characterisations of Uncalcined and Calcined Samples of GS Activated Carbon**

### **4.9.1 Scanning Electron Microscope (SEM) analysis result**

The Scanning Electron Microscope (SEM) micrograph for uncalcined and calcined GSAC sample is presented in Figures 4.7 (a-e).

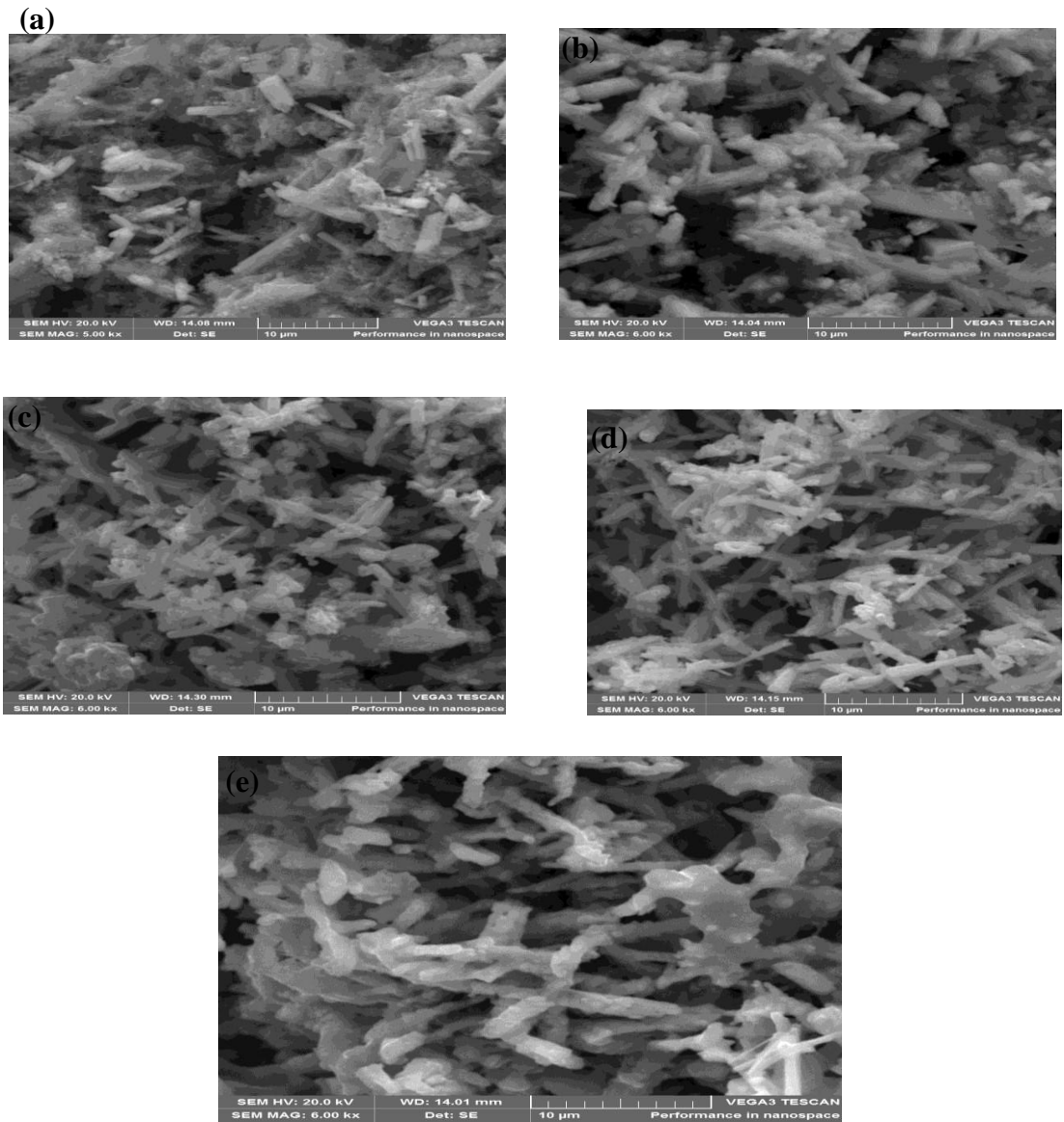


Figure 4.7: SEM micrographs of (a) UC (b) C71 (c) C72 (d) C81(e) C82 samples

Micrographs of SEM studies on the uncalcined and calcined samples in Figure 4.7 (a – e) show well-developed porous network which resulted due to chemical activation with  $\text{ZnCl}_2$  which is highly dehydrating in nature. The micrographs show that GSAC has rough texture with heterogeneous surfaces and a variety of randomly distributed pore size (Kamaraj and Umamaheswari, 2017). However, the pore sizes increased up to calcinations



calcination temperature resulted in formation of more phases (phase transformation) which could be as a result of the fact that at high temperature organic elements which were trapped decomposed and reacted with predominant silicon oxides ( $\text{SiO}_2$ ) to form new compounds. It was observed that uncalcined sample (UC), recorded a few major diffraction peaks  $30.06$  and  $35.78^\circ$ , showing that the peaks could be in the formative stage when compared with the sample calcined at  $800^\circ\text{C}$  for 2 hours which recorded numerous identified peaks at  $12.62, 22.03, 25.50, 26.54, 28.28, 31.46, 33.97, 35.17, 38.76, 48.92, 65.60$  and  $70.32$ .

#### 4.9.3 The Fourier transform infrared (FTIR) analysis result

Fourier transform infrared analysis was carried out on uncalcined (UC) and calcined (C71, C72, C81 and C82) GSAC samples and the result is presented in Figure 4.9

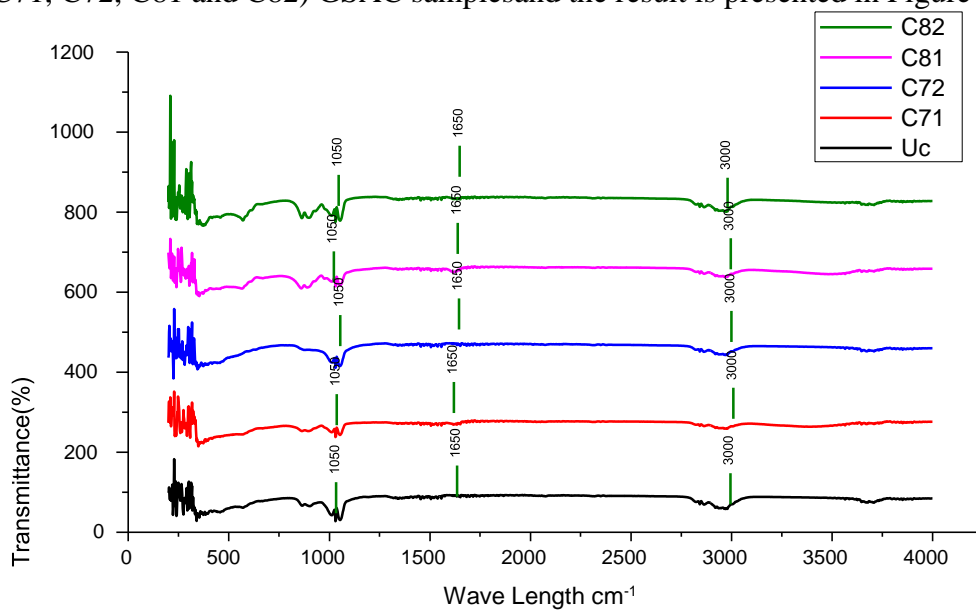


Figure 4.9: FTIR spectrum for uncalcined (UC) and calcined C71, C72, C81 and C82) samples

The FTIR spectra for samples UC, C71, C72, C81 and C82 recorded functional groups typical of any cellulose material. A stretching wave number range at about 3300 – 3400  $\text{cm}^{-1}$  point to the existenc of O- H functional group and a bending wave number range at about 2900 – 2800  $\text{cm}^{-1}$  reveals the existence of C– H functional group. However, as temperature increased from sample UC to C82, it was noticed that the organic maters began to burn off. It is well known that groundnut shell like other agricultural bio-wastes are largely composed of cellulose, hemicelluloses and lignin. The characteristic C- C stretching vibration is assigned to a spectra-wide significant peak at 1650, which is most likely ascribed to carbonyl groups that are strongly conjugated in the grapheme sheet. This is in line with carbon's fundamental existence. Also another consistent signicant peak at 1550 $\text{cm}^{-1}$  in the FTIR spectra is assigned to N = O vibration and ascribed to nitro (R –

$\text{NO}_2$ ) group. The presence of sulphur (S = O at peak 1050 $\text{cm}^{-1}$ ) and amino groups on the surface of GSAC can be attributed to its leguminous plant origin as evident in the presence of nitrogen and sulphur in elemental analysis.

#### **4.9.4 Thermogravimetric (TGA) analysis result**

Thermogravimetric (TGA) analysis was carried out on the uncalcined (UC) and calcined (C71, C72, C81 and C82) samples of GSAC and the result is presented in Figures 4.10 and 4.11.

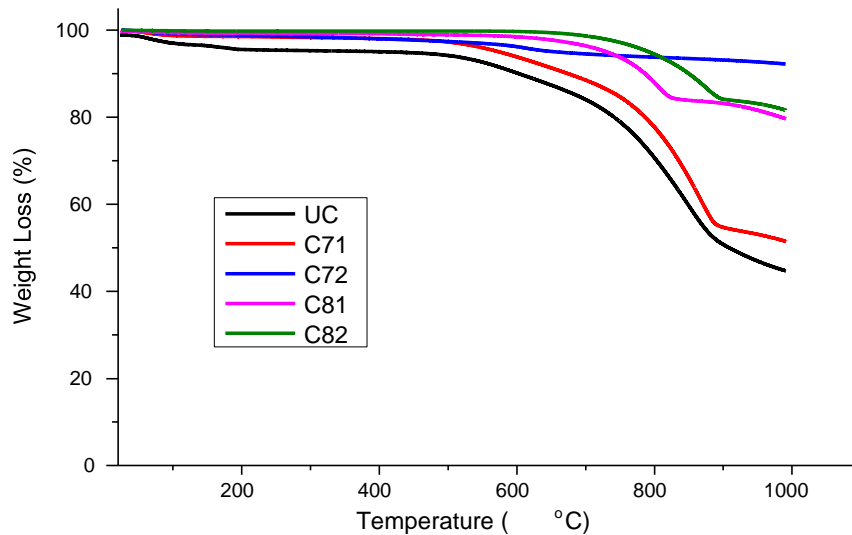


Figure 4.10: Thermogravimetric (thermal stability) plots for uncalcined (UC) and calcined (C71, C72, C81 and C82) samples of GSAC

From the thermogravimetric (thermal stability) plots shown in Figures 4.10, it was discovered that weight loss usually occurs in two phases (Thuan *et al.*, 2016). At temperatures around 500°C, the first stage of weight loss, which could be attributed to the loss of adsorbed water, occurred, and the second stage of weight loss, which could be due to more lignin and hemicellulose decomposing in the temperature range of 700 -

800°C. The plot also revealed that the degradation temperature for uncalcined sample (UC) stood at about 490°C while that of the most calcined sample (C82) was approximately 700°C. The result implied that the material exhibited good thermal stability which increased with increase in calcination temperature and time. The weight loss for uncalcined sample (UC) was approximately 55% while weight loss for the most calcined samples (C82) was approximately 15%. The percentage weight loss reduced with increase in calcination temperature.

The thermal decomposition plot of volatile matter for the uncalcined (UC) and calcined (C71, C72, C81 and C82) samples of GSAC is presented in Figure 4.11.

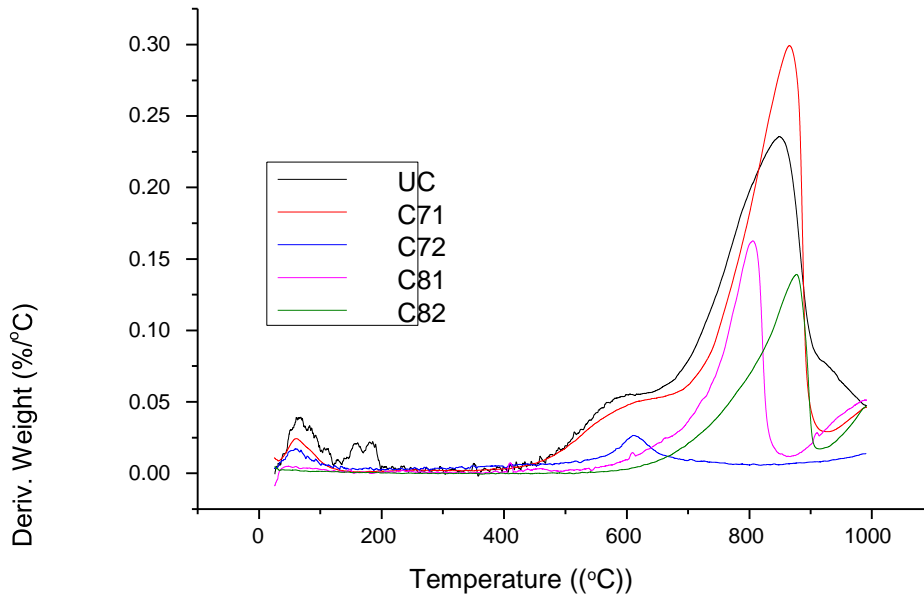


Figure 4.11: Derivative Thermogravimetric (DTG) graph of uncalcined (UC) and calcined (C71, C72, C81 and C82) samples of GSAC  
The derivative thermogravimetry (DTG) curves for all samples in Figure 4.11 shows initial peaks between 20 and 130°C, which corresponds with vaporization of water (Mamun *et al.*, 2015). The curves for all samples exhibited a single decomposition step with decomposition peak temperatures for UC, C71, C72, C81 and C82 samples at 820, 830, 610, 810, 820 and 900°C respectively. Result shows volatile matter increased with increase in calcinations temperature with sample C82 showing maximum thermal decomposition at temperature of about 900°C.

#### 4.9.5 Brunauer-Emmett-Teller (BET) Analysis

The BET surface area of uncalcined (UC) and calcined (C71, C72, C81 and C82) samples of GSAC is presented in Table 4.9.

Table 4.10: Brunauer-Emmett-Teller (BET) Analysis Result

Sample	Data
Sample	Surface Area
(m <sup>2</sup> /g)	
UC	498.52
C71	747.78
C72	751.05
C81	571.92
C82	418.67
Sample	Pore
	Volume(cm <sup>3</sup> /g)
UC	0.7
C71	0.88
C72	0.87
C81	0.89
C82	0.68
Sample	Pore Size (nm)
UC	24.3
C71	30.1
C72	28.6
C81	37.5
C82	19.0

The BET specific surface area of the samples increased with increase in temperature up to sample C72; after which increase in temperature resulted in decrease in specific surface area. Consequently, sample calcined at 700°C for 2 hours (C72) has the highest specific

surface area of  $751.05\text{m}^2/\text{g}$ . The results suggest that GSAC can be used as adsorbents and host matrix for metal nanoparticles (McDougall, 1991).

**4.10 Scanning Electron Microscope (SEM) Analysis of Metal Nanoparticles** Results of the Scanning Electron Microscope (SEM) analysis carried out for zinc, aluminum and titanium metal nanoparticles were obtained.

#### **4.10.1 Scanning electron microscope (SEM) analysis with energy dispersive x-ray spectroscope (EDS) for zinc metal nanoparticles**

The results of scanning electron microscope with energy dispersive X-ray spectroscope (SEM-EDS) analysis carried out on zinc metal nanoparticles are presented in Figure 4.12 (a and b) and Table 4.10.

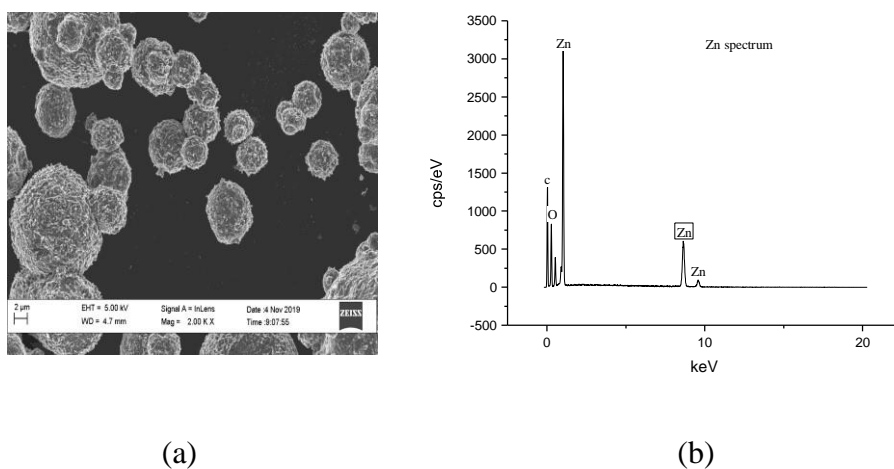


Figure 4.12: (a) SEM micrograph and (b) EDS spectrum of synthesized Zn metal nanoparticles  
The SEM image of prepared Zn nanoparticles shown in Figure 4.10 revealed the morphologies of pure, predominantly regularly shaped and smooth Zn nanoparticles

particles with fine nanograins sizes. The absence of dots and coloured patches on the image indicated the absence of impurities.

The SEM-EDS spectrum confirmed presence of Zn at peaks of about 1.01, 8.62 and 9.50 keV while the elemental composition table (Table 4.10) confirmed 63.98% and 36.02% presence of Zn and oxygen respectively.

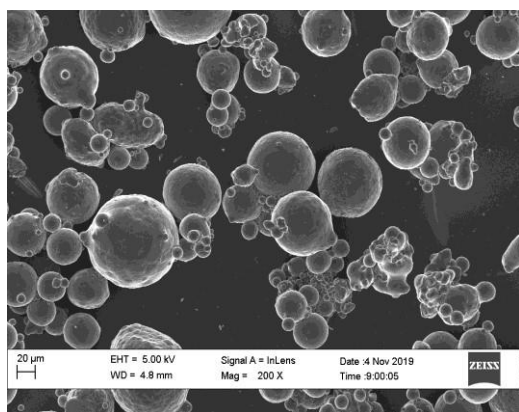
**Table 4.11: SEM-EDS elemental composition of Zn metal nanoparticles**

Element	wt. %
O	36.02
Zn	63.98
Total:	100

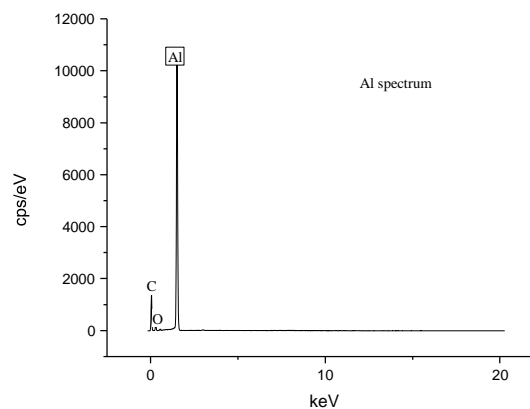
#### **4.10.2 Scanning electron microscope (SEM) analysis with energy dispersive x-ray spectroscope (EDS) for aluminum metal nanoparticles**

The results of scanning electron microscope with energy dispersive X-ray spectroscope (SEM-EDS) analysis carried out on aluminum metal nanoparticles are presented in Figure

4.13 (a and b) and Table 4.11



(a)



(b)

Figure 4.13: (a) SEM micrograph and (b) EDX spectrum for prepared Al metal nanoparticles

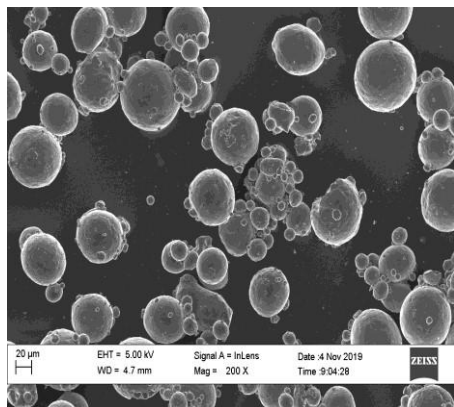
The SEM image of prepared Al metal nanoparticles shown in Figure 4.13 revealed the morphologies of pure, spherically shaped and smooth Al particles with fine nanograins sizes. The absence of dots and coloured patches on the image indicated the absence of impurities. The SEM-EDS elemental composition of Al metal nanoparticles is shown in Table 4.12

Table 4.12: SEM-EDS elemental composition of Al metal nanoparticles

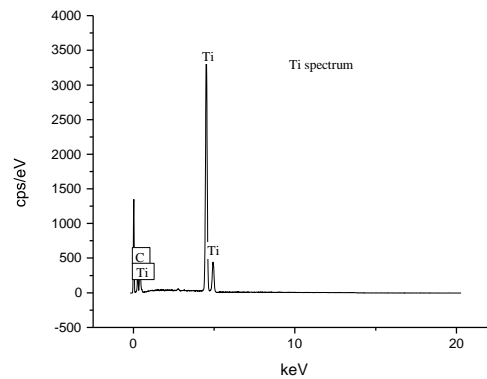
Element	wt. %
O	3.67
Al	96.33
Total:	100

The EDS spectrum confirmed the presence of Al at peak of about 1.48 keV while the elemental composition table (Table 4.12) confirmed 96.33% and 3.67% presence of Al and oxygen respectively.

#### 4.10.3 Scanning electron microscope (SEM) analysis with energy dispersive x-ray spectroscope (EDS) for titanium metal nanoparticles



(a)



(b)

Figure 4.14: (a) SEM micrograph and (b) EDS result of prepared Ti metal nanoparticles. The SEM image of prepared Ti shown in Figure 4.15 revealed the morphologies of pure, predominantly regularly shaped and smooth Ti particles with fine nanograins sizes. The absence of dots and coloured patches on the image indicated the absence of impurities. The EDS spectrum confirmed an interesting presence of Ti at peaks at about 0.02 keV, 4.52 keV and 4.57 keV.

Table 4.13: SEM-EDS elemental composition of Ti metal nanoparticles

Element	wt. %
Ti	100
Total:	100

From Table 4.13, it was noticed that the sample's elemental composition recorded a 100% Ti presence.

#### 4.11 Transmission Electron Microscope (TEM) Analysis of Metal Nanoparticles

Transmission Electron Microscope (TEM) analysis was carried out on prepared Zn, Al and Ti metal nanoparticles and results are presented in Figure 4.15 (a-c).

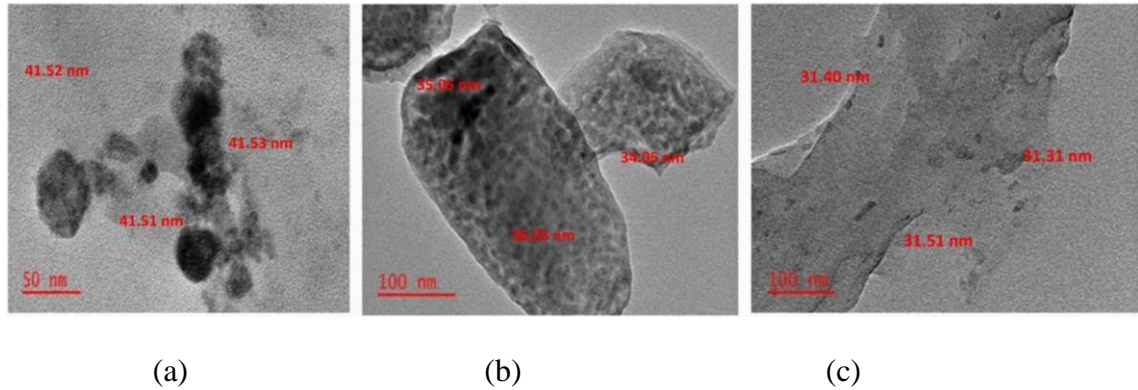


Figure 4.15: TEM micrographs of (a)Ti, (b)Zn and (c)Al metal nanoparticles

The TEM micrographs of the prepared metal nanoparticles as shown in Figure 4.15 (a-c) revealed internal fine and well distributed structures of Ti, Zn and Al metal nanoparticles, however, at some point the nanoparticles were agglomerated probably because of the high surface energy associated with metal nanoparticles which make them tend to be thermodynamically unstable. From the TEM analysis, the Ti, Zn and Al particles gave mean sizes,  $d_m$ , of 41.52 nm, 35.05 and 31.40 nm respectively.

#### 4.12 Determination of GSAC/ Metal Nanoparticles Composites from Crystallite Size Calculated Using Scherrer Formular

GSAC was first doped with Zn metal nanoparticles at three (3) different ratios of 3:1, 1:1 and 1::3, the XRD diffractions of each sample set obtained and used in calculating their

average crystallite size. The mixture ratio with the smallest average crystallite size/grain size was used as the base sample for the next mixture procedure.

#### 4.12.1 Determination of GSAC/Zn metal nanoparticles composites

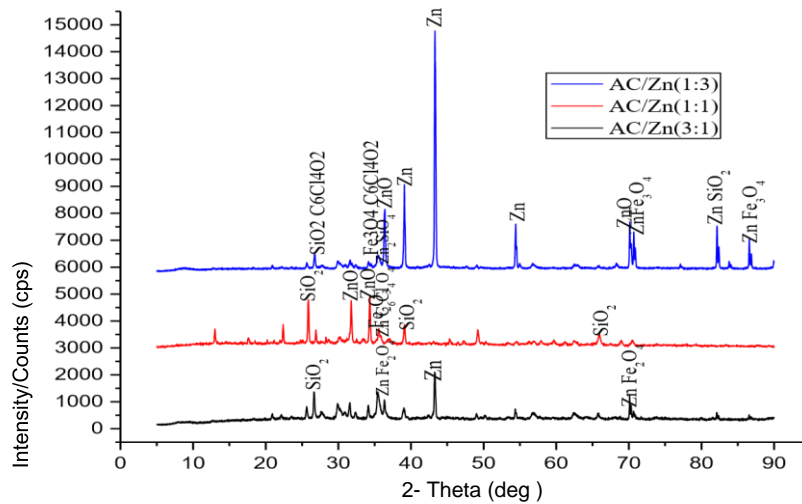


Figure 4.16: XRD pattern for GSAC/Zn composites at different mixture ratios

The XRD patterns shown in Figure 4.16 for the for GSAC/Zn mixture at different ratios of 3:1, 1:1 and 1:3 revealed sharp diffraction peaks for the three mixture ratios which suggested well crystallized samples. Strong, sharp and narrow diffraction peaks show that the synthesized product was well crystallized (Irfan *et al.*, 2018). Average crystallite size was calculated as presented in Table 4.14.

Table 4.14: Structural parameters of AC/Zn mixture at various mixture ratios

Sample ratio	Pos (2 $\theta$ )	Height (cts)	FWHM ( $\theta$ )	dspacing ( $\text{\AA}$ )	Rel. Int (%)	Crystallite size (G) (nm)
AC/Zn 3:1	26.694	815.265	0.157	3.340	55.690	54.30
	35.392	874.843	0.275	2.536	59.760	31.70
	43.238	146.998	0.157	2.092	100.000	56.89
	70.394	276.157	0.945	1.337	18.860	10.75
Average crystalline size (nm)						38.42
AC/Zn 1:1	13.005	481.749	0.205	6.807	30.110	40.77
	26.879	1522.424	0.128	3.444	95.120	66.70
	31.768	1514.599	0.153	2.817	94.660	56.43
	34.314	1600.122	0.180	2.613	100.000	48.28
	35.605	426.398	0.409	2.521	26.650	21.32
	39.105	653.321	0.205	2.303	40.830	42.98
	65.935	303359	0.409	1.417	18.960	24.20
	Average crystalline size (nm)					
AC/Zn 1:3	26.747	510.654	0.197	3.333	6.160	43.33
	35.489	387.223	0.394	2.529	4.670	22.13
	36.415	2116.334	0.177	2.467	25.510	49.39
	39.103	2756.964	0.197	2.304	33.230	44.73
	43.280	8296.267	0.098	2.090	100.000	91.16
	54.417	1625.057	0.118	1.686	19.590	79.13
	70.117	1660.344	0.098	1.342	20.010	103.87
	70.683	1322.823	0.098	1.333	15.940	103.80
82.144	1574.849	0.098	1.173	18.980	112.39	
86.584	1107.175	0.120	1.123	13.350	95.06	
Average crystal line size ( nm)						74.42

From the peak identity results for GSAC/Zn mixture presented in Table 4.13, it was observed that the mixture ratio of 3:1 recorded four (4) major diffraction peaks at 26.694, 35.392, 43.238 and 70.394° with Full Width at Half Maximum (FWHM) of 0.157, 0.275, 0.157 and 0.945 respectively. The GSAC/Zn mixture ratio of 1:1 recorded seven (7) major diffraction peaks at 13.005, 26.879, 31.768, 34.314, 35.605, 39.105 and 65.935° with Full Width at Half Maximum (FWHM) of 0.205, 0.128, 0.153, 0.180, 0.409, 0.205 and 0.409

respectively while the GSAC/Zn mixture ratio ten (10) major diffraction peaks were obtained at 26.747, 35.489, 36.415, 39.103, 43.280, 54.417, 70.117, 70.683, 82.144 and 86.584° with Full Width at Half Maximum (FWHM) of 0.197, 0.394, 0.177, 0.197, 0.098, 0.118, 0.098, 0.098, 0.098 and 0.120 respectively. The number of major peaks formed increased with decrease in the weight percentage of GSAC in the mixture. The crystallite size/grain size was determined from half maximum intensity using Scherrer equation stated in Equation 3.6. From the result presented in Table 4.19, it was observed that the GSAC/Zn mixture ratio of 3:1 gave the least average crystallite size of 38.42 nm. Therefore, the GSAC/Zn mixture ratio of 3:1 was selected for mixture with Al metal nanoparticles.

#### 4.12.2 Determination of GSAC-Zn/Al Metal Nanoparticles Composite

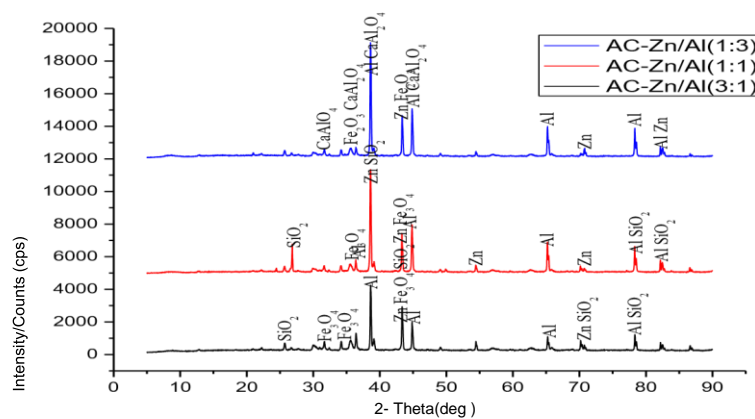


Figure 4.17: XRD pattern of GSAC-Zn/Al composites at different mixture ratios

The XRD patterns shown in Figure 4.17 for the for GSAC-Zn/Al mixture at different ratios of 3:1, 1:1 and 1:3 revealed sharp diffraction peaks for the three mixture ratios which

suggested well crystallized samples. This is in agreement with Irfan *et al.* (2018) which stated that strong, sharp and narrow diffraction peaks show that the synthesized product was well crystallized.

**Table 4.15: Structural parameters of AC-Zn/Al mixture at various mixture ratios**

Sample ratio	Pos (2 $\theta$ )	Height (cts)	FWHM ( $\theta$ )	dspacing (Å)	Rel. Int (%)	Crystallite size (G) (nm)
AC-Zn/Al 3:1	25.719	399.995	0.315	3.464	10.470	27.04
	30.125	228.947	0.630	2.967	6.000	13.65
	35.579	513.701	0.394	2.523	13.450	22.13
	36.493	963.437	0.157	2.466	25.230	55.69
	38.591	3818.649	0.118	2.333	100.000	74.56
	39.134	644.032	0.197	2.302	16.870	44.73
	43.338	2571.927	0.118	2.088	67.350	75.72
	44.833	1646.232	0.118	2.022	43.110	76.12
	65.239	832.876	0.118	1.430	21.810	83.55
	70.482	230.997	0.944	1.336	6.050	10.77
78.347	948.433	0.118	1.220	24.840	90.77	
Average cryst alline size ( nm)						52.25
AC-Zn/Al 1:1	26.836	1604.326	0.118	3.322	27.820	72.35
	35.527	386.221	0.394	2.527	6.700	22.13
	38.645	5767.809	0.148	2.330	100.000	59.46
	43.311	2303.732	0.098	2.089	39.940	91.17
	44.782	2322.220	0.157	2.024	40.260	57.20
	54.428	388.449	0.236	1.686	6.730	39.56
	65.193	1825.821	0.098	1.431	31.660	100.57
	70.258	211.434	0.787	1.340	3.670	12.13
	78.312	1538.786	0.098	1.221	26.680	109.27
	82.369	370.072	0.472	1.171	6.420	23.38
Average cryst alline size ( nm)						58.72
AC-Zn/Al 1:3	155.694	0.630	2.966	2.370	13.65	
	394.889	0.394	2.523	6.010	22.13	
	6575.789	0.098	2.334	100.000	89.77	
	2339.327	0.118	2.088	35.570	75.72	
	2661.635	0.117	2.022	40.480	76.77	
	1727.888	0.118	1.431	26.280	83.53	
	310.327	0.630	1.330	4.720	16.17	
	1664.475	0.118	1.221	25.310	90.76	
338.733	0.630	1.170	5.150	17.52		

From the peak identity results for GSAC/Zn mixture presented in Table 4.15 it was observed that the mixture ratio of 3:1 recorded eleven (11) major diffraction peaks at 25.719, 30.125, 35.579, 36.493, 38.591, 39.134, 43.338, 44.833, 65.239, 70.482 and 78.347° with Full Width at Half Maximum (FWHM) of 0.315, 0.630, 0.394, 0.157, 0.118, 0.197, 0.118, 0.118, 0.118, 0.944 and 0.118 respectively. The GSAC-Zn/Al mixture ratio of 1:1 recorded ten (10) major diffraction peaks at 26.836, 35.527, 38.645, 43.311°, 44.782, 54.428, 65.193, 70.258, 78.312 and 82.369° with Full Width at Half Maximum (FWHM) of 0.118, 0.394, 0.148, 0.098, 0.157, 0.236, 0.098, 0.787, 0.098 and 0.472 respectively while the GSAC-Zn/Al mixture ratio of 1:3 produced nine (9) major diffraction peaks at 30.129, 35.584, 38.581, 43.343, 44.826, 65.191, 70.831, 78.327 and 82.438° with Full Width at Half Maximum (FWHM) of 0.630, 0.394, 0.098, 0.118, 0.117, 0.118, 0.630, 0.118 and 0.630 respectively. The number of major peaks formed decreased with increase in the weight percentage of Al in the mixture. The crystallite size/grain size was determined from half maximum intensity using Scherrer equation stated in Equation 3.6. From the result presented in Table 4.20, it was observed that the GSAC-Zn/Al mixture ratio of 3:1 gave the least average crystallite size of 52.25 nm. Therefore, the GSACZn/Al mixture ratio of 3:1 was selected for mixture with Ti metal nanoparticles.

#### **4.12.3 Determination of GSAC-Zn-Al/Ti metal nanoparticles composite**

The XRD result for GSAC-Zn-Al/Ti mixture at ratios 1:3, 1:1 and 3:1 is presented in Figure 4.18.

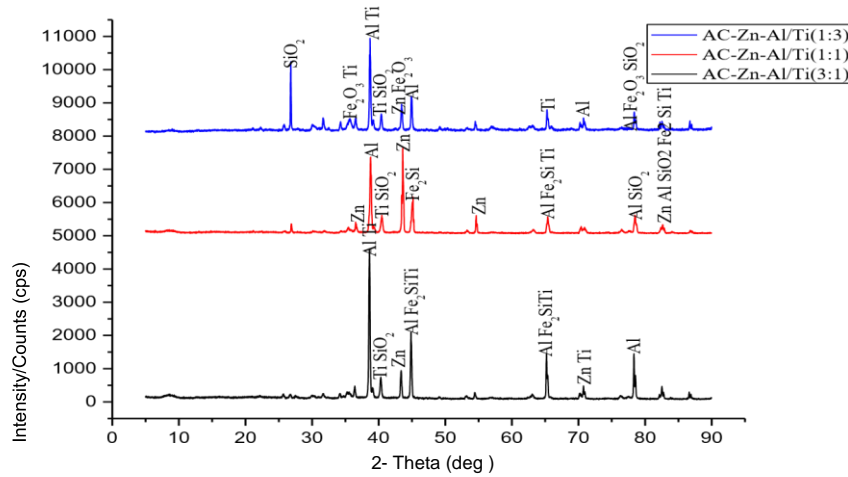


Figure 4.18: XRD patterns of GSAC-Zn-Al/Ti composites at different mixture ratios. The XRD patterns shown in Figure 4.18 for the for GSAC/Zn mixture at different ratios of 3:1, 1:1 and 1:3 revealed sharp diffraction peaks for the three mixture ratios which suggested well crystallized samples. This is in agreement with Irfan *et al.* (2018) which stated that strong, sharp and narrow diffraction peaks show that the synthesized product was well crystallized.

**Table 4.16: Structural parameters of AC-Zn-Al/Ti mixture at various mixture ratios**

Sample ratio	Pos (2 $\theta$ )	Height (cts)	FWHM ( $\theta$ )	d-spacing ( $\text{\AA}$ )	Rel. Int (%)	Crystallite size (G) (nm)
AC-Zn-Al/Ti 3:1		4477.604	0.216	2.332	100.000	40.73
		596.909	0.236	2.236	13.330	37.48
		770.206	0.197	2.087	17.200	45.36
		1946.765	0.118	2.022	43.480	76.12
		1250.461	0.098	1.431	27.930	100.57
		241.699	0.630	1.330	5.400	16.17
		1327.116	0.118	1.220	29.64	90.76
	Average crystal line size (nm)					51.69
AC-Zn-Al/Ti 1:1	30.598	226.059	0.315	2.455	10.120	27.33
	38.780	2232.868	0.138	2.322	100.000	63.79
	40.490	445.131	0.315	2.228	19.940	28.10
	43.639	2205.559	0.197	2.074	98.780	45.41
	45.112	843.862	0.275	2.010	37.790	32.70
	54.615	444.229	0.197	1.680	19.890	47.44
	65.398	469.710	0.315	1.427	21.040	31.33
	70.442	135.720	0.945	1.337	6.080	10.76
	78.494	491.518	0.236	1.218	22.010	45.43
	82.662	216.120	0.551	1.167	9.680	20.07
	Average crystal line size (nm)					35.24
AC-Zn-Al/Ti 1:3	26.783	1874.637	0.118	3.329	70.100	72.34
	35.663	283.688	0.630	2.517	10.610	13.85
	38.720	2674.294	0.138	2.325	100.000	63.78
	40.384	463.395	0.236	2.233	17.330	37.49
	43.453	737.108	0.197	2.083	27.560	45.37
	44.918	963.016	0.197	2.018	36.010	45.61
	63.044	109.687	0.945	1.474	4.100	10.31
	65.323	475.760	0.315	1.428	17.790	31.31
70.880	230.288	0.945	1.329	8.610	10.79	
78.421	400.014	0.315	1.219	14.960	34.02	
	Average crystal line size (nm)					36.49

From the peak identity results for GSAC-Zn-Al/Ti mixture presented in Table 4.16 it was observed that the mixture ratio of 3:1 recorded seven (7) major diffraction peaks at

38.611°, 40.309°, 43.351°, 44.831°, 65.183°, 70.830° and 78.327° with Full Width at Half

Maximum (FWHM) of 0.216, 0.236, 0.197, 0.118, 0.098, 0.630 and 0.118 respectively.

The GSAC-Zn-Al/Ti mixture ratio of 1:1 recorded ten (10) major diffraction peaks at 30.598°, 38.780°, 40.490°, 43.639°, 45.112°, 54.615°, 65.398°, 70.442°, 78.494° and 82.662° with Full Width at Half Maximum (FWHM) of 0.315, 0.138, 0.315, 0.197, 0.275, 0.197, 0.315, 0.945, 0.236 and 0.551 respectively. Also the GSAC-Zn-Al/Ti mixture ratio ten (10) major diffraction peaks were obtained at 26.783, 35.663, 38.720, 40.384, 43.453, 44.918, 63.044, 65.323, 70.880 and 78.421° with Full Width at Half Maximum (FWHM) of 0.118, 0.630, 0.138, 0.236, 0.197, 0.197, 0.945, 0.315, 0.945 and 0.315 respectively. The number of major peaks formed increased with increase in the weight percentage of Ti metal nanoparticles in the mixture from ratio 3:1 to 1:1 but remained the same from ratio 1:1 to 1:3. The crystallite size/grain size was determined from half maximum intensity using Scherrer equation stated in Equation 3.6. From the result presented in Table 4.21, it was observed that the GSAC-Zn-Al/Ti mixture ratio of 1:1 gave the least average crystallite size of 35.24 nm. Therefore, the GSAC-Zn-Al/Ti mixture ratio of 1:1 was selected for coating of mild steel substrates.

### 4.13 Preparation of Mild Steel Samples

The photograph of prepared mild steel samples is shown in Plate II



Plate II: Photograph of mild steel samples

The prepared mild steel samples as can be observed in Plate II became mirror like surfaces after they were brushed, polished with emery paper and activated in hydrochloric acid.

### 4.14 Characterisation of Raw Steel Sample

#### 4.14.1 X-ray fluorescence (XRF) analysis

The raw steel sample was analysed using x-ray fluorescence spectrometer to determine elemental composition of the sample and the result presented in Table 4.17.

Table 4.17: Percentage elemental composition of raw mild steel sample

Element	Fe	Ca	C	Mn	Mo	Si	Al	Cr	Ti
Weight (%)	97.28	0.8	0.15	0.46	0.22	0.12	0.2	0.04	0.73

Low carbon steel (mild steel) is a classification of steel when it has a carbon content of

less than 0.25. As a result of the information in table 4.16, it can be deduced that the sample used in this analysis is mild steel, as the carbon content is 0.15 % (Abdulrahman *et al.*, 2017). Beside C, Si, Al, Cr, Ca, Mn, Mo, Ca and Ti were present in different percentage compositions as shown in Table 4.17.

**4.14.2 X-ray Diffraction (XRD) analysis of heated and unheated steel sample** The X-ray diffraction (XRD) analysis of both heated and unheated mild steel samples was carried out and their results shown in Figure 4.20

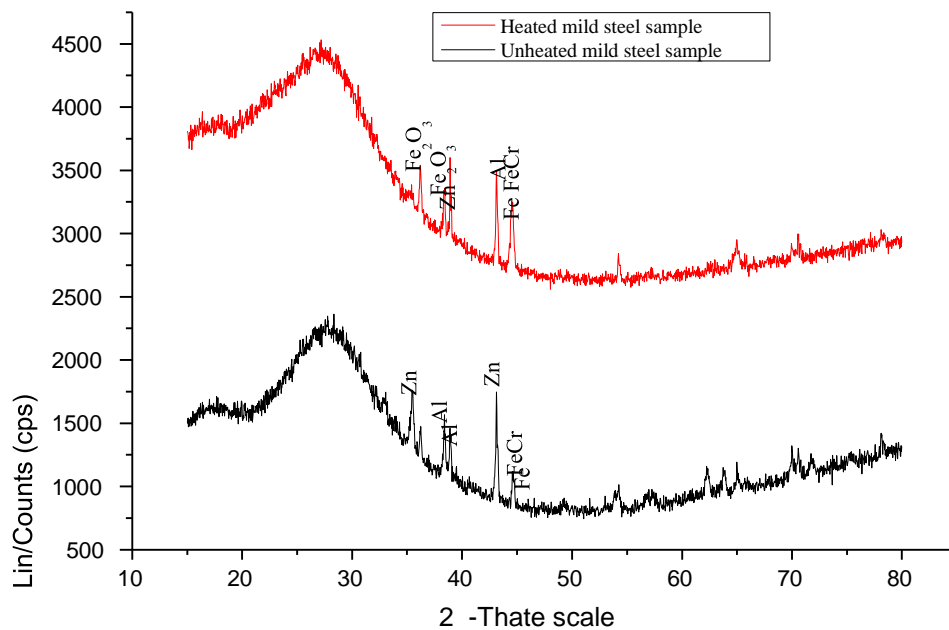


Figure 4.20: XRD pattern of heated and unheated mild steel samples

The XRD patterns of the two samples (heated and unheated steel samples) were seen to be somewhat similar. However, the XRD patterns for heated sample revealed the formation of five (5) major peaks with phases formed at those peaks as FeCr, Fe, Zn, Al and Fe<sub>2</sub>O<sub>3</sub>, while the XRD pattern for the unheated sample recorded four (4) major peaks

with phases formed at those peaks as FeCr, Fe Zn and Al. The formation of a secondary hematite ( $\text{Fe}_2\text{O}_3$ ) crystal phase could be attributed to the oxidation of steel at high temperature. The result is similar to that shown by Marcus *et al.* (2012) who observed  $\text{Fe}_2\text{O}_3$  as a dominant phase during oxidation of steel at 500 and 600°C.

#### 4.14.3 Scanning electron microscope (SEM) with energy dispersive x-ray spectroscopy (EDS) analysis of mild steel sample

Scanning electron microscope (SEM) with Energy Dispersive X-ray spectroscopy (EDS) analysis of the raw mild steel sample was carried out and the result is presented in Figure

4.21.

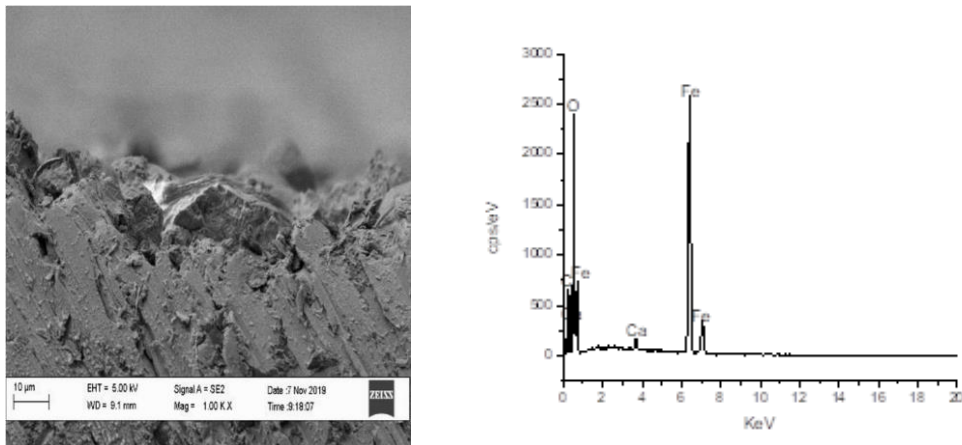


Figure 4.21:(a) SEM cross-sectional image and (b) and EDS spectrum of raw steel sample

The result of surface morphology of the mild steel sample shown in Figure 4.21 revealed rough surfaces with irregularly shaped cavities that could trap some molecules of the corrosive medium and become potential sites for propagation of corrosion. Parallel

features which are associated with polishing scratches were observed on the clean polished steel surface (Noor and Al-Mubarak, 2008).

The energy dispersion spectrum (EDS analysis) was utilized to determine the elemental composition of the mild steel which showed the presence of Fe, O, C and Ca. The percentage weight composition of the mild steel is as presented in Table 4.18.

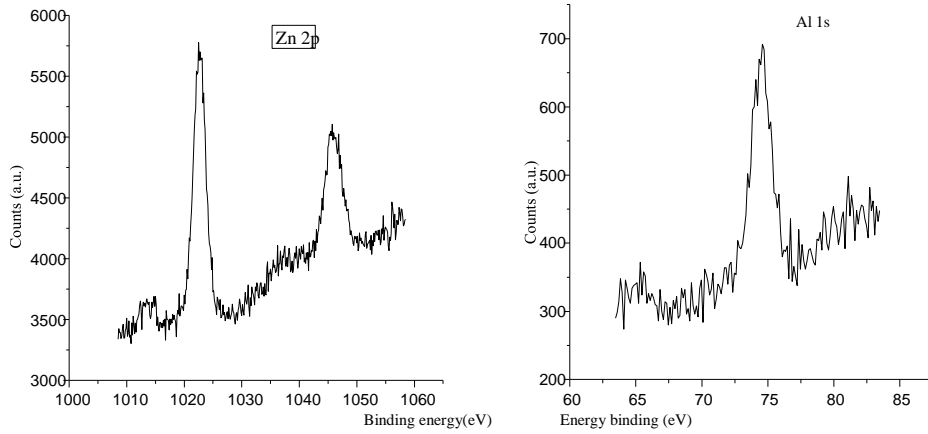
**Table 4.18: SEM-EDS elemental composition** for raw mild steel

Element	Wt. %	Wt.%	Sigma
C	18.91	0.47	
O	24.18	0.32	
Ca	0.76	0.06	
Fe	56.14	0.43	
Total	100		

The quantitative result of the mild steel SEM-EDS shown in Table 4.18 revealed a high weight percentage for Fe (56.14 wt. %). This is an indication that the mild steel is highly susceptible to corrosion when in contact with corrosive environment such as hydrochloric acid.

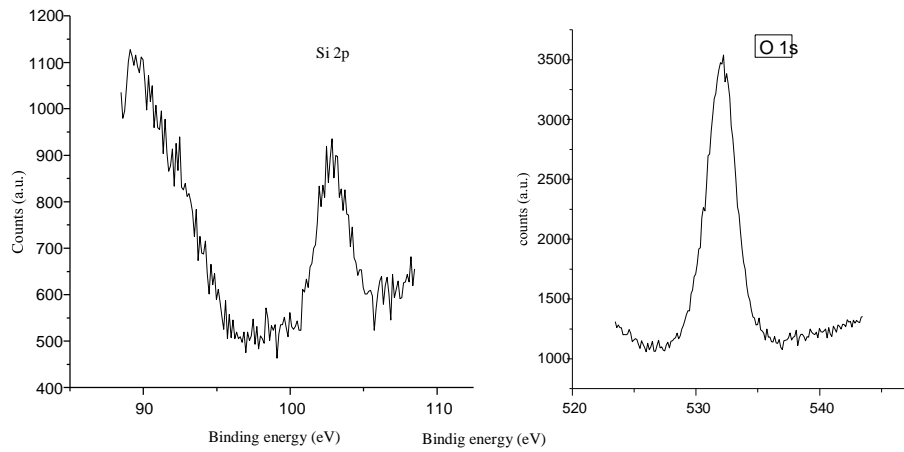
#### 4.15 X-ray Photoelectron Spectroscopy (XPS) Analysis of Prepared GSAC-Zn-Al/Ti Composites

The X-ray photoelectron spectroscopy (XPS) spectra for Zn-Al-Ti metal nanocomposites supported groundnut shell activated carbon is presented in Figure 4.22.



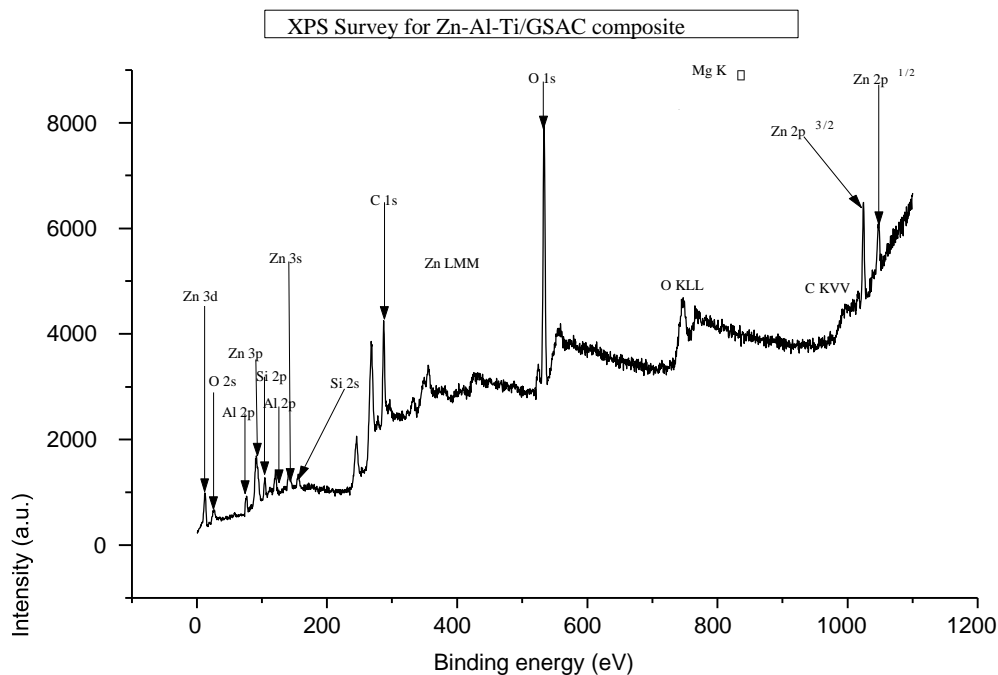
(a)

(b)



(c)

(d)



(e)

Figure 4.22: XPS spectra for (a) Zn 2p (b) Al 2p (c) Si 2p (d) O 1s and (e)GSAC-ZnAl/Ti composites

Figure 4.22 (a) shows the spectrum obtained for Zn in the metal nanoparticles supported organic activated carbon, with the Zn 2p peak at 1020.8 eV, corresponding to Zn (II) in the ZnO structure (Arandi *et al.*, 2019). A strong resolution of Zn 2p spectrum with two strong peaks at 1021.83 eV and 1023.15 eV corresponding to Zn 2p<sup>3/2</sup> and Zn 2p<sup>1/2</sup> respectively was observed, representing the presence of Zn<sup>2+</sup> and in the ZnO wurtzite structure (Kim and Kim, 2015). Figure 4.22 (b) represents the Al 2p spectrum of an aluminum surface while Si 2p binding energy of approximately 102 eV shown in Figure 4.22 (c) is typical of organic Si. The O 1s spectrum at 530 eV observed in Figure 4.22 (d) could be attributed to adsorbed molecular oxygen from the atmosphere on the oxide films

(Lee *et al.*, 2015). The high intensity observed for the O 1s clearly shows that there is a significant amount of adsorbed oxygen ions on the surface of the film under study.

The general survey spectrum in Figure 4.22 (e) gives information about the elements present in the GSAC/Zn-Al-Ti film and their chemical bonds in each phase of the growth process. The GSAC-Zn-Al-Ti spectrum confirmed the presence of Al 2p and Zn 3p which relates to the participating species of Al and Zn in organic support. However, Ti could not be detected, probably because of low concentration. Similar observation was made in the SEM EDS result for Zn-Al-Ti nanocomposites supported GSAC where Ti was not detected. XPS and SEM are complimentary techniques for investigating the chemical composition and morphology of nanomaterials (Stromeier *et al.*, 2009). The participation of GSAC support in the system was verified by the detection of Si 2p and C 1s signals as part of the surface compositions. It was observed that O 1s has the highest peak and therefore, has the highest atomic composition. This is not surprising since XPS is a surface technique which probes only a few nanometers of a sample. Therefore, intense peak for oxygen may be as a result of exposure of the sample to ambient atmosphere before analysis.

The intensive O 1s signal at 530.5 eV, Zn 2p<sup>3/2</sup> and Zn 2p<sup>1/2</sup> with binding energy of 1021.83 and 1044 eV respectively correspond to XPS core levels of matrix elements of ZnO wurtzite structure (Ievtushenko *et al.* 2013). A weak line is observed positioned at 72.6 eV corresponds to the 2p state of Al in the Zn-Al-Ti/GSAC film. Absence of peak at 74.3 eV in the general survey spectrum is related to 2p state of Al in Al<sub>2</sub>O<sub>3</sub> was observed.

This tends to confirm that Al substituted Zn in the cation sublattice of ZnO when the Zn-Al-Ti/GSAC film was formed. It was observed that Zn species formed two new types of Zn bonds at Zn 2p<sup>3/2</sup> first with binding energy of 1021.83 eV and the second at 1023.15 eV. Similarly, a shift in Al 2p binding energy from 75.9 to 112.5 eV was observed. This result suggests that the introduction of metal nanoparticles into GSAC may have led to rearrangement of the particles surface, leading to reappearance of Zn 2p<sup>3/2</sup> signal at 1023.15 eV of the ZnO. This second Zn 2p<sup>3/2</sup> signal at 1023.15 eV may have resulted from the electrostatic interaction between the zinc oxide group (of the metal composite) and the stabilizing carbon micropores.

Taking into consideration all the observed changes on the general survey spectra captured by the XPS equipment and the possible chemical compounds obtained from NIST database, the possible formation of Al<sub>2</sub>ZnSi<sub>2</sub> composite film was responsible for the enhanced anti-corrosion performance of the coated mild steel surface.

The presence of peaks with a double entry as shown in Table 4.18 indicates more than one chemical state condition. The possible chemical compounds obtained from NIST database on the internet as well as the Handbook of Photoelectron Spectroscopy by Perkin Elmer corp. 1992 have also been listed in Table 4.19.

Table 4.19: Results of XPS possible chemical compounds for GSAC-Zn-Al/Ti

Specimen C	Correct	Comment
Peak	BE(eV)	BE (eV)
C 1s	286.33	284.8
Correct	1.53	C-C

Al 2p	75.97	74.44	Al <sub>2</sub> O <sub>3</sub>
Zn 2p <sub>3/2</sub> (1)	1023.36	1021.83	ZnO
Zn 2p <sub>3/2</sub> (2)	1024.68	1023.15	Zn(OH) <sub>2</sub>
Si 2p	104.38	102.85	Silicate/SiO <sub>2</sub>

#### 4.16 Heat Treatment of Mild Steel Samples

Raw steel samples (4) were subjected to heat treatment (stress releasing annealing) procedure and the effect of heat treatment on the hardness of mild steel sample was investigated and result presented on the bar chart in Figure 4.26.

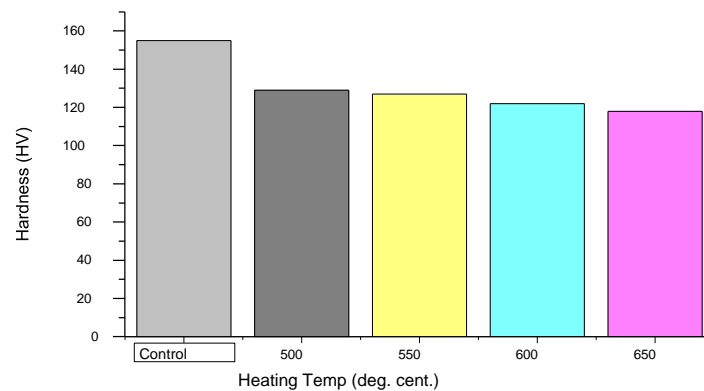


Figure 4.23: Bar chart showing effect of annealing on the hardness values of mild steel sample

As shown in Figure 4.23, the hardness value of the annealed mild steel sample decreased with increase in annealing temperature from 500 to 650°C. This could be attributed to the migration of atoms in the crystal lattice during heating operation. The migration of atoms in the crystal lattice may have resulted in reduction in number of dislocations in the crystal structure of mild steel, thereby reducing the hardness property of the steel. Heat treatment of metals with defects leads to recovery by migration of interstitial atoms and rearrangement and annihilation of dislocations which played vital roles in hardening

process of materials (Boczkal and Perek-Nowak, 2014).The control sample (mild steel sample which was not annealed) provided a hardness value of 155 HV, while during annealing, hardness value decreased from 129HV at 500°C to 118HV at 650°C.

**4.17 Scanning Electron Microscope (SEM) with Energy Dispersive X-ray Spectroscopy (EDS) Analysis of the Cross Section of Coated Steel Sample** The SEM image showing the cross-sectional view of GSAC-Zn-Al/Ti coated steel sample with EDS result is presented in Figure 4.27

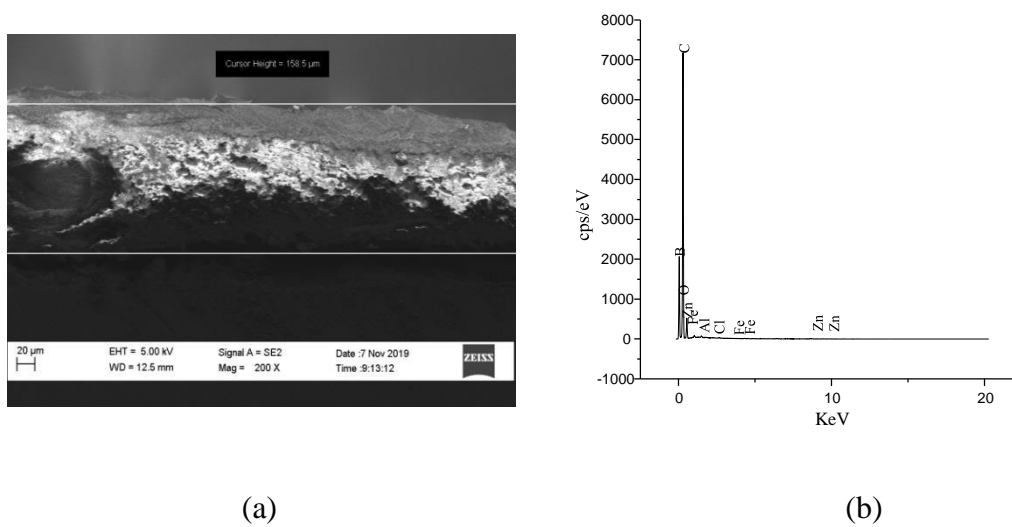


Figure 4.24:(a) SEM cross-sectional image and (b)EDS spectrum for Zn-Al-Ti-GSAC/Epoxy coated steel sample

Good interface reinforcement is observed in the SEM image of Zn-Al-Ti nanoparticles supported GSAC coated mild steel shown in figure 4.24. This could be attributed to interaction between the reinforcing metal nanoparticles and epoxy. The result is similar to the position of Burns (2007) which suggested that formation of finer scale lamellar microstructure corresponds to improved mechanical properties which could prevent cracking in the coating. Also shown in the SEM image is the well-defined coating layer

with a measured coating thickness of 158.5 $\mu$ m. Increase in coating thickness resulted in reduction of material hardness with 100  $\mu$ m coating thickness ensuring the highest hardness values for Cr<sub>2</sub>O<sub>3</sub> and Al<sub>2</sub>O<sub>3</sub> coatings (Kucukrendeci and Yetgin, 2013).

The SEM-EDS for GSAC-Zn-Al/Ti coated steel sample showing the percentage weight of participating elements in the coating system has been presented in Table 4.19.

Table 4.20: SEM-EDS for Zn-Al-Ti-GSAC/Epoxy coated steel sample

Element	wt.%	wt.% Sigma
B	21.56	7.96
C	74.24	7.53
O	4	0.42
Al	0.04	0.01
Cl	0.02	0.01
Fe	0.04	0.01
Zn	0.1	0.02
Total:	100	

SEM-EDS result for Zn-Al-Ti-GSAC/Epoxy coated steel sample revealed the coatings were mainly composed of B, C, O, Al, Cl, Fe, and Zn. The result is indicative of the successful incorporation of all the starting elements in the coating processes. The presence of B and Cl could be traced to the boron-containing epoxy – novalac resins, and the activating agent (ZnCl<sub>2</sub>) used in the chemical activation process. However, the presence of Ti could not be detected. This could be because Ti was below the detection range of the SEM equipment. Similar situation was reported in the XPS result.

#### 4.18 Determination of the Effect of GSAC-Zn-Al/Ti Weight Fraction in Epoxy on the Microhardness Value of Coated Mild Steel Samples

The result of microhardness test carried out on the uncoated mild steel sample and the coated samples with 1:1, 2:1, 3:1 and 4:1 weight fractions of GSAC-Zn-Al/Ti in epoxy matrix was investigated and result presented in Figure 4.25.

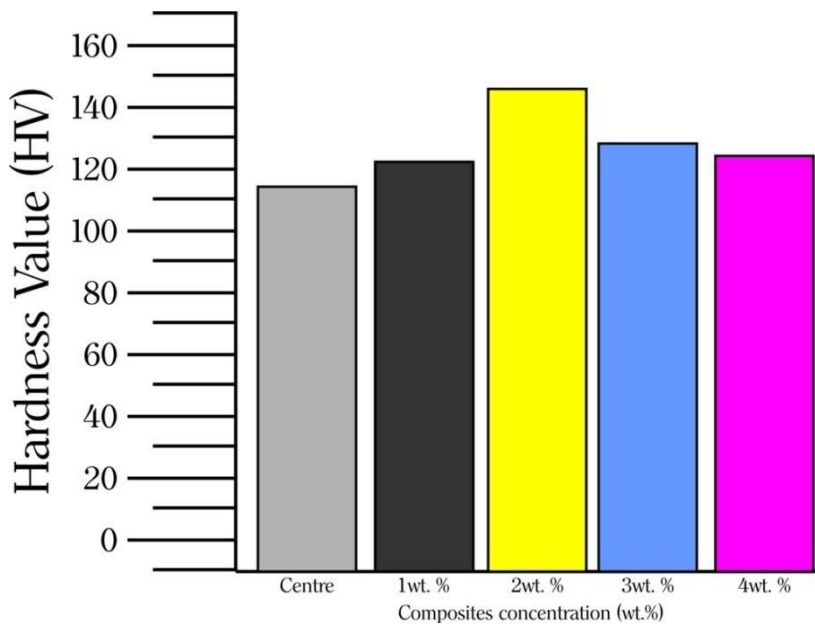


Figure 4.25: Bar chart showing effect of ratio of weight fraction on hardness values of coated mild steel samples

It was noted from Figure 4.25 that the control sample which is neat epoxy coating recorded the lowest micro hardness value of 115 HV while the microhardness values for the coated samples was seen to increase with increase in weight fraction of GSAC-ZnAl/Ti in the system up to 2:1 wt.% with the highest microhardness value of 157 HV as shown in Figure 4.25. The improvement in the microhardness values could be attributed to the formation of adhesive mechanism of the composite coating on the substrate sample, the strain energy

imposed by the particles in the matrix on the periphery of the composite coated steel and other processing parameters (Akande *et al.*, 2019). Particles addition in the matrix alloy increases the strain energy in the periphery of the particles in the matrix and these tendencies may be as a result of formation of the dislocation at the boundary of the reinforcing particles by the difference in the thermo-expansion coefficient between the matrix and the reinforcing particles (Popoola *et al.*, 2016). However, after 2:1 wt.% ratio, it was observed that the hardness value of the coated steel surface began to reduce which could be attributed to the fact that the composite may have exceeded its saturation point with further loading of alloys into epoxy resin.

#### 4.19 Determination of the Effect of GSAC-Zn-Al/Ti Weight Fraction in Epoxy on Porosity of Coated Mild Steel Sample

The result of porosity test carried out on the uncoated mild steel sample and the coated samples with 1:1, 2:1, 3:1 and 4:1 weight fractions of GSAC-Zn-Al/Ti in epoxy matrix was investigated and result presented in Figure 4.29.

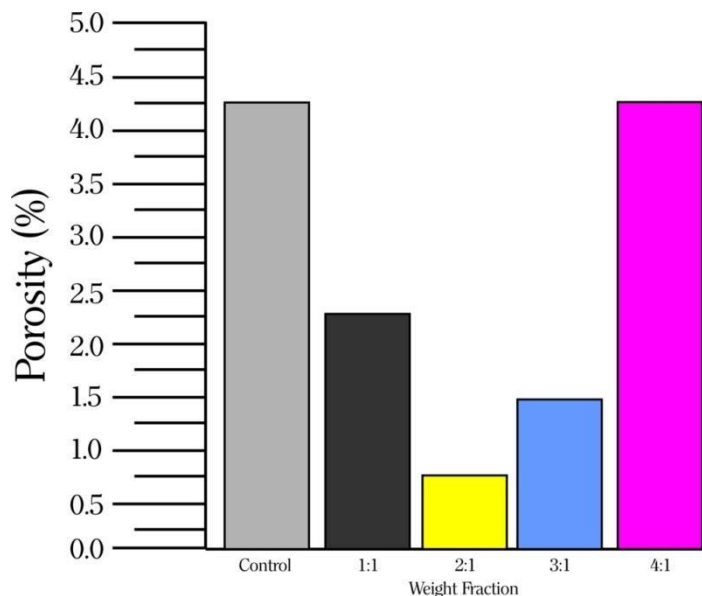


Figure 4.26: Bar chart showing effects of weight fraction on the porosity of coated mild steel sample

The data shown in Figure 4.26 revealed that the control sample which is a neat epoxy coated steel recorded high percentage volume of porosity. This could be related to the existence of pores in epoxy coatings, either at the coating /metal interface or in the form of pathways through the coating which accelerates the rate of delamination of the coatings (Kosek *et al.*, 1995). However, there was decrease in percentage volume of porosity with increase in weight fraction of GSAC-Zn-Al/Ti in the epoxy matrix till ratio 2:1, after which there was increase in percentage volume of porosity with additional loading of the composite, showing an inverse relationship with microhardness results (Saravanan *et al.*, 2001). This behaviour which may have resulted from increased competition among the increasing reinforcement particles as they travel to settle on the surface of mild steel substrate. There is therefore, decrease in the kinetic energy of the particles which may create inter-atomic spaces. The particles may compress each other and create air traps within the structure while the epoxy resin may no longer be able to completely fill all the voids formed between the reinforcement particles at higher weight fraction due to insufficient amount of epoxy or low viscosity resulting in poor flowability at higher filler content. The density and porosity of epoxy resin composite is a function of filler content and porosity is seen to increase with increase in filler content which may partially be due to the fact that the epoxy resin are completely not in close contact at the interface, thus causing higher porosity at higher filler content (Chung and Lin, 2016).

## 4.20 Electrochemical Impedance Spectroscopy (EIS) Result

The Nyquist plots for bare metal with neat epoxy coated steel and coated steel samples in 1 M HCl solution are shown in Figure 4.30 (a and b).

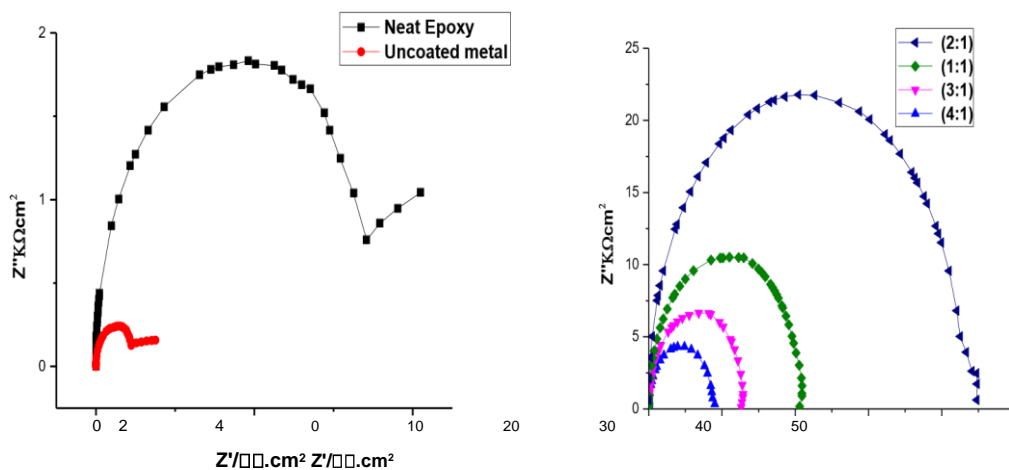


Figure 4.27: Nyquist plots for (a) bare metal and neat epoxy coating and (b) coated steel samples in 1 M HCl solution at 293K

Figure 4.27 (a) shows a Nyquist plot of uncoated and neat epoxy coated mild steel coupons with incomplete semicircles in the high frequency region and approximate straight lines in the low frequency range. The charge transfer resistance ( $R_{ct}$ ) and the double layer capacitance ( $C_{dl}$ ) are also connected to the high frequency area semicircle in general. The low frequency impedance is the Warburg impedance ( $W$ ), which means the diffusion of dissolved oxygen or soluble iron chloride complexes during the corrosion process. The semicircle suggested electron transport at the thin electrode/electrolyte interface, and the straight line indicated grain boundary.

The Nyquist plot of Zn-Al-Ti nanocomposites supported GSAC epoxy coatings in Figure 4.27 (b) showed semi-circle like curves with the disappearance of the Warburg impedance in the low frequency region. This implies that the loading of the alloy into epoxy prevented the diffusion of dissolved oxygen, iron chloride and iron oxide complexes. At this time, the corrosion of the mild steel coupons depends on the charge transfer process. A close inspection of the impedance arc of the alloyed epoxy coatings revealed the presence of the capacitive loops formed in the high and low frequency regions. The semicircular loops in the low frequency region are depressed. Kumari *et al.* (2017); Bousskri *et al.* (2016) have attributed the depression in the semi-circles to surface roughness, inhomogeneity of solid surface, and an indication that corrosion process is mainly a charge transfer process. Capacitive loops shaped in the high frequency region, on the other hand, are less depressed. This means that the inner surface film is dense and provides consistent protection, as reported by Mahato and Singh (2011). The quality of the plots demonstrated a generally good corrosion prevention behaviour of Zn-Al-TiGSAC reinforced epoxy coatings which may be due to good dispersion and alignment of the alloy in the epoxy. The composite coatings showed only one capacitive time constant, suggesting that the corrosion process was not initiated on the substrate; therefore, the composite coatings prevented the underlying metal from direct contact with the aqueous corrosive environment of HCl electrolyte. The time constant refers to the barrier performance of organic coatings (Gonzalez-Garcia *et al.*, 2007).

The Nyquist plot for the composite coatings showed increase in diameter of the capacitive loop from ratio 1:1 to 2:1. Kumari *et al.* (2017); Gonzalez-Garcia *et al.* (2007) explained this to mean increase in corrosion resistance property. In the cases ratios of 3:1 and 4:1, diameter of the capacitive loop was seen to have decreased. The decrease in EIS radius means that Faraday process is promoted and the corrosion resistance is decreased. The radius of the frequency loop of neat epoxy in Figure 4.25 is smallest when compared with those of alloyed epoxy, indicating that the corrosion resistance property of neat epoxy coated steel is lowest among all coated samples. The neat epoxy coating is only better than the bare metal with very small EIS radius and two time constants. Corrosion resistant property of composite coatings increased with increase in nanoparticles/inhibitors concentration (Baghery *et al.*, 2010; Kumari *et al.*, 2017)

However, this was not the case in this study. In this investigation, corrosion resistance property increased with increase in amount of nanoparticles composites only to ratio of 2:1, after which there was decrease in the corrosion resistance property of the coatings. The result is similar to the findings of Chen *et al.* (2010) who investigated Ni-Al<sub>2</sub>O<sub>3</sub> coating using the jet electrodeposition method; which observed that the corrosion resistance behaviour of Ni-Al<sub>2</sub>O<sub>3</sub> coatings in 4% improved with increase in Al<sub>2</sub>O<sub>3</sub> content from 0 to 9.3%, after which the corrosion resistance property began to decrease and attributed the development to nanoparticles agglomeration at excess amount. However, the anti-corrosion behaviours of the coatings in this investigation may not be attributed to nanoparticles agglomeration because of the stabilization effects of GSAC support. Therefore, it is crucial to always use the appropriate amounts of nanoparticles for optimum coatings anti-corrosion performance. Optimum dispersion and

hydrophobicity may have been achieved at the ratio 2:1, hindering wetting of the surface and inhibiting diffusion of corrosive ions (Schaefer and Miszczyk, 2013). Further loading of alloys only served to create voids between filler particles arising from low mobility of epoxy matrix at higher filler content. These voids could allow for the penetration of corrosive ions towards the substrate.

The qualitative observations were corroborated by the quantitative interpretations of the EIS data obtained for all samples by fitting the electrical equivalent circuits (EEC) shown in Figure 4.31 (a and b). Suitable equivalent circuits are used to analyse the impedance data, depending on the shapes of the Nyquist plot (Kumari *et al.*, 2017). Consequently, in order to quantitatively compare the corrosion inhibition properties of the different coatings, the obtained experimental values from the EIS analysis was fit using the program

Z-simp win 3.21 software to obtain equivalent circuit diagram shown in Figure 4.28 (a and b).

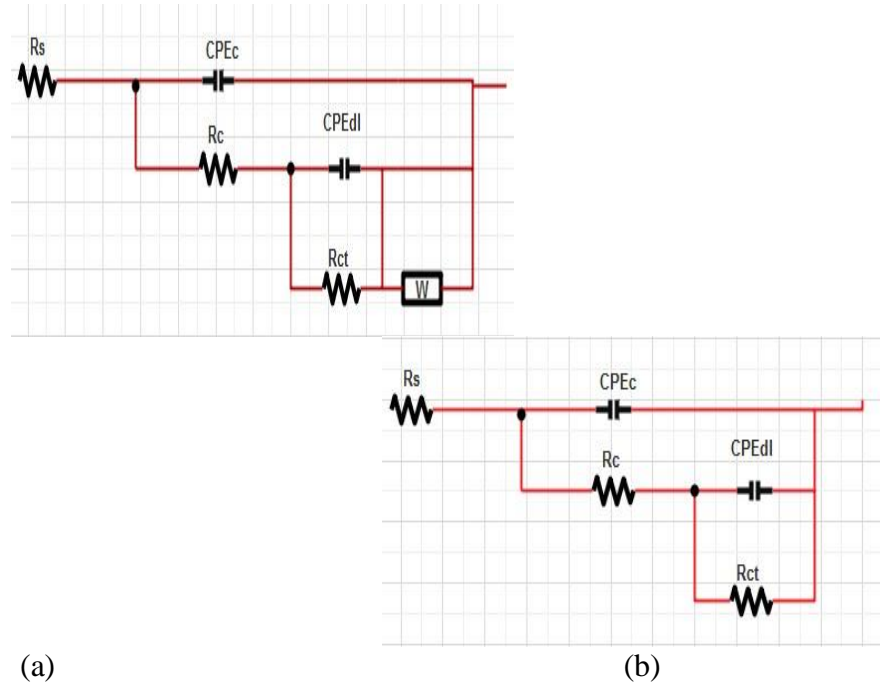


Figure 4.28: Equivalent circuit diagrams for fitting the EIS data

Figures 4.28 (a and b) represents an equivalent circuit that is widely used in electrochemical studies of corrosive medium/corrosion products/metal systems. A good fit with this model was obtained with an average error of about 2.0%.  $R_s$  is the solution resistance,  $R_c$  is the resistance of the coating on the mild steel working surface,  $R_{ct}$  is the charge transfer resistance, and  $W$  is the Warburg impedance.  $CPE_c$  and  $CPE_{dl}$  are constant phase angle elements representing the coating capacitance ( $C_c$ ) and the double layer capacitance ( $C_{dl}$ ), respectively. The presence of lower frequencies  $W$  loop for Figure 4.28 (a) may be attributed to the relaxation process obtained by adsorption species like  $H^+_{ads}$  and  $Cl^-_{ads}$  on the electrode surface (Veloz and González, 2002; Amin *et al.*, 2007). The

point of intersection between the capacitive loop and the real axis presents ( $R_s+R_{ct}$ ). The charge transfer resistance ( $R_{ct}$ ) is an important parameter, and is inversely proportional to the corrosion rate for each type of coating (Chenet *et al.*, 2011). The charge transfer resistances in HCl solution and other resulting electrochemical parameters are listed in Table 4.20. The impedance of these circuits can be expressed in Equation 4.2 as given by Tian *et al.* (2013).

$$Z_{CPE} = \frac{\omega^{-n}}{Y\left(\frac{\cos n\pi}{2} + j\frac{\sin n\pi}{2}\right)^n} \quad (4.2)$$

Where Y is the modulus of the CPE,  $\omega$  is the angular frequency, j is the imaginary number, and n is the deviation parameter.

The protection efficiency of the each nanocoatings over the mild steel electrode in the 1 M HCl electrolyte was calculated according to Equation (4.3),

$$P.E (\%) = \left(\frac{R_{ct} - R_{ct(0)}}{R_{ct}}\right) \times 100 \quad (4.3)$$

Where  $R_{ct}$  and  $R_{ct(0)}$  are the charge transfer resistances of the mild steel samples with and without various coatings in 1 M HCl solution, respectively.

The electrochemical parameters of the EIS experiment have been listed on Table 4.21.  
Table 4.21: Electrochemical parameters of EIS for samples

Nanocomposites	R <sub>c</sub> (KΩcm <sup>2</sup> )	R <sub>ct</sub> (KΩcm <sup>2</sup> )	CPE <sub>c</sub> (μFcm <sup>-2</sup> )	CPE <sub>dl</sub> (μFcm <sup>-2</sup> )	W	P.E
Uncoated sample	0.016	0.51	25.74	112.6	2.3 x 10 <sup>-3</sup>	-----
Neat Epoxy	0.076	3.42	6.67	56.78	5.8 x 10 <sup>-5</sup>	84.23
Zn-Al-Ti- GSAC/Epoxy (1:1)	0.33	12.86	18.75	60.33	-----	88.9
Zn-Al-Ti- GSAC/Epoxy (2:1)	0.81	42.51	5.58	38.89	-----	98.73
Zn-Al-Ti- GSAC/Epoxy (3:1)	0.72	20.91	7.19	43.89	-----	94.55
Zn-Al-Ti- GSAC/Epoxy (4:1)	0.58	8.47	8.46	58.67	-----	87.94

Result presented on Table 4.20 revealed that the R<sub>c</sub> and R<sub>ct</sub> values of the alloyed epoxy coated samples were larger than that of neat epoxy. High R<sub>ct</sub> value of 12.86 KΩcm<sup>2</sup> recorded for ratio 1:1 could be indicative of well adhered coating system according to Touzain *et al.* (2005); Heidarian *et al.* (2010). However, with increased loading of alloy at 2:1 ratio, the R<sub>ct</sub> value increased to 42.51 KΩcm<sup>2</sup> but decreased to 20.91 and 8.47 KΩcm<sup>2</sup> for ratios 3:1 and 4:1 respectively. This showed that the best interface reinforcement, and by extension, the best anti-corrosion property of the alloyed epoxy coating was achieved at ratio 2:1 after which the R<sub>ct</sub> value began to decrease. According to electrochemical theory, charge transfer resistance R<sub>ct</sub> is inversely proportional to the corrosion density (that is, corrosion rate). Ratio 2:1 sample presented the highest value of resistance as well as the lowest amount capacitance which Asadi *et al.* (2014) considered as key factors for protective coatings. The higher the values of C<sub>dl</sub>, the more serious the

delamination since polarization resistance  $R_p$  and double layer capacitance  $C_{dl}$  are the characteristics of the bare metal which do not appear in the EIS spectrum until the electrolyte traverses and make contact with the metal interface.

Similar trend was equally observed in the protection efficiency (P.E) for the coated samples. The highest protection efficiency of 98.73% was recorded for ratio 2:1 coated sample which decreased to 94.55 and 87.94% for ratios 3:1 and 4:1 coated samples respectively.

Previous investigations on corrosion resistant properties of similar systems and values of their Percentage Protection Efficiency (PE) in acidic solutions have been listed in Table

4.22 for comparative analysis.

Table 4.22: Comparison of the percentage corrosion protection (P.E)

S/N	Nanocomposites	Medium	P.E (%)	Reference
1	NME/Ag	1 M HCl	76.68	Atta <i>et al.</i> . (2013)
2	Ni-TiO <sub>2</sub>	1 M HNO <sub>3</sub>	53.48	Baghery <i>et al.</i> . (2010)
3	ZnO/polyacrylamide	1 M HCl	90.09	Morsi <i>et al.</i> . (2016)
4	ZnO/PVP	5 M HCl	90.81	Quadri <i>et al.</i> . (2017)
5	5/5%Ni-Zr-TiO <sub>2</sub>	3.5% NaCl + 1 M HCl	97.09	El-Lateef and Khalaf (2015)
6	Ni- RGO -TiO <sub>2</sub>	0.1 M acetic acid	82.39	El-Sayed <i>et al.</i> . (2019)
7	% SiC-MoSi <sub>2</sub>	0.05 M HCl	99.87	Mohamed <i>et al.</i> . (2013)
		0.05 M H <sub>2</sub> SO <sub>4</sub>	85.71	
		0.05 M HNO <sub>3</sub>	99.88	
8	6.0 wt. hydrophobic Polyaniline-SiO <sub>2</sub> (HPSC)	% 3.5%NaCl	96	Dhawan <i>et al.</i> . (2015)

It could be concluded from Table 4.22 that the Zn-Al-Ti-GSAC alloyed epoxy nanocomposite at ratio (2:1) is effective in deterring the corrosion of mild steel in a 1 M HCl environment. The high P.E (%) values (98.73%) further highlight the superior corrosion resistance property of the nanocomposite coatings in this study when compared with those of similar systems as referenced in Table 4.20. Corrosion inhibitors with a percentage safety efficiency greater than 70% were rated as excellent inhibitors by Umoren and Solomon (2017).

The cross sectional views of the bare steel, neat epoxy coated and ratio 2:1 alloyed epoxy coated samples have presented in Figure 4.32

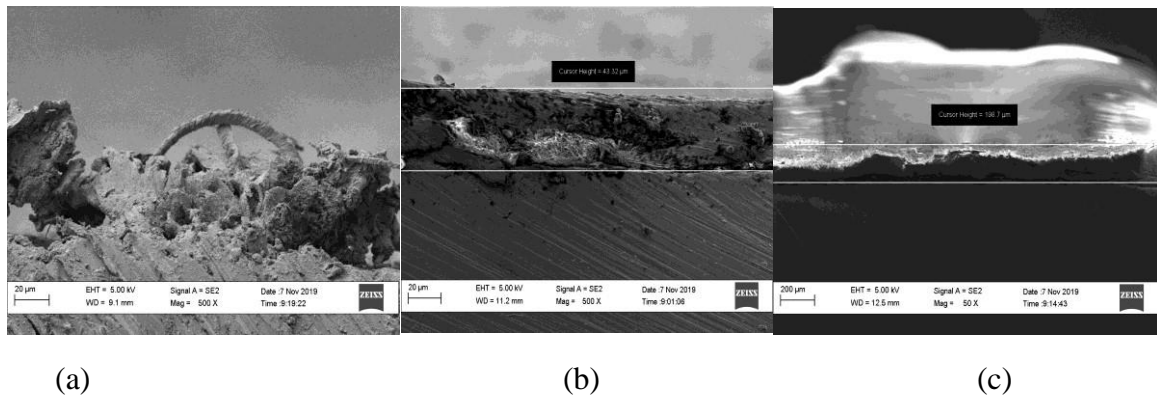


Figure 4.29: Cross-sectional view of SEM image for (a) bare metal (b) neat epoxy and (c) 2:1 alloyed epoxy coated samples

The SEM cross-sectional images shown in Figure 4.32 corroborated the electrochemical experiment result. From Figure 4.29 (a) which is the bare metal, it could be seen that the surface was substantially damaged owing to corrosion in the absence of an anticorrosion coating. The large pores observed on the top cross-section may be as a result of reaction

of metal particles with chloride ions leading to the damage of some parts of the substrate surface. This was similar to the result obtained by Da Silva *et al.* (2016). The ravaging Cl<sup>-</sup> ions were unhindered as they attacked the surface of the metal, probably due to the absence of organic protective film on the surface of the metal. In Figure 4.32 (b), some tiny voids were observed on the neat epoxy coating. Though the neat epoxy coating prevented complete damage of the substrate surface, as seen in Figure 4.32 (a), the tiny voids may have allowed the entry of some amount of aggressive species which resulted in some small parts of the underneath metal being damaged.

However, the surface of the underneath metal in Figure 4.32 (c) remained intact with no sign of corrosion or delamination. This could be attributed to the highest degree of cross linking and system homogeneity associated with ratio 2:1 coated sample.

## CHAPTER FIVE

### 5.0 CONCLUSION AND RECOMMENDATIONS

#### 5.1 Conclusion

The research work was focused on the development of Zn–Al–Ti nanocomposites supported groundnut shell activated carbon (GSAC) for the protection of mild steel AISI 1015 in 1 M HCl. From the above results, the following conclusions were drawn:

The Response Surface Methodology (RSM) was successfully used to optimize the process conditions in preparing activated carbon from groundnut shell where activation temperature was observed to exhibit the most significant effect on the activated carbon yield with *F-value* of 2413.99.

Calcination of optimized sample of groundnut shell activated carbon at 700°C for 2 hours recorded the best BET surface area of 751.92 (m<sup>2</sup>/g).

Zn, Al and Ti metal nanoparticles were successfully prepared using the sol- gel method, the Zn-Al-Ti metal nanocomposites were effectively hosted on GSAC and an average crystallite size of 35.24 nm for the metal nanoparticles and GSAC mixture at ratio 1:1.

The alloy (Zn-Al-Ti-GSAC) reinforced epoxy composites was successfully coated on mild steel substrates using the spraying gun method at an average coating thickness of 158.5 μm when Zn-Al-Ti-GSAC was loaded in epoxy matrix at different ratios of 1, 2, 3 and 4wt.%.

The hardness values of the metallic coatings showed increased in microhardness with increase in the loading of Zn-Al-Ti-GSAC in the epoxy from ratio 1 to 2wt.%, after which there was a decline while there was decrease in percentage volume of porosity with increase in weight fraction of Zn-Al-Ti-GSAC in the epoxy from ratio 1 to 2wt.% after which percentage porosity increased with further addition alloy into epoxy resin; thereby establishing an inverse relationship with micro hardness. However, the corrosion resistance property increased with increase in amount of loaded Zn-Al-Ti-GSAC in the epoxy matrix only to ratio 2:1 which recorded a charge transfer resistance ( $R_{ct}$ ) of 42.51  $K\Omega cm^2$  and Protection Efficiency (PE) of 98.73%., after which there was decrease in the coatings anti-corrosion performance.

## **5.2 Recommendations**

1. The anticorrosion properties of similar alloy coatings on mild steel in alkaline medium should be investigated and the results compared with the findings from this research work.
2. The effects of variation in coating thickness on the Protection Efficiency (PE) of developed Zn-Al-Ti-GSAC composites should be investigated.
3. Other mechanical properties such as tensile strength, wear resistance, toughness, brittleness of developed Zn-Al-Ti-GSAC composites should be investigated.
4. Effects of other coating methods on the Protection Efficiency (PE) of developed Zn-Al-Ti-GSAC composites should be studied.

## REFERENCES

- Abakah, R. R., Huang, F., Hu, Q., Wang, Y. & Jing, L. (2020). Comparative Study of Corrosion Properties of Different Graphene Nanoplate/Epoxy Composite Coatings for Enhanced Surface Barrier Protection *Coatings* 11, 285. <https://doi.org/10.3390/coatings11030285>
- Abdulrahman, M. A., Abubakre, O. K., Abdulkareem, S. A., Tijani, J. O., Aliyu, A. & Afolabi, A. S. (2017). Effect of Coating Mild Steel with CNTs on its Mechanical Properties and Corrosion Behaviour in Acidic Medium. *Advances in Natural Sciences: Nanoscience and Nanotechnology*, 8 (8).
- Abu-Thabit, N. Y. & Makhlof, A. S. H. (2015). Recent Advances in Nanocomposite Coatings for Corrosion Protection Applications. In Makhlof, A. S. H & Scharnweber, D. (Eds.), *Handbook of Nanoceramic and Nanocomposite Coatings and Materials*, 515-549 Butterworth-Heinemann, [doi.org/10.1016/B978-0-12-799947-0.00024-9](https://doi.org/10.1016/B978-0-12-799947-0.00024-9)
- Adullah, A. H., Kasim, A., Zainal, Z., Hussien, M. Z., Kuang, D. & Ahmad, F. (2001) Preparation and Characterization of Activated Carbon from Gelam Wood Bark (*Melaleuca cajupuli*) *Malaysian Journal of Analytical Science*, 7(1) 65 – 8
- Agapovichev, A. V., Kokareva, V. V., Smelov, V. G. & Sotov, A. V. (2016). Selective Laser Melting of Titanium Alloy: Investigation of Mechanical Properties and Microstructure *IOP Conf. Series: Materials Science and Engineering* 156 (2016) 012031 [doi:10.1088/1757-899X/156/1/012031](https://doi.org/10.1088/1757-899X/156/1/012031)
- Ahmad, T., Danish M., Rafatullah, M., Ghazali, A., Sulaiman, O., Hashim, R. & Ibrahim, M. (2012). The Use of Date Palm as a Potential Adsorbent for Wastewater Treatment: A Review. *Environ Sci Pollut Res* 19(5),1464 –1484
- Ahmad, A. A., Hameed, B. H., & Ahmad, A. L. (2009). “Removal of disperse dye from aqueous solution using waste-derived activated carbon: Optimization study,” *Journal of Hazard. Materials*,170, 612-619
- Ahmadpour, A. & Do, D. D. (1996). Carbon Emission. Oxford Publishing unit, USA 31
- Ahmadpour, A. & Do, D. D. (1997). The Preparation of Activated Carbon from Macadamia Nutshell by Chemical Activation, *Carbon* 35 (12),1723-32

- Ahmedna M., Marshall W. E. & Rao R. M. (2000), Production of Granular Activated Carbons from Select Agricultural By-products and Evaluation of their Physical, Chemical and Adsorption Properties. *Biosource Technology*, 71, 113-123 .
- Aigbodion, V. C., Atuanya, C. U., & Juku, G. S. (2011). Thermogravimetric Study: Polyethylene/Orange Peels Ash Composite, LAMBERT Academic Publishing.
- Aji, M. M., Gutti, B. & Highina, B. K. (2017). Production and Characterization of Activated Carbon (AC) from Groundnut Shell and its Application in Water Treatment University of Maiduguri, Faculty of Engineering Seminar Series,8
- Akande, I. G., Oluwole, O. O. & Fayomi, O. S. I. (2018). Optimizing the Defensive Characteristics of Mild Steel via the Electrodeposition of Zn-Si<sub>3</sub>N<sub>4</sub> Reinforcement Particles. *Defence Technology*,15(4)526-532
- Akbari, B., Tavandashti, M. P. & Zandrahim, I M. (2011). Particle Size Characterization of Nanoparticles —A practical Approach. *Iran. J. Mater. Sci. Eng.* 848–56
- Akinyemi, O. O., Nwaokocha, C. N. & Adesanya, A. O. (2012). Evaluation of Corrosion of Crude Oil Processing Industry. *Journal of Engineering Science and Technology*,7,(4)517 – 528.
- Alhamed, Y. A. (2006) Activated Carbon from Dates Stone by ZnCl<sub>2</sub> Activation *JKAU; Eng Sc*, 17 (2),75 – 100.
- Allahkaram, S. R., Golroh, S. & Mohammadalipour, M. (2011). Properties of Al<sub>2</sub>O<sub>3</sub> Nano-Particle Reinforced Copper Matrix Composite Coatings Prepared by Pulse and Direct Current Electroplating. *Mater. Des.*, 32: 4478-4484.
- Al-Qodah, Z. Shawabkah, R., & Eliseo A. G., (2009) “Production and Characterization of Granular Activated Carbon from Activated Sludge” *Braz J. Chem Eng*, 26(1): 127 – 36.
- Al-Qodah, Z. & Shawabkah, R. Onsecaa, E. & Amado, G (2016) “Production and Characterization of Granular Activated Carbon from Activated Sludge” *Chemical Engineering Transactions*.26, (1),127 - 136, January - March, 2009.
- Amin, M. A., Abd El-Rehim, S. S., El-Sherbini, E. E. F., & Bayyomi, R. S. (2007). The Inhibition of Low Carbon Steel Corrosion in Hydrochloric Acid Solutions by Succinic acid: Part I. Weight Loss, Polarization, EIS, PZC, EDX and SEM Studies. *Electrochimica Acta*, 52, 3588–3600.
- Andreola, F. Romagnoli, M. Leonelli, C. & Miselli, P. (2000). Techniques Used to Determine Porosity. *American Ceramic Society Bulletin*, July.

- Ankur, P. & Manivannan, R. (2015). A Study on Synthesis of Nickel Nanoparticles Using Chemical Reduction Technique. *Department of Chemical Engineering, National Institute of Technology, Raipur, Chhaisgarh, India.*
- Anyika, C., Asri, N. A. M., Majid, Z. A., Yahya, A. & Jaafar, J. (2017). Synthesis and Characterization of Magnetic Activated Carbon Developed from Palm Kernel Shells. *Nanotechnol. Environ. Eng.* 2, 16.
- Arami-Niya, A., Faisal, A., Mohammed, S. S., Wan Daud, W. M. A. & Sahu, J. N. (2012). Optimization of Synthesis and Characterization of Palm Shell Based Bio-Chars as a Bye-Product of Bio-Oil Production Process, *BioResources* 7(1), 246-264.
- Arandi, A., Landers R., Carnelli, P., Candal, R., Alarcon, H. & Rogriguez, J. (2019). Influence of Silver Electrochemically Deposited Onto Zinc Oxide Seed Nanoparticles on the Photoelectrochemical Performance of Zinc Oxide Nanorod Films. *Nanomaterials and Nanotechnology*, 9, 1-9.
- Asadi, A., Naderi, R., Saremi, M., Arman, S. Y., Fedel, M. & Deflorian, F. (2014). Study of Corrosion Protection of Mild Steel by Eco-Friendly Silane Sol- Gel Coating. *J. Sol-Gel Sci Tecnol* January, DOI 10.1007/s10971-014-3286-8.
- Ashimita, B. (2017). Anti-Corrosion Market Overview. *Allied Market Research.*
- Attia, A. A, Girgis, B. S. & Fathy, N. A. (2008). Removal of Methylene Blue by Carbons Derived from Peach Stones by 'H3PO4 Activation: Batch and Column Studies. *Dyes Pigments* 76,82–289
- Atta, A. M., & Al-lohedan, H. A. (2013). Corrosion Inhibition Efficiency of Modified Silver Nanoparticles for Carbon Steel in 1 M HCl. *International Journal of Electrochemical Science* 8, 4873–4885.
- Atta, A. M., El-Mahd, G. A., Al-Lohedan, H. A. & El-Saeed, A. M. (2015). Preparation and Application of Crosslinked Poly(sodium acrylate)-Coated Magnetite Nanoparticles as Corrosion Inhibitors for Carbon Steel Alloy. *Molecules*. 20(1), 1244-1261; doi.org/10.3390/molecules20011244
- Avolio, R., D'Albore, M., Guarino, V., Gentile, G., Cocca, M. C., Zeppetelli, S., Errico, M. E., Avella, M. & Ambrosio, L. (2016). Pure Titanium Particle Loaded Nanocomposites: Study on the Polymer/Filler Interface and hMSC Biocompatibility. *J Mater Sci: Mater Med* 27, 153. doi.org/10.1007/s10856-016-5765-7
- Awaja, F., Gilbertb, M., Kellya, G., Foxa, B., & Pigram, P. J. (2009). Adhesion of Polymers *Progress in Polymer Science* 34, 948–968

- Azargohar, R. & Dalai, A. K. (2005). Production of Activated Carbon from Luscar Char: Experimental and Modelling Studies. *Micropor Mesopor Mater* 85, 219-225
- Azlina, H. N., Hassidawani, J. N., Norita, H. & Surip, S. N. (2016). Synthesis of SiO<sub>2</sub> Nanostructure Using Sol- Gel Method. *5<sup>th</sup> International Science & Exhibition APMAS2015 Lykia Oludeniz*.
- Baghery, P., Farzam, M., Mousavi, A. B., & Hosseini, M. (2010). Surface & Coatings Technology Ni–TiO<sub>2</sub> Nanocomposite Coating with High Resistance to Corrosion and Wear. *Surface & Coatings Technology*, 204 (23), 2010; 3804–3810. <https://doi.org/10.1016/j.surfcoat.2010.04.061>
- Baladi, A. & Mamoory, R. S. (2010). *Applied Surface Science*. 256, 7559–7564
- Behzad, R. & Hamid, M. (2006). Applications of Titanium Dioxide Nanocoating. NanoTechnology in Environment Conference, Isfahan University of Technology, Isfahan, Iran,
- Benaddi, H., Badosz, T. J., Jagiello, J., Schwarz, J. A., Rouzaud, J. N., Legras, D. & Be'guin F. (2000). Surface Functionality and Porosity of Activated Carbons Obtained from Chemical Activation of Wood. *Carbon* 38(5):669–674.
- Benhebal, H., Chaib, M., Salomon, T., Geens, J., Leonard, A., Lambert, S. D., Crine, M. & Heinrichs, B. (2013). Photocatalytic Degradation of Phenol and Benzoic Acid Using Zinc Oxide Powders Prepared by Sol-gel Process. *Alex. Eng. J.*,52, 517–523.
- Bergna, D., Hu, T. Prokkala, H. & Lassi, U. (2019). Effects of Some Process Parameters on the Main Properties of Activated Carbon Produced from Peat in a Lab-Scale Process. *Waste Biomass Valor*.
- Boczkal, G and Perek-Nowak, M. (2014) Reconfiguration of Point Defects in FCC and HCP Metals at Initial Stage of Recovery Process. *Archives of Metallurgy and Materials*,59(4),78-80.
- Bolla, G. R., Debosshee, M. & Benjaram, M. R. (2017) Nanostructures for Novel Therapy: Synthesis, Characterization and Applications. *A Volume in Micro and Nano Technologies* Ed. Denisa, F. and Alexandru M. G.,1-36
- Bousskri, A., Anejjar, A., Salghi, R., Jodeh, S., Touzani, R., Bazzi, L. & Lgaz, H. (2016). Corrosion Control of Carbon Steel in Hydrochloric Acid by New Ec-Friendly Picolinium-Based Ionic Liquids Derivative: Electrochemical and Synergistic Studies. *Journal of Matters on Environmental Science* 7 (11) 4269-4289

- Budinova, T. Ekinic, E., Yardim, F., Grimm, A. Bjornborn, E. & Minkova, V. (2006) Characterization and Application of Activated Carbon Produced by H<sub>3</sub>PO<sub>4</sub> and Water Vapour Activation. *Fuel Process Technol*, 87:899-905
- Burris, D. L. (2007) Effects of Nanoparticles on the Wear Resistance of Polytetrafluoroethylene *Doctoral Thesis University of Florida* 2007
- Campbell, Q. P., Bunt, J. R., Kasaini, H. & Kruger, D. J. (2012). The Preparation of Activated Carbon from South African Coal. *Journal of South African Institute of Mineral Metallurgy*, 112:37 – 44
- Caturla, F., Molina-Sabio, M & Rodriguez-Reinoso (1994) Preparation of Activated Carbon by Chemical Activation with ZnCl<sub>2</sub>. *Carbon* 29 (1994) 999
- Chen, J., Huang, Y., Wei, C., Qiao, B., Yang, J. & He, Y. (2010). A Study on Ni-Al<sub>2</sub>O<sub>3</sub> Nanocomposite Coatings Prepared by Jet Electrodeposition. *Advanced Composites Letters*, Vol 19 Iss. 5, 2010
- Chen, M. A., Lu, X. B., Guo, Z. H., & Huang, R. (2011). Influence of Hydrolysis Time on the Structure and Corrosion Protective Performance of (3-mercaptopropyl) Triethoxysilane Film on Copper. *Corrosion Sciences*. 2011, 53, 2793,
- Chhetri, S., Samanta, P., Murmu, N. C. & Kuila, T. (2019). Anticorrosion Properties of Epoxy Composite Coating Reinforced by Molybdate-Intercalated Functionalized Layered Double Hydroxide. *J. Compos. Sci.* 2019, 3, 11; doi:10.3390/jcs3010011
- Chieh-Tsung, L., Laabs, F. C. & Narasimhan, B. (2004). *Journal of Polymer Science Part B: Polymer Physics*,42(14):2667–79
- Chowdhury, Z. Z., Zain, S. M., Khan, R. A. & Ashraf, M. A. (2011). Preparation, Characterization and Adsorption Performance of the KOH- Activated Carbons Derived from Kenaf Fibre for Lead (II) Removal from Waste Water. *Sci Res Essays*, 6(29),6185-96
- Chowdhury, Z. Z., Zain, S. M., Khan, R. A., Arami-Niya, A. & Khalid, K. (2012) Process Variables Optimization for Preparation and Characterization of Novel Adsorbent from Lignocellulosic Waste. *Bio Resources* 7(3), 3732-3754
- Chung, S. and Lin, J. (2016). Thermal Conductivity of Epoxy Resin Composites Filled with Combustion Synthesized h - BN particles. *Molecules* 21 (5): 670.
- Cripps, D. & Gurit, (2015). Epoxy resin. [Online] Available at: <http://www.netcomposites.com/guide/epoxy-resins/10> [Accessed 23 march 2020].
- Da Silva, R. C., Heinen, m., Lorenzi, G. A., Lima, D. W., Moura J. H. L. De Freitas, J. MMartini, E. M. A. & Petzhold, C. I. (2019). Carbon Steel Corrosion Controlled by

- Vegetable Polyol, in Medium Containing Chloride and Glyoxal: Influence of Phosphate Content and CO<sub>2</sub> *Heliyon*. doi.org/10.1016/j.heliyon.2019.e01720
- Das, D., Depi, P. S. & Meikap, B. C. (2015). Preparation of Activated Carbon from Green Coconut Shell and its Characterization, *J. Chem Eng. Process Technol.*
- Deen, K. M., Ahmed, R. & Khan, I. H. (2009). Corrosion Protection Evaluation of Mild Steel Painted Surface by Electrochemical Impedance Spectroscopy. *Journal of Quality and Technology Management*
- Demiral, I. & Aydin-Samdan, C. (2016). Preparation and Characterization of Activated Carbon from Pumpkin Seed Shell Using H<sub>3</sub>PO<sub>4</sub>. Anadolu University. *Journal of Science and Technology A-Appl Sci and Eng.* 17(1),125-138
- Dhawan S. K., Anoop, K. S., Hema, B., Bisht, B. M. S. & Fehmeeda, K. (2015). Development of Highly Hydrophobic and Anticorrosive Conducting Polymer Composite Coating for Corrosion Protection in Marine Environment. *American Journal of Polymer Science*, 5(A1) 7-17
- Dias, J. M., Alvin-Ferraza, M. C. M., Almeida, M. F., Rivera-Utrilla, J. & Sanchez-Polo, M. (2007). Waste Materials for Activated Carbon Preparation and its Use in Aqueous Phase Treatment: A Review. *Journal of Environmental Management*, 85,833-46
- Ding, Y. & Wang, Z. L. (2009) Structures of Planar Defects in ZnO Nanobelts and Nanowires. 40,335–342.
- Dipa, D., Dep, P. S. & Meikap, B. C. (2015). Preparation of Activated Carbon from Green Coconut Shell and its Characterization. *Journal of Chemical Engineering Process Technology*,6 (5): doi:10.4172/2175 – 7048.1000248
- Donald, J., Ohtsuka, Y. & Xu, C. C. (2011). Effects of Activation Agent and Intrinsic Minerals on Pore Development in Activated Carbons Derived from a Canadian Peat. *Mater Lett* 65:744-7
- Dutta, S., Chattopadhyay, S., Sarkar, A., Chakrabarti, M., Sanyal, D. & Jana, D. (2009). Role of Defects in Tailoring Structural, Electrical and Optical Properties of ZnO. *Progress in Materials Science*, (54, No. 1, 2009, 89-136. doi.org/10.1016/j.pmatsci.2008.07.002
- Egbe, E. A. P. & Onuoha, D. C. (2016). Effects of Weight Fraction and Soaking Temperature on Mechanical Properties of Groundnut Shell Ash Reinforced Epoxy Composite. *SSRG International Journal of Mechanical Engineering (SSRG-IJME)*, 3, 6
- El-Lateef, H. M. A. & Khalaf, M. M. (2015). Corrosion Resistance of ZrO<sub>2</sub>TiO<sub>2</sub> Nanocomposite Multilayer thin Films Coated on Carbon Steel in Hydrochloric Acid Solution. *Materials Characterization*, 108, 29–41.

- El-Sayed, K., Hamid, Z. A., Salah, T. A., & Khalil, M. W. (2019). Anti-Corrosion Nickel / Reduced Graphene Oxide-Titanium Dioxide Coating for Mild Steel in Organic Acids. *Journal of Materials and Environmental Sciences*, 10(2), 141–162.
- El-Sheikh, A., Newman A., Al-Daffae H., Phull S. & Crosswell N. (2003). Characterization of Activated Carbon Prepared from a Single Cultivar of Jordanian Olive Stones By Chemical and Physicochemical Techniques. *J. Anal. Appl. Pyrolysis*, 30, 1-16.
- Eric, P. L. (2010). Production, Characterization, and Applications of Activated Carbon Masters Thesis, University of Missouri.
- Eugene, U., Donnel, P. S., Ifeoma, V. J. & Feyisayo, V. A. (2016). The Effect of Corrosion Inhibitors on Stainless Steels and Aluminum Alloys: A Review Vol.10(2), 23-32 , March 2016: doi.org/10.5897/AJPAC2016.0676
- Fang, Z. Z., Paramore, J. D., Sun, P., Chandran, K.S. R., Zhang, Y., Xia, Y., Cao, F., Koopman M. & Free, M. (2018) Powder metallurgy of titanium – past, present, and future, *International Materials Reviews*, 63:7, 407-459, doi: 10.1080/09506608.2017.1366003.
- Fatoba, O. S., Popoola, A. P.I. & Aigbodion, V. S. (2015). Experimental Study of Hardness Values and Corrosion Behaviour of Laser alloyed Zn-Sn-Ti Coatings of UNS G10150 Mil Steel, *Journal of Alloys and Compounds* 658, 248 - 254
- Fayomi, O.S. I., Popoola, A.P. I. & Aigbodion, V. S. (2015). Investigation on Microstructural, Anti-Corrosion and Mechanical Properties of Doped Zn-Al-SnO<sub>2</sub> Metal Matrix Composite Coating on Mild Steel, *J. Alloys and Compounds* 622, 325334
- Fontana, M.G (1987). Corrosion Engineering, 3rd Ed., Mc Graw-Hill Book Co, Singapore.
- Fuentes, E., Alves, S., Lopez-Ortega, A., Mendizabal, L., & de Viteri, V. S. (2019). Advanced Surface Treatments on Titanium and Titanium Alloys Focused on Electrochemical and Physical Technologies for Biomedical Applications. In: Barbeck, M., Jung, O., Smeets, R & Korzinskas. (Eds), *Biomaterials-Supported Tissue Reconstruction or Regeneration*, IntechOpen Doi:10.5772/intechopen.85095
- Fustes, J., Gomes, A. & da Silva Pereira, M. I. (2008). Electrodeposition of Zn-TiO<sub>2</sub> Nanocomposite Films- Effects of Bath Composition. *J. Solid State Electrochem.* 12, 1435- 1443

- Fuyou, L., Chunmiao, H. & Wei, F. (2013). Upconversion-Nanophosphor-Based Functional Nanocomposites. *Advanced Materials*. 25,37,5287-5303
- Ganeev, R. A., Boltaev, G. S., Tugushev, R. I. & Usmanov, T. (2010). Nanoparticle Formation During Laser Ablation of Metals at Different Pressures of Surrounding Noble Gases. *Applied Physics A*, 100, 119-123
- Gao, W., Zhang, Z., Chen, B., Ma, X. & Yan, B. (2017). Effects of Calcinations Temperature on the Structure and Adsorption Performance of Ce-Mn/ Activated Carbon Materials. *Wuhan University J. Nat Sci* 1007-1202,05-0435-08
- Ghaziof, S. & Gao, W. (2015) Mechanical and Chemical Properties of Zn-Ni-AL<sub>2</sub>O<sub>3</sub> Nanocomposite Coatings, *Int. J. Chem. Mol. Nucl. Matter. Metallic Eng.* 9 (8),945949
- Ghorbani, H. R. A (2014). Review of Methods for Synthesis of Al Nanoparticles. *Orient J Chem*, 30(4): doi.org/10.13005/ojc/300456
- Gigliola, L., Corrado, B., Federica, G. & Giulia, P. (2017). Synthesis and Characterization of TiO<sub>2</sub> Nanoparticles for the Reduction of Water Pollutants. *Materials*.
- Gong, T., Qin, L., Zhang, W., Wan, H., Lu, J. & Feng, H. (2015). Palladium Nanoparticle Catalysts Synthesis by Atomic Layer Deposition: Genesis and Evolution of Nanoparticles and Tuning the Particle Size. *J. Phys. Chem. C*, 119, 21, 11544115556: doi.org/10.1021/jp5130102
- Gonzalez-Garcia, Y., Gonzalez, S. & Souto, R. M. (2007). Electrochemical and Structural Properties of a Polyurethane Coating on Mild Steel Substrate for Corrosion Protection. *Corrosion Science*. 49, (9),3514 - 3526
- Gorla, C. R., Emanetoglu, N. W., Liang, S., Mayo, W. E., Lu, Y., Wraback, M. & Shen, H. (1999) Structural, Optical, and Surface Acoustic Wave Properties of Epitaxial ZnO Films Grown on (0112) Sapphire by Metalorganic Chemical Vapor Deposition. *J. Appl. Phys.*, 1999. 85: doi.org/10.1063/1.369577
- Goso, X. & Kale, A. (2011). Production of titanium metal powder by the HDH process. *The Journal of The Southern African Institute of Mining and Metallurgy*. Vol 111, March 2011
- Guo, S., Peng, J., Li, W., Yank, K., Zhnag, L. & Zhang, S., (2009) Effects of CO<sub>2</sub> Activation on Porous Structure of Coconut Shell-Based Activated Carbon. *Appl Surf Sci* 2009; 255:8443-9
- Guo, D., Xie, G. and Luo, J. (2014). Mechanical Properties of Nanoparticles: Basics and Applications. *J. Phys D: Appl. Phys* 47(1):3001-3024

- Gupta, V. K., Mittal, A. and Gajbe, V. (2005). Adsorption and Desorption Studies of a Water-Soluble Dye, Quinoline Yellow, Using Waste Materials. *J Colloid Interface Sci* 284(1):89–98.
- Gupta, V. K & Rastogi, A. (2009). Biosorption of Hexavalent Chromium by Raw and Acid-Treated Green Alga *Oedogonium Hatei* from Aqueous Solutions. *J Hazard Mater* 163(1),396–40.
- Habeeb, H. J., Luaibi, H. M., Dakhil, R. M., Kadhum., A. M. H., Al-Amiery., A. A. & Gaaz, T. S. (2018). Development of a New Corrosion Inhibitor Tested on Mild Steel Supported by Electrochemical Study. *Results in Physics* (5) 1250-1267
- Hamid, S. & Seyyed, A. J. J. (2014). Effects of Titanium Dioxide Nanoparticles on the Mechanical Properties of Vinyl Ester-Based Nanocomposites. *J Comp Mat*, 49(19), 2365-2373
- Hanemann, T. & Szabo, D. V. (2010). Polymer - Nanoparticle Composites: From Synthesis to Modern Applications. *Materials*, 3(6) 3468 - 3517
- Harris, F. W. & Spinelli, H. J. (1985). *Reactive Oligomers*. American Chemical Society, Washington.
- Harris, P. J. F., Lie, Z. & Suenaga, K. (2008). Imaging the Atomic Structure of Activated Carbon. *Journal of Physical Condensation Matter*, 20: 1 – 5.
- Harish, K. K., Nagasamy, V., Himangshu, B. & Anuttam, K. (2018). Metallic Nanoparticles: A Review. *Biomed J Sci & Tech Res* 4(2).
- Hassan, I. C., Itodo, A. U. & Umar, U. B. (2010). Equilibrium Study on the Biosorption of Malachite Green from Aqueous Solution onto Thermochemically Cracked Groundnut Groundnut Shells. *Journal of Chemical Pharmaceutical Research*, 2(3),656-66
- Hassanpour, P., Panahi, Y., Ebrahimi-Kalan, A., Akbarzadeh, A., Davaran, S., Aygun, N. N., Khalilov, R. & Kavetsky, T. (2018). Biomedical Applications of Aluminum Oxide Nanoparticles. 13(9),1227-1231
- Hayashi, J. I., Horikawa, T., Takeda, I., Muroyama, K. & Nasir, A. F. (2002). Preparing Activated Carbon from Various Nutshells by Chemical Activation with  $K_2CO_3$ . *Carbon* 40:2381–2386
- Hayashi, J., Kazehaya, A., Muroyama, K. & Watkinson, A. P. (2000). Preparation of Activated Carbon from Lignin by Chemical Activation. *Carbon*. 38,1873-8

- Hefni, H. H.; Azzam, E. M.; Badr, E. A.; Hussein, M. & Tawfik, S. M. (2016). Synthesis, characterization and anticorrosion potentials of chitosan-g-PEG assembled on silver nanoparticles. *International Journal Biological Macromology*, 83,297–305
- Heidarian, M., Shishesaz, M., Kassiriha, S., & Nematollahi, M. (2010). Characterization of Structure and Corrosion Resistivity of Polyurethane/Organoclay Nanocomposite Coatings Prepared through an Ultrasonication Assisted Process. *Progress in Organic Coatings*, 68, 180-188.
- Herle, R., Shetty P, Shetty S.D. & Kini, U. A. (2011). Corrosion inhibition of 304 SS in hydrochloric acid solution by N – Furfuryl N'- phenyl thiourea. *Portugaliae Electrochim. Acta* 29:69-78.
- Hu, Z. & Srinivasan, M. P. (2001). Mesoporous High Surface Area Activated Carbon. *Micro Meso Mater.* 43:267-75
- Hushman, A., Daud, W. M.A W. & Shaffeyan, M. S. (2011). Tailoring the Surface Area of Activated Carbon by Nitric Acid: Study Using Response Surface Methodology Method. *Build. Chemical Society of Japanese.* 84, 11, 1251-1260.
- Ibrahim, M., Kannan, K., Parangusan, H., Eldeib, S., Shehata, O., Ismail, M., Zarandah, R. & Sadasivuni, K. K. (2020). Enhanced Corrosion Protection of Epoxy/ZnO-NiO Nanocomposite Coatings on Steel. *Coatings.* 10, 783
- Ievtushenko, A., Khyzhun, O., Shteplyuk, I., Tkach, V., Lazorenko, V. & Lashkarev, G. (2013). X-ray Photoelectron Spectroscopy Study of Nitrogen and AluminumNitrogen Doped ZnO Films. *ACTA PHYSICA POLONICA A* 124,(5), 67-78.
- Ioannidou, O. & Zabaniotou, A. (2007). Agricultural Residues as Precursors for Activated Carbon Production. *Renewable and Sustainable Energy Reviews.* 1, 1966 – 2005 doi:10.1016/j.rser. 2006.03.013
- Irfan, H., Mohamed, R. K. & Anand, S. (2018). Microstructural Evaluation of CoAl<sub>2</sub>O<sub>4</sub> Nanoparticles by Williamson-Hall and Size-Strain Plot Method. *Journal of Asian Ceramic Societies* 6,1.
- Jang, J. S., Yu, C. J., Choi, S. H., Ji, S. M., Kim, E. S. & Lee, J. S. (2008). Topotactic Synthesis of Mesoporous ZnS and ZnO Nanoplates and their Photocatalytic Activity. *J Catal.* 2008; 254:144–155
- Jankowska, H., Swiatkowski, A. & Choma, J. (1991). Active Carbon. Ellis Horwood Limited.Junot de B. (1848) Fr. Pat. 3564 (1848)
- Jassim, A. N., Amlah, L. K., Ali, D. F. and Aljiabar, A. T. A. (2012). P reparation and

Characterization of Activated Carbon from Iraqi Apricot Stone *Can J Chem Eng Technol*, 3,60 – 5

Jinhuan, J., Jiang, P. & Jiye, C. (2018). The Advancing of Zinc Oxide Nanoparticles for Biomedical Applications. *Bioinorganic Chemistry and Applications*, Article ID 1062562, 18 pages

Kakiuchi, K., Hosono, E., Kimura, T., Imai, H. & Fujihara, S. (2006). Fabrication of Mesoporous ZnO Nanosheets from Precursor Templates Grown in Aqueous Solutions. *Journal of Sol-Gel Sci Technol.* 39,63–72.

Kalders, D., Koutoulakis, D., Paraskeva, P., Diamadopoulos, E., Otal, E., Valle, J. O. D. & Fernandez-Pereira, C. (2008). Adsorption of Polluting Substances on Activated Carbons Prepare from Rice Husk and Sugarcane Bagasse. *Chemical Engineering Journal*, 144(1), 42–50.

Kalderis, O., Bethains, S., Paraskeva, P. & Diamodopoulus, E. (2008). Production of Activated Carbon from Bagasse and Rice Husk by a Simple Stage Chemical Activation Method at Low Retention Times. *Bioresour Technol.*, 99:6809-16

Kamaraj, M. & Umamaheswari (2017). Preparation and Characterization of Groundnut Shell Activated Carbon as an Efficient Adsorbent for the Removal of Methylene Blue Dye from Aqueous Solution with Microbiostatic Activity. *Journal of Materials and Environmental Science* 2017 8 (6) pp 2019 – 2025

Kamil, F., Hubiter, K. A., Abed, T. K. & Al-Amiery, A. A (2016). Synthesis of Aluminum and Titanium Oxides Nanoparticles Via Sol-Gel Method: Optimization for the Minimum Size. *Journal of Nanoscience and Technology*, 2(1) (2016) 37–39

Kannan, N. & Sundaram, M. M, (2001). Kinetics and Mechanism of Removal of Methylene Blue by Adsorption on Various Carbons: A Comparative Study. *Dyes Pigments* 2001, 51:25–40

Kaur, B. and Bhattacharya, S. N. (2011). Automotive Dyes and Pigments. *A Handbook of Textile and Industrial Dyeing*, 2011 vol 2 231-251

Kendig, M. W. & Buchheit, R. G. (2003). *Corrosion*, 59 (2003) 379.

Khalifaoui, A., Bendjamaa, I., Bensid, T., Meniai, A. H., & Derbal, K., (2014). Effects of Calcination on Orange Peels Characterization: Applications of in Industrial Dye Adsorption, *Chemical Engineering Transactions*, 38, 361 – 366.

Khalili, N. R., Campbell, M., Sandi, G. & Gola, J. (2000). Production of Micro and Mesoporous Activated Carbon from Paper Mill Sludge: Effect of zinc chloride activation. *Carbon*, 38, 1905-1915.

- Khodaei, P., Shabani-Nooshabadi, M. & Behpour, M. (2019). Epoxy-Based Nanocomposites Coating Reinforced by a Zeolite Complex: It's Anti-Corrosion Properties on Mild Steel in 3.5 wt.% NaCl Media. *Progress in Organic Coatings*. 105254
- Khwaja, S. S., Aziz, R. Tajuddin, & Azamal, H. (2018). Properties of Zinc Oxide Nanoparticles and their Activity Against Microbes. *Nanoscal Res Lett*. 13; 141
- Kim, C. H. & Kim, B. H. (2015). Zinc Oxide/Activated Carbon Nanofiber Composites for Higher Performance Supercapacitor Electrodes. *Journal of Power Sources*, 274, 512 – 520.
- Komeili, S., Takht Ravanche, M. & Taeb, A. (2016) Influence of Calcination Parameters on the Properties of Alumina as a Catalyst Support. *Scientia Iranica. Transactions C Chemistry and Chem Engr* 23, 1128 - 1135
- Kosek, J. R., DuPoint, J. N. & Marder, A. R. (1995) Effects of Porosity on Resistance of Epoxy Coatings to Cold-Wall Blistering. *Corrosion*.51(11)
- Kumar, A. M., Khan, A., Suleiman, R., Qamar, M., Saravanan, S. & Dafalla, H. (2018). Bifunctional CuO/TiO<sub>2</sub> Nanocomposite as Nanofiller for Improved Corrosion Resistance and Antibacterial Protection. *Prog. Org. Coat*. 114, 9–18
- Kumari, P. P., Shetty, P. & Rao, S. A. (2017). Electrochemical Measurement for the Corrosion Inhibition of Mild Steel in 1 M Hydrochloric Acid by Using an Aromatic Hydrazide Derivative. *Arabian Journal of Chemistry*. 10, 653-663
- Lafi, W. (2001). Production of Aactivated Carbon from Acrons and Olive Seed Biomass. *Biomass and Bioenergy*, 20, 57-62.
- Lai, S. M., Yeh, F. C., Wang, Y., Chan, H. C. & Shen, H. F. (2003). Comparative study of Maleated Polyolefins as Compatibilizers for Polyethylene/Wood Flour Composites. *Journal of Applied Polymer Science*, 87(3), 487-496.
- Laine, J., Calafat, A. & Labady, M. (1989). Preparation and Characterization of Activated Carbons from Coconut Shell Impregnated with Phosphoric Acid. *Carbon*, 27, 191195.
- Lee, B. J., Song, H. J. & Jeong, J. (2015). Structural and X- Ray Photoelectron Spectroscopy Study of Al- Doped Zinc-Oxide Thin Film. *Advances in Materials Science and Engineering*. 4(2), 55-67.
- Lee, Y. J., Lee, C. & Lee, H. M. (2018). Synthesis of oxide-free aluminum nanoparticles for application to conductive film Nanotechnology. 2018;29(5):055602 doi: 10.1088/1361-6528/aa9c1b

- Lee, Y. W., Pak, J. W., Choung, J. H. & Choi, D. K. (2002). Adsorption Characteristics of SO<sub>2</sub> on Activated Carbon Prepared from Coconut Shell with Potassium hydroxide Activation. *Environ Sci Technol*, 36:1086 - 92
- Leisner, P. & Benzon, M. E. (2017) Porosity Measurements on Coatings. *Laboratory Techniques tutorials Trans IMF*, 75(2), 88
- Li, H., Meziani, M. J., Lu, F., Bunker, C. E., Gulians, E. A. & Sun, Y. P. (2009). Templated synthesis of aluminum nanoparticles - A new route to stable energetic materials *Journal of Physical Chemistry C*. 113, 20539-20542.  
Doi: 10.1021/Jp908681P
- Lillo-Rodens, M. A., Cazorla-Amoros, D. & Linares-Solano, A. (2003). Understanding Chemical Reaction between Carbons and NaOH and KOH: An Insight into the Chemical Activation Mechanism. *Carbon*. 41,267-75
- Lu, X., Wang, S., Xiong, T., Wen, D., Wang, G. & Du, H. (2019). Anticorrosion Properties of Zn-Al Composite Coating Prepared by Cold Spraying. *Coatings*. 9(3), 210 doi:10.3390/coatings9030210
- Lua, A. C. & Yang, T. (2004). Effects of Activation Temperature on the Textural and Chemical Properties of Potassium Hydroxide Activated Carbons. *Journal of Analytical and Applied Pyrolysis*, 76, 96-102.
- Lunder, O., Simensen, C., Yu, Y., & K. Nisancioglu (2004). Formation and Characterisation of Ti–Zr Based Conversion Layers on AA6060 Aluminium, *Surface Coating Technology* 184, 2-3, 278- 290
- Lusi, E., Ratna, B., Takashi, O., Kikuo, O. & Tomonori, T. (2017) Role of Acetone in the Formation of Highly Dispersed Cationic Polystyrene Nanoparticles. *Chemical and Process Engineering*. 38(1), 5 – 18
- Mahato, N. & Singh, M. (2011). Investigation of Passive Film Properties and Pitting Resistance of AISI 316 in Aqueous Ethanoic Acid Containing Chloride Ions Using Electrochemical Impedance Spectroscopy (EIS). *Portugaliae Electrochimica Acta*, 29, 233-251.
- Mahmud, S. & Abdullah, M. J. (2006) Nanotripods of Zinc Oxide, *IEEE Conf. Emerging Technol.—Nanoelectron*. 442–446
- Mahmud, S., Johar, M., Abdullah, P. G. A., Chong, J. & Mohamad, A. K. (2006) Nanostructure of ZnO Fabricated via French Process and its Correlation to Electrical Properties of Semiconducting Varistors. *Synth React Inorg Met Org Chem Nano-Met Chem*. 36,155–159

- Malatji, A. & Popoola, A. P. I. (2015). Electrodeposition of Ternary Zn-Cr<sub>2</sub>O<sub>3</sub>-SiO<sub>2</sub> Nanocomposite Coating on Mild Steel for Extended Applications, *International Journal of Electrochemical Science*, 10,3988 – 4003
- Malik, R., Ramteke, D. S. & Wate, S. R. (2006) Physico-Chemical and Surface Characterization of Adsorbent Prepared from Groundnut Shell by ZnCl<sub>2</sub> Activation and its Ability to Adsorb Colour, *Indian Journal of Chemical Technology*, 13, 319328
- Mamun, A. A., Heim, H. P. & Bledzki, A. K. (2015). The Use of Maize, Oat, Barley and Rye Fibres as Reinforcements in Composites. *Biofiber Reinforcement in Composites Material*, 2015, 454-487: doi.org/10.1533/9781782421276.4.454
- Mansooreh, S. & Tahereh, K. (2008) Activated Carbon Shell of Apricot Stones: A promising Adsorbent in Gold Recovery. *China Journal of Chemical Engineering*, 16 (1),112- 118
- Mansooreh, S. & Tahereh, K. (2007) Agricultural Waste Conversion to Activated Carbon by Chemical Activation with Phosphoric Acid *Chemical Engineering Technology Journal*, 30,5, 649–654 DOI: 10.1002/ceat.200600325
- Manoj, K. R. P., Mahammadunnisa,S., Ramaraju B., Sreedhar, B. & Subrahmanyam, C. (2013) Low-Cost Adsorbents from Biowaste for the Removal of Dyes from Aqueous Solution. *Environ Sci Pollut Res* 20(6),4111–4124
- Mantia, F. P. & Morreale, M. (2011). Green Composite: A Brief Review. *Composite Part A: Applied Science and Manufacturing* 579 -588.
- Marcus, M., Ristic, M., Ivanda, M & Music, S. (2012). Formation of Iron Oxides by Surface Oxidation of Iron Plate. *Croatia Chemical Acta*, 85 (1), 117 - 124
- McDougall, G. J. (1991) The Physical Nature and Manufacture of Activated Carbon, *Journal of the South African Institute of Mining and Metallurgy*, 91,4, 109-120.
- Menendez-Diaz, J. A. & Martin-Gullon, I (2006) Activated Carbon Surfaces in Environmental Remediation (Interface Science and Technology Series, 7) T. Bandosz Ed. ELSEVIER 2006 1-48.
- Miguel-Angel, P., Francisco, M., Quetzalcoatl, H. & Alberto-Jesus, P. (2018). Peanut Shell for Energy: Properties and its Potential to Respect the Environment. *Sustainability*, 2018, 10, 3254
- Mishra, D., Mishra, K. M., Singh, N. & Haque, F. Z. (2016). Photoluminescence Based Fast Detection of Ammonia Gas Through TiO<sub>2</sub> Nanoparticles. *J A.* 5,3,220-224
- Moezzi, A., Cortie, M. and McDonagh, A. (2011) Aqueous Pathways for the Formation of Zinc Oxide Nanoparticles. *Dalton Trans.* 40,4871–4878.

- Mohamed, M. Rashidi, N. A., Yusup, S., Teong, L. K. Rashid, U. & Ali, R. M. (2012) Effects of Experimental Variables on Conversion of Cockle Shell to Calcium Oxide Using Thermal Gravimetric Analysis. *Journal of Cleaner Production*, 37, 394-397
- Mohamed, M. J. S., Selvakumar, N., Jeyasubramanian, K. & Vettivel, S. C. (2013). Numerical Modelling on Corrosion Behaviour of Molybdenum Based Ceramic Nanocomposite Coated Mild Steel Using Response Surface Methodology. *International Journal of Surface Science and Engineering*, 7,4. <https://doi.org/10.1504/IJSURFSE.2013.057613>.
- Mohammed, M., Babagana, G. & Bitrus, K. H. (2015) Production and Characterization of Activated Carbon from Groundnut Sourced in Maiduguri. *Columbian Journal of Life Sciences*, 17,1,18 – 24.
- Mohd, Z. M. N., Najaatul, A. S. & Sonny, I. (2018) Surface Modification of Aluminum Oxide (Al<sub>2</sub>O<sub>3</sub>) Nanoparticles (NPs) on Detection of Crude Oil Production (2018) Presented at Environment, Green Technology and Engineering *International Conference (EGTEIC 2018) Caceres, Spain, 18-20 June, 2018*
- Monaliben S., Derek F., Shashi S., Suraj K. T., & Gérrard, E. J. P. (2015). Green Synthesis of Metallic Nanoparticles via Biological Entities. *Materials*, 8(11): 7278– 7308
- Montemora, M. F., Pinto, R., & M.G. S. Ferreira (2009): Chemical Composition and Corrosion Protection of Silane Films Modified with CeO<sub>2</sub> Nanoparticles *Electrochim. Acta* 54, 5179.
- Muralidhara, H. B., Balasubramanyam , J., Arthobanaik, Y., Yogesh Kumar, K., Hanumanthappa, H. & Veena, M. S. (2011). Electrodeposition of Nanocrystalline Zinc on Steel Substrate from Acid Sulphate Bath and its Corrosion Study. *Journal of Chemical and Pharmaceutical Research*, 3(6): 433 – 449
- Myer, R. H. & Montgomery, D. C. (2002). *Response Surface Methodology: Process and Product Optimization Using Designed Experiment*, 2<sup>nd</sup> Ed., John Wiley and Sons., USA
- Nalwa, H. S. (2000). *A Handbook of Nanostructured Materials and Nanotechnology*, Vol. 1 Academic Press, San Diego, 1-56
- Nasehir, K. E. M., Muhamad, F. P. M. L., Ismail, A. & Mohd, A. A. (2010). Effects of Preparatory Conditions of Activated Carbon Prepared from Rice Husk by ZnCl<sub>2</sub> Activation for Removal of Cu(II) from Aqueous Solution. *International Journal of Engineering & Technology*, 10, 6,67-68.

- Naser, A.A. & Fahad, B. M. (2018). Adhesion Test for Epoxy Reinforcing Using Waste Materials Applied on Concrete Surface. *IOP Conf. Series: Materials Science and Engineering* 433, 0120004
- Natarajan, K. A. (2013). Lecture 1: Corrosion Introduction – Definition and Types; NPTEL course, <http://www.nptel.iitm.ac.in/courses/113108051/module1/lecture1.pdf>, accessed on June 27, 2013
- Nath, K., Panchani, S., Bhakhar, M. S. & Chatrola, S. (2013) Preparation of Activated Carbon from Dried Pods of Prosopis Cineraria with Zinc Chloride Activation for the Removal of Phenol. *Environmental Science of Pollution Research*, 20(6):4030–4045
- Nasih, M. N. & Vicki, W. V. (2018). Effect of Epoxy/Al<sub>2</sub>O<sub>3</sub>/CeO<sub>2</sub> Coating on Corrosion Rate and Mechanical Properties of Mild Steel. *International Journal of Engineering & Technology*, 7 (4.35).194-197
- Nguyen-Tri, P., Nguyen, T. A., Carriere, P., & Xuan, C. N. (2018). Nanocomposite Coatings: Preparation, Characterization, Properties, and Applications *International Journal of Corrosion*, Article ID 4749501, 19 pages <https://doi.org/10.1155/2018/4749501>
- Nitin, A. J., Chan, W. K., Umapada, P., Jinheung, K. & Young, S. K. (2012) Concentration and Temperature Effects on Controlling Pore Size and Surface Area of Mesoporous Titania by Using Template of F-68 and F-127 Co-Polymer in the Sol-Gel Process. *Journal of Nanoscience Nanotechnology*, 12, 7.
- Noor, E. A. & Al-Moubaraki, A. H (2008) Corrosion Behaviour of Mild Steel in Hydrochloric Acid Solutions. *International Journal of Electrochemical Science*, 3, 806 – 818.
- Nordin, N., Hamzah, Z., Hashim, O., Hafiz-Kasim, F. & Abdullah, R. (2015) Effects of Temperature in Calcination Process of Sea Shells. *Malaysian Journal of Analytical Sciences*, 19, 1, 65-70
- Nurudeen, A. R. & Oluleke, O. O. (2013). Optimization of the Annealing Parameters for Improved Tensile Properties in Cold Drawn 0.12 wt.% C Steel *SCIRP Engineering*, 5, 870-876
- Nurettin, E., Hamza, S. & Selhan, K. (2015) Preparation of Nano – Silver Supported Activated Carbon Using Different Ligands *Paper Presented at the 17<sup>th</sup> International Conference on Nanoscience and Nanotechnology, Paris, France 2015*

- Ocheri, C., Ajani, O. O. Daniel, A. & Agbo, N. (2017) The Steel Industry: A Stimulus to National Development. *J of Powder Metallu Min*, 6, 156
- Oki, M, J. (2007): Studies on chromium-free conversion coatings on aluminium, *Appl. Sci. Environ. Manage.* 11, 2, 187
- Olafadehan, O. A., Jinadu, O. W., Salami, L. & Popoola, O. T. (2012) Treatment of Brewery Wastewater Effluent Using Activated Carbon from Coconut Shell, *International Journal of Applied Science Technology*, 2(1), 165 – 78
- Olfa, H., Leila, D., Patrice, B., El Mustafa, R.. & Ezzeddine, T. (2012). Study of Zn-Ni Alloy Coatings Modified by Nano-SiO<sub>2</sub> Particles Incorporation. *International Journal of Corrosion*, 4(1), 98-100. doi:10.1155/2012/301392
- Olowoyo, D. N. & Orere, E. E. (2012) Preparation and Characterization of Activated Carbon Made from Palm- Kernal Shell, Coconut Shell, Groundnut Shell and Obeche Wood (Investigation of Apparent Density, Total Ash Content, Moisture Content, Particle Size Distribution Parameters) *International Journal of Research in Chemistry and Environment*. 2(3), 32 – 38.
- Onyeji, L. I. & Aboje, A. A (2011) Removal of Heavy Metal from Dye Effluent Using Activated Carbon Produced from Coconut Shell *Int J. Eng Sci Technol*, 3, 8238 - 46
- Ozdemir, M., Bolgaz. T., Saka, C. & Sahin, O. (2011) *Preparation and Characterization of Activated Carbon from Cotton Stalks in a Two-stage Process. Journal of Anal Appl Pyrolysis* 92, 171–175
- Pandia, P. R., Mohammad, I., Seyedmottaba, G., Jahangir, M., Mokhtar, C. I. Saeid, K. & Afidah, A. R. (2016). Reviews on Corrosion Inhibitors: A Short View *Chemical Engineering Communications*. 203(9),97-99  
doi.org/10.1080/00986445.2016.1172485
- Phindile, B. K., Makwena, J. M. & Lucky, N. (2012). The Effect of Solvent, Acetone, Water, and Ethanol on the Morphological and Optical Properties of ZnO Nanoparticles Prepared by Microwave. *Journal of Nanotechnology*, 19(1), 67-71.  
doi:1155/2012/195106
- Phani, A. R., Gammel, F. J., Hack, T., & H. Haefke (2005). *Mater. Corros.* 56, 2, 77
- Philip, G. H., Wan, A., Ahmed, T. M., Craig, B., Wayne, D. & Nicholas, C. L. (2007). Structure and Activity of Cu/ Cr/SnO<sub>2</sub> Environmental Control Catalysts. *Studies in Surface Science and Catalysis* 116, 495-505.
- Popoola, A., Olorunniwo. O. E. & Ige, O. O. (2014). Corrosion Resistance Through the

Application of Anti- Corrosion Coatings In book: Developments in Corrosion Protection. doi.org/10.5772/57420

- Popoola, A. I. P., Aigbodion, V. S. & Fayomi, O. S. I. (2016). Anti-Corrosion of Mild Steel Using Ternary, Zn- ZnO-Y<sub>2</sub>O<sub>3</sub> Electro-deposition *Journal of Surface & Coating Technology*.
- Popoola, A. P. I., Loto, C. A., Osifuye, C. O., Aigbodion, V. S. & Popoola, O. M. (2016). Corrosion and Wear Properties of Ni-Sn-P Ternary Deposits on Mild Steel Via Electroless Method. *Alexandria Engineering Journal*.
- Pramesh, N. K., Ajay, K. B., Ravichandra, S. M. & Kenneth, K. (2004). Mixed Metal Oxide Nanoparticles. *Dekker Encyclopedia of Nanosciences and Nanotechnology* (2007-2017) Marcel Dekker Inc. doi: 10.120/NOE0849396397.ch197.
- Pratibha, B. & Jayant, N. (2017). Characterization and Activation of Coconut Shell Activated Carbon Research Paper. *International Journal of Engineering Science Invention*. 6(11),43-49
- Punith, K. & Venkatesha, M. K. (2013). Fabrication of Zinc- nanoTiO<sub>2</sub> Composite Films: Electrochemical Corrosion Studies, *J. Chem. Pharm. Res.* 5(5), 253-261.
- Quadri, T. W., Olasunkanmi, L. O., Fayemi, O. E., Solomon, M. M. & Ebenso, E. E. (2017). Zinc Oxide Nanocomposites of Selected Polymers: Synthesis, Characterization, and Corrosion Inhibition Studies on Mild Steel in HCl Solution. *American Chemical Society Omega*, 8421-8427. doi.org/10.1021/acsomega.7b01385
- Ramanjeet, S., Simranjit, S. Gurlal, S. & Arshdeep, S. (2014). A Review of Porosity Formation and Recommendations on the Avoidance of Porosity in TTIG Welding of Steel *International Journal of Mechanical Engineering and Information Technology*, 2(8), 78-80.
- Ramezanzadeha, B., Attara, M. M. & Farzamb, M. (2011) A Study on the Anticorrosion Performance of the Epoxy-polyamide Nanocomposites Containing ZnO Nanoparticles *Pro. Org. Coating*, 72, 410 – 22
- Rani, B. E. A. & Basu, B. B. J. (2011). Green Inhibitors for Corrosion Protection of Metals and Alloys: An Overview. *International Journal of Corrosion*, Article ID 380217, 15 pages, 2012. doi.org/10.1155/2012/380217
- Rengarag S., Seung-Hyeon Moon, Sivabalan S., Arabindoo B. & Murugesan V., (2002). Agricultural Solid Waste for the Removal of Organics: Adsorption of Phenol from Water and Wastewater by Palm Seed Coat Activated Carbon. *Waste Management*, 22, 543-548 (2002).55

- Rengarag, S., Arabindoo, B. & Murugesan, V. (1996). Activated Carbon from Rubber Seed and Palm Seed Coat, Preparation and Characterization. *Journal of Science and Industrial Research*, 57, 129-132.
- Rishipal, R. B (2002). Treatment Of Organic And Inorganic Pollutants In Municipal Wastewater By Agricultural By-Product Based Granular Activated Carbons (GAC). A Thesis Submitted to the Graduate Faculty of the Louisiana State University and Agricultural and Mechanical College in partial fulfillment of the requirements for the degree of Master of Science in the Department of Food Science, Osmania University,
- Rodriguez- Reinoso, F., Molina-Sabio, M. & Gonzalez, M. (1995). The Use of Steam and CO as Activating Agents in the Preparation of Activated Carbons *Carbon* 33(1), 15-23
- Russo, F., Rossi, S. & Compagnoni, A. M. (2021). Porcelain Enamel Coatings. *Encyclopedia 2021*, 1, 388-400. doi.org/10.3390/encyclopedia1020032
- Rodriguez-Reinoso F., Molina-Sobia M. & Gonzalez G. C. (2001). Preparation of activated carbon– sepiolite pellets. *Carbon*, 39, 771 – 785
- Sahu, J. N., Acharya, J. & Meikap, B. C. (2010) Optimization of Production Conditions for Activated Carbons from Tamarind Wood by Zinc Chloride Using Response Surface Methodology. *Bioresour Technol*, 101, 1974 – 82
- Sajjadi, S. P. (2005) Sol-gel Process and its Application. *Journal of Polymer Engineering and Technology*, 13, 38-41
- Sanni, E. S., Emetere, M. E., Odigire, J. O., Efeovbokham, V. E., Agboola, O. & Sadiku, E. R. (2017) Determination of Optimum Conditions for the Production of Activated Carbon Derived from Separate Varieties of Coconut Shells. *International Journal of Chemical Engineering*. doi.org/10.1155/2017/2801359
- Sarmed, A. S., Abdalrasoul, S. M. & Ali, S. N. A. (2013). Study the Effects of Nickel Coating on Fatigue Life of Low Carbon Steel Exposed to Corrosive Environment, *Journal of Environmental and Earth Science*, 3, 5.
- Saravanan, P., Selvarajan, V., Josh, S. V. & Sundarajan, G. (2001). Experimental Design and Performance Analysis of Alumina Coatings Deposited by a Detonation Spray Process. *Journal of Physics*, 34(2001) 131-140. doi:10.1088/0022-3727/34/1/320
- Schaefer, K. & Miszczyk, A. (2013). Improvement of Electrochemical Action of Zincrich Paints by Addition of Nanoparticulate Zinc. *Corrosion Science*, 66, 380-391.

- Scully J R, Taylor D. W. (1987). Electrochemical Methods of Corrosion Testing, Metals Hand Book, 13,
- Serena, T. (2019). Traditional Sol-Gel Chemistry as a Powerful Tool for the Preparation of Supported Metal and Metal Oxide Catalyst. *Materials*, 12, 668
- Shailesh, K. D., Khanna, A. S. & Sinha, T. J. M. (2009). Effects of Nano-ZnO Particles on the Corrosion Behaviour of Alkyd-based Waterborne Coatings, *Progress in Organic Coatings* 64, 371 -382
- Sharmila, R., Selvakumar, N. & Jeyasubramaniam, K. (2012). Smart Coating for Corrosion Protection by Adopting Nano Particles *Progress Org Coatings*, 74, 461469
- Shamsuddin, M. S., Yusoff, N. R. N. & Sulaiman, M. A. (2016). Synthesis and Characterization of Activated Carbon Produced from Kenaf Core Fiber Using H<sub>3</sub>PO<sub>4</sub> Activation. *Procedia Chemistry* 19, 558-565
- Shanaghi, A., Sabour, R. A. A., Shahrabi, T. & Aliofkhazraei, M. (2009). Corrosion Protection of Mild Steel by Applying TiO<sub>2</sub> Nanoparticle Coating via Sol-Gel Method. *Protection of Metals and Physical Chemistry of Surfaces* 45(3):305-311 doi:10.1134/S2070205109030071
- Shao, Y., Jia, C., Meng, G., Zhang, T. & Wang, F. (2009). The Role of Zinc Phosphate Pigment in the Corrosion of Scratched Epoxy-Coated Steel. *Corrosion Science* 51(2),371-379 doi:10.1016/j.corsci,11.015
- Shawabkeh R., Rockstraw D. & Bhada R. (1998). Activated Carbon Feedstock. United States Patent 6225256
- Shei, L., Sun, C., Gao, P., Zhou, F. & Liu, W. (2005) Mechanical Properties and Wear and Corrosion Resistance of Electrodeposited Ni- Co/SiC Nanocomposite Coating. *Applied Surface Science* 252, 3591-3599
- Shen, L., Zhang, H. & Guo, S. (2009) Control on the Morphologies of Tetrapod ZnO Nanocrystals. *Mater Chem Phys*. 2009; 114:580–583
- Shi, X. M., Nguyen, T. A., Suo, Z. & Liu, Y. (2009) Effect of Nanoparticles on the Anticorrosion and Mechanical Properties of Epoxy Coating *Surf. Coat. Technol.* 204 (3) 237–45 2009
- Shi, Y., Yang, B. & Liaw, P. K. (2017) Corrosion –Resistant High-Entropy Alloys: A Review. *Metals* 2017, 7,43.
- Siavash, I. (2011). Green Synthesis of Metal Nanoparticles Using Plants. *Green Chem.* 2011 13:2638-2650: DOI:10.1039/C1GC15386b

- Song, Y. K. & F. Mansfeld (2006): Development of a Molybdate–Phosphate–Silane–Silicate (MPSS) Coating Process for Electrogalvanized Steel, *Corrosive Science*, 48, 154.
- Srivastava, M., Balaraju, J. N., Ravishankar, B & Rajam, K. S. (2010). Improvement in the Properties of Nickel by Nano Cr<sub>2</sub>O<sub>3</sub> Incorporation *Surface Coating Technology.*, 205, 66.
- Starkova, O., Buschhorn, S. T., Mannov, E. Schulte, K. & Aniskevich, A. (2013). Water Transport in Epoxy/MWCNT Composites. *European Polymer Journal*, 49, 2138–2148
- Stromeier, B.R., Bunker, K. L., Lopano, C. L. Marquis Jr, J. P., Piasecki, J. D., Bennethum, K. E., White, R. G., Nunney, T. & Lee, R. J. (2009). XPS and SEM/TEM Characterization of Silver Nanoparticles Formed from the X-ray-Induced and Thermal Reduction of Silver Behenate *Microsc Microanal* 15.
- Suba, K., Easwaramoorthi, D. & Andal, G. (2016). Corrosion Inhibition Using Nanomaterials -An Overview. *ResearchGate*, 3(110), 167-170.
- Sugumaran, P., Susa, V. P., Ravichandran, P. & Seshadri, S. (2012) Production and Characterization of Activated Carbon from Bana Empty Fruit Bunch and *Delonix Regia* Fruit Pod. *Journal of Sustain Energy Environment* 3,125 – 32
- Sumathi, S., Bhatia, S., Lee, K. T. & Mohamed, A. R. (2009). Optimization of Microporous Palm Shell Activated Carbon Production for Flue Gas Desulfurization: Experimental and Statistical Studies, *Bioresour Technol.* 100, 1614-1621
- Sumitra, K., Jilesh, P. & Samir, C. (2016). Preparation and Characterization of Activated Carbon from Agricultural Waste, Peanut Shell by Chemical Activation. *International Journal of Trend in Research and Development*, 3(3), 2394-9333
- Sun, L. H., Yang, Z. G. & Li, X. H. (2008). Mechanical and Tribological Properties of Polyoxymethylene Modified with Nanoparticles and Solid Lubricants *Polymer Eng. Sci.* 48, 1824–32
- Tadda, M. A., Ahsan, A., Shitu, A., El-Sergany, M., Arukumar, T., Jose, B., Razzaque, M. A., & Daud, N. N. N. (2016). A Review on Activated Carbon: Process, Application and Prospects, *Journal of Advanced Civil Engineering Practice and Research.*
- Thuan, T. V., Thinh, P. V., Quynh, B. T. P., Cong, H. T., Tam, D.T.T. Thouan, V.N & Bach L. G. (2016). Production of Activated Carbon from Sugercane Bagasse by Chemical Activation with ZnCl<sub>2</sub>: Preparation and Characterization Study *Research Journal of Chemical Science*, 6(5), 42-47.

- Tian, H., Li, W., Cao, K. & Hou, B. (2013). Potent Inhibition of Copper Corrosion in Neutral Chloride Media by Novel Non-toxic Thiadiazole Derivatives. *Corrosion Sciences*, 73, 281–291.
- Touzain, S. Thu, Q. L. & Bonnet, G. (2005). Evaluation of Thick Organic Coatings Degradation in Seawater Using Cathodic Protection and Thermally Accelerated Tests. *Progress in Organic Coatings*, 52, 311-319.
- Tsai, W. T., Chang, C. Y. & Lee, C. Y. (1998). A Low-Cost Adsorption from Agricultural Waste Corn Cob by Zinc Chloride Activation. *Bioresour Technol* 64,211-7
- Tsoncheva, T., Genova, I., Stoyeva, I., Spassove, I., Ivanova, R. Tsyntsarki, B. Kovachova, D. & Pehov, N. (2015). Activated Carbon from Waste Biomass as Catalyst Support: Formation of Active Phase in Copper and Cobalt Catalysts for Methanol Decomposition, *Journal of Porous Matter*. doi 10. 1007/s10934-0159988-7
- Ulrich, S & Husing, N. (2012). *Synthesis of Inorganic Materials 3<sup>rd</sup> Ed.* WILEY-VCH Verlag GmbH & Co. KGaA, Weinheim.
- Um, J. G. Jun, Y. S., Alhumade, H., Krithivasan, H., Lui, G. & Yu, A. (2018). Investigation of the Size Effect of Graphene Nano-Platelets (GnPs) on the AntiCorrosion Performance of Polyurethane/GnP Composites. *RSC Adv.* 8, 17091–17100
- Umoren, S. A. & Solomon, M. M. (2017). Synergistic Corrosion Inhibition Effect of Metal Cations and Mixtures of Organic Compounds: A Review. *Journal of Environmental Chemical Engineering*, 5, 246–273.
- Umoru, L. E. (2001):' Corrosion Studies in a Tar Sand Digester, Unpublished Ph D Thesis, Materials Science and Engineering Dept., O. A. U., Ile – Ife.
- Varila, T., Bergna, D., Lahti, R., Romar, H., Hu, T. & Lassi, U. (2017). Activated Carbon Production from Peat Using ZnCl<sub>2</sub>: Characterization and Application *Bio Resources* 12(4) 8078 -8092
- Veloz, M. A. & Gonzáaalez, I. (2002). Electrochemical Study of Carbon Steel Corrosion in Buffered Acetic Acid Solutions with Chlorides and H<sub>2</sub>S. *Electrochimica Acta*, 48,135–144.
- Verma, C., Olasunkanmi, L. O., Akpan, E. D., Quraishi., M. A., Dagdag, O., El Gouri, M., El-Sayed, M. S. & Ebenso, E. E. (2020). Epoxy Resins as Anticorrosive Polymeric Materials: A Review. *Reactive and Functional Polymers*. 156,104741 doi.org/10.1016/j.reactfunctpolym.104741

- Verradate, P., Voranuch, T., Piyapong, A. & Pichet, L. (2012) Preparation and Characterization of Aluminium Nanoparticles in Deionized Water Using Laser Ablation Technique. *Journal of Nanoparticles*. 819403,
- Vijaya, P. D., VaideiBalraj, K. & Satish, D. K. (2018) Synthesis and Characterization of Aluminium Oxide (Al<sub>2</sub>O<sub>3</sub>) Nanoparticles and its Application in Azodye Decolourization. *International Journal of Environmental Chemistry*. 2(1),10-17
- Vineetha, M., Shiyao, S., Chuan-Jian, Z. and Oana, MM. (2018). Effects of Chemical Composition on the Nanoscale Ordering Transformations of Physical Mixtures of Pd and Cu Nanoparticles. *Journal of Nanomaterials*. Article ID 9087320, 10
- Viswanathan, B., Indra- Neel, P. & Varadarajan, T. K. (2009). Methods of Activation and Special Application of Carbon Materials. National Centre for Catalytic Research Department of Chemistry, Institute of Technology Madras Chennai, India 600.036 2009.
- Vladimir, V., Nikolay, K., Anton, K., Ilya, Z & Alexandr, V. (2018). Investigation of the Structure, Mechanical Properties and Crystallization of Aluminum Alloys Containing Oxides Nanoparticles. MATEC Web of Conferences 243, 00022.
- Wan-Nik, W. B., Rahman, M. M., Yusof, A. M., Ani, F. N. & Adnan, C. M. C. (2006). Production of Activated Carbon from Palm Oil Shell Waste and its Adsorption Characteristics *In: Proceedings of the 1<sup>st</sup> International Conference on Natural Research and Engineering Technology*.
- Wang, J., Xu, R. & Zhang, Y. (2010). Influence of SiO<sub>2</sub> Nanoparticles on Microstructures and Properties of Ni-W-P/CeO<sub>2</sub>-SiO<sub>2</sub> Composites Prepared by Pulse Electrodeposition, *Science Direct, Transactions of Nonferrous Matetrials of China* 20, 839 – 843
- Wang, M. & Zhoa, Q. (2019). Biomedical Composites. *Encyclopedia of Biomedical Engineering*, 34-52. doi.org/10.1016/B978-0-12-801238-3.99868-4
- Wang, T. X. & Lou T. J. (2008). Solvothermal Synthesis and Photoluminescence Properties of ZnO Nanorods and Nanorod Assemblies from ZnO<sub>2</sub> Nanoparticles. *Mater Lett*. 62,2329–2331
- Wang, J., Zhao Q., Hou, H., Wu, Y., Yu, W., Ji, X. & Shao, L. (2017). Nickel Nanoparticles Supported on Nitrogen-Doped Honeycomb-like Carbon Frameworks for Effective Methanol Oxidation *RSC Adv*. 7, 14152-14158
- Wen, N. T., Lin, C. S., Bai, C.Y. & Ger, M. D. (2008). Structures and Characteristics of Cr(III)-Based Conversion Coatings on Electroalvanized Steels, *Surf. Coat. Technol*. 203, 317

- Williams, P. T & Reed, A. R. (2004). High Grade Activated Carbon Matting Derived from the Chemical Activation and Pyrolysis of Natural Fibre Textile Waste. *J Anal Appl Pyrol*71:971-86
- Wu, F. C. & Tseng, R. L. (2006) Preparation of Highly Porous Carbon from Fire Wood by KOH Etching and CO<sub>2</sub> Gasification for Adsorption of DYES and Phenols from Water. *J. Colloid Interface Sci* 294-, 21-30
- Xavier, J. R. (2020). Investigation on the Anticorrosion, Adhesion and Mechanical Performance of Epoxy Nanocomposite Coatings Containing Epoxy-Silane Treated Nano-MoO<sub>3</sub> on Mild Steel. *J. Adhes. Sci. Technol.* 34, 115–134
- Yacob, A. R., Majid, Z. A., Dasri, R. S. D. & Inderan, V. (2008) Comparison of Various Sources of High Surface Area Carbon Prepared by Different Types of Activation. *Malays J Anal Sci.* 12(1),264-71
- Yahya, M. A., Al-Qodahb, Z. & Zanariah Ngaha, C. W. (2015) Agricultural bio-waste materials as potential sustainable precursors used for activated carbon production: A Review Renewable and Sustainable *Energy Reviews* 46, 218-235 doi.org/10.1016/j.rser.02.051
- Yahaya, N. K. E. M., Latiff, M. F. P. M., Abustan, I., Bello, O. S. & Ahmad, M. A. (2010). Effects of Preparatory Conditions of Activated Carbon from Rice Husk by ZnCl<sub>2</sub> Activation for Removal of Cu(II) from Aqueous Solution. *Int J. Eng Technol.*(6):27-31
- Yathish, U. & Chitharanjan, A. H. (2013) Corrosion Protection of Electrodeposited Multilayer Nanocomposite Zn-Ni-SiO<sub>2</sub> Coatings
- Yorgun, S. & Yildiz, D. (2015). Preparation and Characterization of Activated Carbon from Paulownia Wood by Chemical Activation with H<sub>3</sub>PO<sub>4</sub>. *Journal of the Taiwan Institute of Chemical Engineers* 53, 122 - 131
- Yusufu, M. I., Ariaahu, C. C. and Igbabul B. D. (2012). Production and Characterization of Activated Carbon form Selected Local Raw Materials, *AFR J Pure Appl Chem.* 6(9):123 – 31.
- Zainudin, N. F., Lee, K. T., Kamaruddin, A. H., Bhatia, S. & Mohamed, A. R. (2005). Study of Adsorbent Prepared from Oil Palm Ash (OPA) for Flue Desulfurization. *Separation and Purification Technology*, 45(1), 50-60. doi: org/10.1016/j.seppur.2005.02.008
- Zazo, J. A., Fraile, A. F., Rey, A., Bahamonde, A., Casa, J.J. & Rodrguez, J. J. (2009).

- Optimizing Calcination Temperature of Fe/Activated Carbon Catalyst for CWPO. *Catalysis Today*, 143(3-43)41-346
- Zhang, J. Fu H, Lv X., Tang J. and Xu X (2011). Removal of Cu(II) from Aqueous Solution Using the Rice Husk Carbons Prepared by the Physical Activation Process. *Biomass Bioenergy* 35, 464–472
- Zhou, Y. X. (2008). Improvement in Electrical Thermal, and Mechanical Properties of Epoxy by Filling Carbon Nanotubes. *Express Polymer Letters*, 2(1), 40-48
- Zhu, Z., Li, A., Xia, M., Wang, J. & Zhang, Q. (2008.) Preparation and Characterization of Polymer Based Spherical Activated Carbons. *Chin J Polym Sci*, 26(5), 645-51
- Zubillaga, O., Cano, F. J., Azkarate, I., Molchan, I. S., Thompson, G. E. & Skeldon, P. (2009). Anodic Films Containing Polyaniline and Nanoparticles for Corrosion Protection of AA2024T3 Aluminum Alloy. *Surf. Coat. Technol.* 203, 1494-1501, doi.org/10.1016/j.surfcoat.2008.11.023